Modeling and Control of an Active Dihedral Fixed-Wing Unmanned Aircraft

Ryan D. Fisher

Dissertation submitted to the Faculty of the
Virginia Polytechnic Institute and State University
in partial fulfillment of the requirements for the degree of

Master of Science
in
Aerospace Engineering

Craig A. Woolsey, Chair
Pradeep Raj
Wm. Michael Butler

May 9, 2022
Blacksburg, Virginia

Keywords: Active Dihedral, Gust Rejection, Unmanned Aircraft System, Linear Parameter-Varying, Gain Scheduling

Copyright 2022, Ryan D. Fisher

Modeling and Control of an Active Dihedral Fixed-Wing Unmanned Aircraft

Ryan D. Fisher

(ABSTRACT)

Unmanned aircraft systems (UAS) often encounter turbulent fields that perturb the aircraft from its desired target trajectory, or in a manner that increases the load factor. The aircraft's fixed dihedral angle, providing passive roll-stiffness, is often selected based on lateral-directional stability requirements for the vehicle. A study to predict the effect of an active dihedral system on lateral-directional stability and vertical gust rejection capability was conducted to assess the performance and feasibility of the system. Traditionally, the dihedral location begins at the root to maintain wing structural requirements, however, the active dihedral system was also evaluated for dynamic stability and gust rejection performance at alternative dihedral breakpoint locations. Simulations were completed using linear parameter-varying (LPV) models, derived from traditional Newtonian aircraft dynamics and associated kinematic equations, to improve the modeling of the nonlinear active dihedral system. The stability of the LPV system was evaluated using Lyapunov stability theory applied to switched linear systems, assessing bounds of operation for the dihedral angle and flapping rate. An ideal feedback controller was developed using a linear–quadratic regulator (LQR) for both a discrete gust model and a continuous gust model, and a gain scheduled LQR controller was implemented to show the benefits of gain scheduling with a parameter varying state and input model. Finally, a cost analysis was conducted to investigate the real-world benefit of altering the dihedral breakpoint location. The effects of the active dihedral system on battery capacity and consumption efficiency were observed and compared with the gust rejection authority.

Modeling and Control of an Active Dihedral Fixed-Wing Unmanned Aircraft

Ryan D. Fisher

(GENERAL AUDIENCE ABSTRACT)

Unmanned aircraft systems (UAS) often encounter wind disturbances that perturb the aircraft from its desired target trajectory, or in a manner that increases the force encountered on the vehicle. The aircraft's fixed dihedral angle, providing stiffness to roll rotations, is often selected based on stability and control requirements for the vehicle. A study to predict the effect of a flapping wing (active dihedral) system on the stability, control, and wind gust rejection capability is completed to assess the performance and feasibility of such a system. Traditionally, the dihedral location begins at the root to maintain wing structural requirements, however, the active dihedral system was also evaluated for stability and wind gust rejection performance at alternative locations along the wing where the dihedral could begin, with intention of finding the best location. Simulations were completed using a varying set of simplified models, obtained from traditional aircraft mechanics, to improve the modeling of the true complex active dihedral system. The stability of the system was evaluated using various theories applied to the linear systems in attempt to define a bounded operating region for the dihedral angle and flapping motion. An ideal controller for the system was developed using ideas from well documented linear control theory for both a single wind gust and a continuous wind gust model. A controller that varies with vehicle flapping motion was implemented to show the benefits of scheduling the controller with a parameter varying state and input model. Finally, a cost analysis was conducted to investigate the real-world benefit of altering the dihedral starting location. The effects of the active dihedral system on battery capacity and consumption efficiency were observed and compared with the total gust rejection capability.

Dedication

This thesis is dedicated to my family, friends, colleagues, professors, and those who never gave up.

Acknowledgments

I would first like to acknowledge Dr. Craig Woolsey. During undergraduate school, Dr. Woolsey consistently took the time to invest in me as a student, and provide me with the resources I needed to succeed. After completing this thesis, I've seen the work he puts in to be a professor, and it's admirable how much he supports his students and helps them succeed, despite the responsibilities he has. Thank you Dr. Woolsey for taking the time to invest in me, help me become the engineer I am today, and set an example in academia for how a professor should interact and support their students. Thank you for allowing me to work on this project throughout undergraduate school and continue the theoretical development as a thesis; it has been an invaluable experience.

I would also like to acknowledge my family, friends, mentors, and Virginia Tech faculty for continually supporting me in pursuit of my education and life aspirations. I thank my family for helping provide this opportunity to me, knowing that not everyone gets a shot like this. I need to thank those friends in undergraduate school who made getting an education even more of an adventure than it has been; between the late study nights and aircraft building competitions, it was moments like those that made obtaining an education in aerospace engineering unforgettable. To those friends who inspired me to continue putting forward my best work, even when this meant no sleep, thank you. To the mentors who encouraged and motivated me to work while obtaining my graduate degree, thank you; it was an invaluable lesson in time management, task prioritization, and financially a great decision. I would like to thank all the Virginia Tech faculty for their hard work and time investing in students' growth, as I would not be the person I am today without their investment.

Contents

List of Figures

List of Tables

List of Abbreviations

α	Angle of Attack
$\bar{c}$	Mean Aerodynamic Chord
$\bar{y}$	Spanwise Center of Lift
β	Sideslip Angle
δ_τ	Torque Input
δ_a	Aileron Deflection
δ_r	Rudder Deflection
δ_T	Throttle Input
Γ	Dihedral Angle
ω_n	Natural Frequency
ϕ	Euler Roll Angle
ψ	Euler Yaw Angle
ρ	Atmospheric Density
σ	The total mass of angels per unit area
τ	Time Constant
θ	Euler Pitch Angle

$\vec{V_n}$ Wing Normal Velocity Vector

$\vec{V}$ Velocity Vector

ζ Damping Ratio

A State Matrix

AR Aspect Ratio

b Wing Span

B_u Controller Input Matrix

B_w Disturbance Input Matrix

C Output Matrix

$c(y)$ Spanwise Chord

C_D Drag Coefficient

C_d Cross-section Drag Coefficient

C_L Lift Coefficient

C_l Body-Axis Rolling Moment Coefficient

C_m Body-Axis Pitch Moment Coefficient

C_n Body-Axis Yaw Moment Coefficient

C_{l} Cross-section Lift Coefficient

D Dimensional Drag Force

D Feed-through Matrix

e	Oswald Efficiency
F_g	Flight Profile Alleviation Factor
H	Gust Gradient Length
I_W	Body-Axis Wing Roll Moment of Inertia
I_x	Body-Axis Roll Moment of Inertia
I_y	Body-Axis Pitch Moment of Inertia
I_z	Body-Axis Yaw Moment of Inertia
J	Cost Function
K	Gain Matrix
L	Dimensional Lift Force
L_{roll}	Dimensional Body-Axis Roll Moment
M	Dimensional Body-Axis Pitch Moment
N	Dimensional Body-Axis Yaw Moment
p	Body-Axis Roll Rate
q	Body-Axis Pitch Rate
q_∞	Dynamic Pressure
r	Body-Axis Yaw Rate
t	Time
$t_{\frac{1}{2}}$	Time to Half Amplitude

t_w	Wing Thickness
u	x Body-Axis Velocity Component
U_{ds}	Design Gust Velocity
U_{ref}	Reference Gust Velocity
v	y Body-Axis Velocity Component
$V(x)$	Lyapunov Function
w	z Body-Axis Velocity Component
X	Dimensional x Body-Axis Force
x^B	x Body-Axis
x^E	North Earth-Fixed Axis
x^S	x Stability-Axis
x_e	North Earth Fixed Position
$x_{c.g.}$	Distance to Center of Gravity along Body-Axis
Y	Dimensional y Body-Axis Force
y^B	y Body-Axis
y^E	East Earth-Fixed Axis
y^S	y Stability-Axis
y_e	East Earth Fixed Position
y_{b_Γ}	Dihedral Breakpoint

$y_{c.g.}$ Distance to Center of Gravity along Body-Axis

Z Dimensional z Body-Axis Force

z^B z Body-Axis

z^E Down Earth-Fixed Axis

z^S z Stability-Axis

z_e Down Earth Fixed Position

$z_{c.g.}$ Distance to Center of Gravity along Body-Axis

ARE Algebraic Riccati Equation

CFD Computational Fluid Dynamics

CFR Code of Federal Regulations

FAA Federal Aviation Administration

GUES Globally Uniform Exponentially Stable

LMI Linear Matrix Inequality

LPV Linear Parameter-Varying

LQG Linear Quadratic Gaussian

LQR Linear Quadratic Regulator

LTI Linear Time-Invariant

LTV Linear Time-Varying

MAV Micro-air Vehicle

MTD My Twin Dream

NSL Nonlinear Systems Laboratory

RMS Root Mean Square

UAS Unmanned Aircraft System

VLM Vortex Lattice Method

Chapter 1

Introduction

Throughout the history of aviation, many aircraft and their shapes have been inspired by nature due to many creatures' ability to fly seamlessly through the air. One phenomenon exhibited by birds that is continually being studied is the bird's flapping wing motion concerning gust rejection and stability. There have been many papers written in an attempt to better mimic nature, transitioning the capabilities of birds to human-made unmanned aircraft systems (UAS). This is most clearly seen in micro-air vehicles (MAV) which are inspired by smaller insects' ability to fly quickly with stability.

For general aircraft, there are three axes defined relative to the body: the roll, pitch, and yaw axis. Of these, only the pitch and yaw axis have a stiffness tendency that resists rotation perturbations. For the yaw axis, the vertical stabilizer provides a restoring yaw moment when the aircraft experiences a sideslip. The pitch axis experiences a similar restoring pitching moment through the horizontal stabilizer, as a trimmed elevator will bring the aircraft back to the set angle of attack after a perturbation. Regarding the roll axis, there is no aircraft component that induces a natural roll stiffness, except the ailerons having the capability of artificial roll stiffness, returning the aircraft to wings level with proper input from a feedback controller. To obtain a naturally passive roll stiffness, an increase in wing angle about the roll axis must be built into the aircraft; this angle is defined as the dihedral angle. The effect of passive roll stiffness created from this angle is defined as the dihedral effect. Dihedral is often incorporated into general aviation aircraft to provide longitudinal

stability while anhedral (negative dihedral angle) is given to military fighter jets for increased maneuverability. The effects of dihedral are not only prevalent in the aviation industry, but also in nature as seen in birds. Frequently during gusty wind conditions, birds such as the turkey vulture, shown in Figures 2.1a and 2.1b, will increase their dihedral angle relative to their body to increase their lateral-directional stability during gusty conditions, and decrease total lift when a headwind is encountered to maintain altitude. Birds along with aircraft sometimes employ a gull-wing configuration, obtaining some dihedral effect, but in general, less lift loss due to the dihedral angle starting at some point outward from the root. There is intrinsic benefit in this type of configuration and therefore it is considered for the development of an active dihedral system.

Due to the implicit effect of increasing passive roll stiffness and decreasing lift generated when increasing the dihedral angle, and conversely decreased roll stiffness and increased lift through a decreased dihedral angle, the question being asked is, do there exist benefits and use cases for UAS having an actuating system allowing for variable dihedral. There are many scenarios where UAS are required to maintain a given trajectory, pitch angle, or roll angle, to complete a specified mission. Assuming active dihedral would provide this gust rejection capability, the direct mission use cases would include, imaging on a windy day and landing on aircraft carriers with turbulent wakes. Both cases require fine-tuned aircraft performance to reduce the risk of aircraft damage and mitigate the loss of mission time. The question persists, can active dihedral be used to better accomplish a given mission where flight path accuracy is held as one of the highest measures of performance? The goal of this study was to attempt to answer this question by modeling and simulating an active dihedral system.

It can be challenging to accurately model and simulate a system whose state and dynamic properties are evolving with time and are dependent on external disturbances.

Modeling methods such as linear parameter-varying (LPV) systems can be used to better predict the response of a nonlinear system to disturbances and configuration changes, helping overcome deficiencies that exist with standard LTI systems, while preserving a system structure that is amenable to linear control design methods. Additionally, a well-tuned controller can be challenging to develop for these evolving systems, leading to a requirement for a dynamic set of feedback gains, commonly referred to as gain scheduling. These dynamic modeling and control techniques combined can lead to higher fidelity modeling and simulation of an active dihedral system.

This thesis describes the following observations and contributions. An active dihedral system can be a useful means of rejecting wind gusts and maintaining a targeted trajectory. The active dihedral system can be modeled to incorporate the changes in lift due to dihedral variation, the dihedral effect, and the flapping motion. These effects can be modeled successfully through the implementation of LPV systems such that the dynamic system can be represented as a function of dihedral angle and flapping rate. The stability of the LPV system can be evaluated with the Lyapunov stability criterion applied to switched systems. Through the evaluation of Lyapunov stability, a restricted domain of operating points can be identified for various configurations of dihedral and breakpoint. The application of gain scheduling to the active dihedral system using observable states can improve gust rejection performance. Finally, the system's gust rejection performance and physical cost associated with implementing an active dihedral system can be measured and evaluated. The associated cost of the active dihedral system can be assessed and varies with change in the dihedral breakpoint, as does the gust rejection authority. A thorough investigation of an active dihedral system applied to fixed-wing UAS is completed in this study, proving active dihedral to be a successful concept for UAS gust rejection.

Chapter 2

Background

2.1 Dihedral Angle in Nature

Often when encountering turbulence it is desired to have gust alleviation capability to increase passenger comfort or reduce the load factor experienced by the aircraft structure or the onboard payload and cargo. Gust alleviation is commonly associated with reducing the effect of wind gusts on a system, but in a more restrictive sense, it is specifically implying a reduction of a gust on load factor [1]. Birds commonly employ this gust alleviation by setting a specific dihedral angle for various wind conditions, also improving roll stability. Figure 2.1a shows a turkey vulture maintaining altitude and roll stability using a lower dihedral angle, with the ability to employ a higher dihedral angle as in Figure 2.1b. While birds do not explicitly have means of propulsion, external of flapping, the force balance often determines the correct dihedral setpoint to maintain altitude. If a large headwind were to be encountered by the bird, a large dihedral angle might be employed to dump lift, and conversely, with a small headwind, the dihedral angle might be lowered. If one were to ignore variation in altitude and the headwind speed, what determines the dihedral setpoint a bird selects for passive roll stability? While one can visualize a bird encountering a large lateral gust, we know that birds are likely capable of handling perturbations such that they do not roll off their lift vector unintentionally, leading to a rapid descent; one can picture a UAS being banked, encountering a larger lateral gust, rolling off the lift vector. Birds

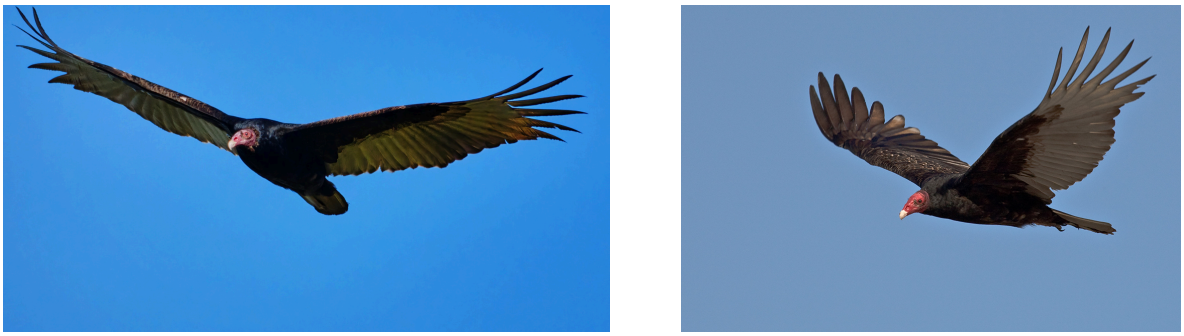

(a) Low dihedral angle employed (b) Large dihedral angle employed

Figure 2.1: Turkey vulture exhibiting different dihedral angle setpoints

are able to successfully employ an increase in passive roll stability through this increase of dihedral angle. It has been shown that birds also decrease their dihedral angle, such that anhedral is obtained, and roll into a bank similar to jets executing a high-performance maneuver; this is frequently executed via asymmetric dihedral [2]. This study looks to show how various aircraft configurations with active dihedral employed can result in a tunable lateral-directional stability system paired with vertical gust rejection capability.

Having the ability to tune the dihedral angle given a set of flight conditions is useful for increased lateral gust rejection in turbulent environments. Take for example the turkey vultures in Figure 2.1, at increased angles of attack, the effectiveness of the dihedral angle in rejecting a lateral wind gust becomes more pronounced. This type of tunable stability is beneficial for a mission requiring an aircraft to loiter, giving a reduction in roll-perturbation over a given target. Consider the same aircraft needing to return to a way-point after its loitering mission is complete. It is desirable to decrease the dihedral angle while at lower angles of attack, such as in cruise flight, to increase $\frac{L}{D}$ efficiency. At lower angles of attack, the dihedral angle provides reduced roll stiffness and yaw control, and hence the lateral gust could roll an aircraft off its trajectory if the increased dihedral angle is maintained [3]. This example highlights one reason why active dihedral is a useful concept for UAS.

It is also known that for aircraft with a flapping wing system, there exists the implicit ability to increase or decrease lift through the flapping effect assuming a pronounced rate of flapping. The direct lift generated through this operation can assist in the rejection of vertical gust disturbances, leading to improved flight path accuracy, and gust alleviation. Additionally, having the ability to actively increase the dihedral angle to a fixed position has been shown useful in specific UAS flight conditions, as Sachs and Holzapfel have shown the effects birds encounter when operating at large dihedral angles, including an intentionally smaller lift to drag ratio, increased plunge rate, and increased glide angle [4]. These effects can be obtained using an active dihedral system, allowing vehicles to ascend or descend in a faster yet controlled manner through a variation in glide slope. The capability associated with the vertical lift phenomenon obtainable through an active dihedral system is advantageous for UAS.

2.2 The Dihedral Effect

The dihedral effect is commonly referred to as the contribution of the wings to the stability derivative C_{l_β}, and is of significant importance to an aircraft's lateral and directional stability characteristics. The stability derivative, C_{l_β}, contributes directly to roll stiffness and the handling qualities of the aircraft, keeping the aircraft from "falling off its lift vector" during a sideslip maneuver [5]. The primary contributing aircraft components to the dihedral effect include the wing dihedral angle, wing sweep, vertical tail, and wing-fuselage interaction [1]. Note that of these features impacting roll stability, the wing dihedral angle and the vertical tail are the pronounced C_{l_β} contributors in this study.

Aircraft commonly have a fixed dihedral angle established at the wing-fuselage juncture, with the only variation in dihedral being due to structural deflection with increased

wing loading during flight. A fixed dihedral angle is selected based on aircraft design requirements including lateral-directional handling qualities, lift and drag predictions, and engine ground clearance requirements. The dihedral effect is used to improve lateral-directional handling characteristics, exhibited through a restoring rolling moment, upon aircraft encountering a sideslip, as depicted in Figure 2.2. The contribution of the wing dihedral angle to roll perturbation due to sideslip is estimated as follows for small dihedral angles. Assume

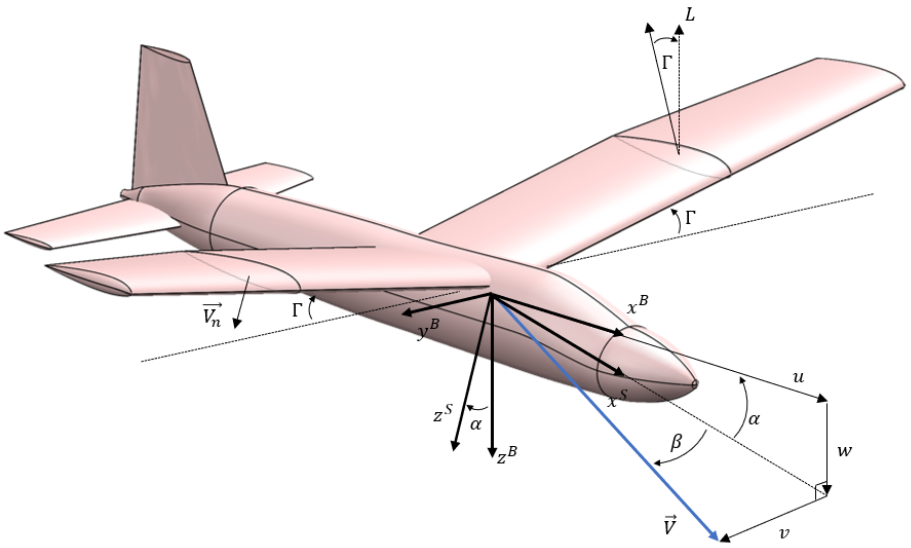

Figure 2.2: Aircraft with increased dihedral angle performing a sideslip

the aircraft enters a sideslip at an angle β, shown in Figure 2.2, experiencing a differential in normal velocity on the right wing, V_{n_R}, compared to the left wing, V_{n_L}. This normal velocity for the right wing is given as [6]:

$$V_{n_R} = w\cos(\Gamma) + v\sin(\Gamma) \approx w + v\Gamma \tag{2.1}$$

Conversely for the left wing:

$$V_{n_L} = w\cos(\Gamma) - v\sin(\Gamma) \approx w - v\Gamma \tag{2.2}$$

This normal velocity leads directly to a change in angle of attack for each wing, given for the right wing as [6]:

$$\Delta\alpha_R = \frac{v\Gamma}{V} = \frac{V\beta\Gamma}{V} \approx \beta\Gamma \tag{2.3}$$

The change in angle of attack for the left wing is:

$$\Delta\alpha_L = \frac{-v\Gamma}{V} = \frac{-V\beta\Gamma}{V} \approx -\beta\Gamma \tag{2.4}$$

This differential in the angle of attack leads to increased lift on the right wing and decreased lift on the left wing, inducing the negative restoring rolling moment. The stability derivative, C_{l_β}, leads to the restoring rolling moment when the aircraft encounters this sideslip. It is expected that with an increase in C_{l_β}, there exists additional stabilization in the spiral mode and destabilization in the Dutch roll motion. This summarizes the dihedral effect commonly referenced in literature and its implications on lateral-directional stability.

2.3 Effect of Dihedral on Roll Stiffness

To understand the contribution of dihedral angle to roll stiffness, denoted as C_{l_ϕ}, first roll stiffness and its effect on an aircraft must be understood. Consider an aircraft that is constrained to rotation about its longitudinal axis, x^B, allowing only one degree of freedom corresponding to the roll angle, ϕ; this can be seen as in Figures 2.3 and 2.4, derived from Etkin [1].

Assume also that the velocity vector of the vehicle is fixed along the x^B axis, which is parallel to the root chord of the wings. In this case, a change in ϕ does not alter the aerodynamic field, as the aerodynamic forces remain constant in the body-fixed frame, meaning the $C_{l_\phi} = 0$ equals zero. However, if the velocity vector, $\vec{V}$, is not aligned with the longitudinal

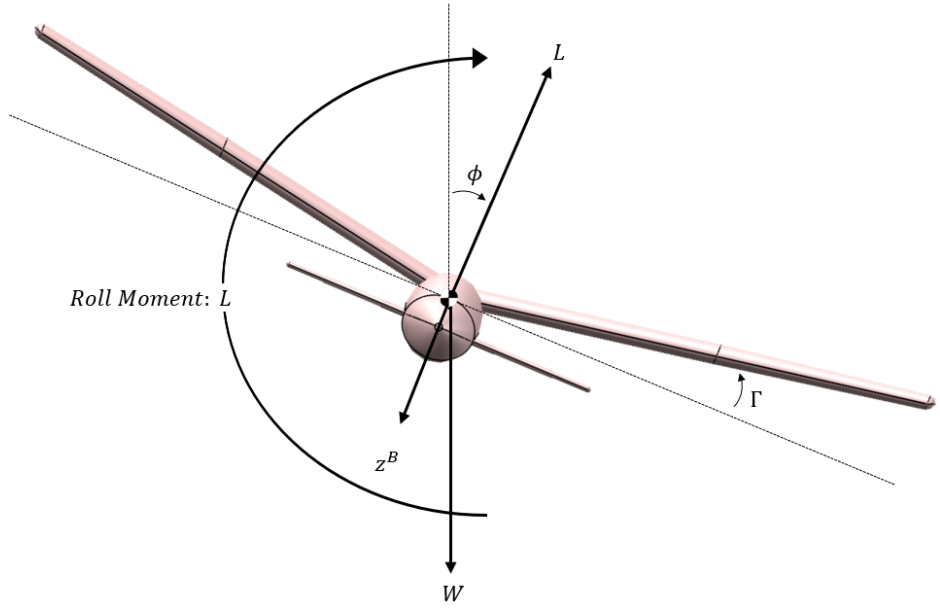

Figure 2.3: Rear view of rolled aircraft constrained about the longitudinal body axis

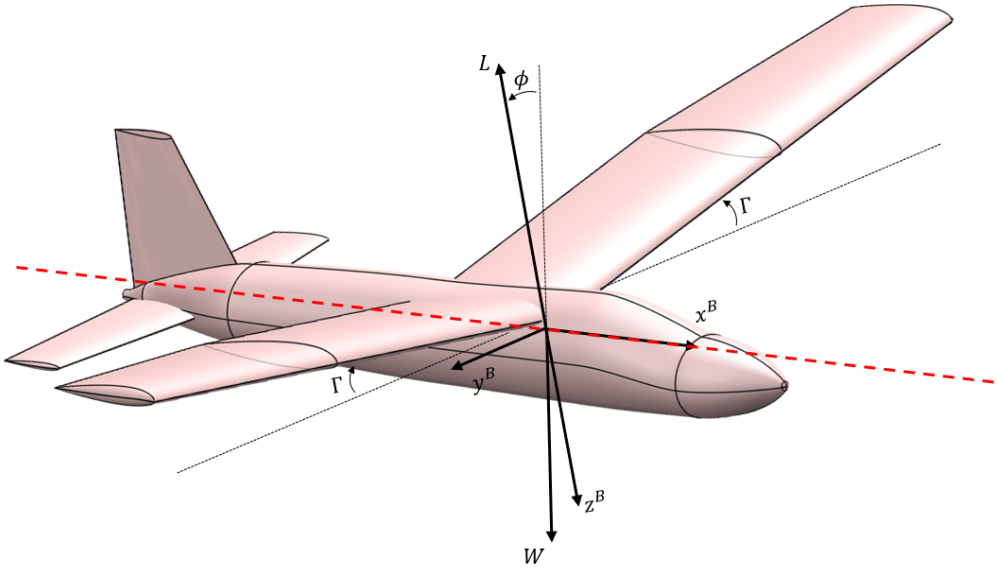

Figure 2.4: Isometric view of an aircraft with one degree of freedom, rotation angle ϕ, being pinned about the longitudinal body axis, x^B, denoted by the red dashed line

axis, then the dihedral effect, C_{l_β}, will contribute directly to the roll stiffness. Consider the aircraft to be at an angle of attack, α, defined as the angle between x^B axis and the stability axis, x^S, while rolling at an angle ϕ. The velocity vector in the body reference frame is then

described as [1]:

$$\vec{V_b} = \begin{bmatrix} V\cos\alpha \\ V\sin\alpha\sin\phi \\ V\sin\alpha\cos\phi \end{bmatrix} \tag{2.5}$$

The angle between the velocity vector and the x^S axis, relating to the lateral velocity component, v, is given to be the sideslip angle β.

$$\beta = \sin^{-1}(\frac{v}{V}) = \sin^{-1}(\sin\alpha\sin\phi) \tag{2.6}$$

Through additional derivation and small angle approximations, an estimate for the roll stiffness, C_{l_ϕ}, is given [1]:

$$\frac{\partial C_l}{\partial \phi} = C_{l_\beta}\alpha \tag{2.7}$$

Equation (2.7) applies only to a vehicle constrained about the longitudinal axis, but emphasizes the importance of the dihedral effect on the roll stiffness of an aircraft, with a negative C_{l_β} providing a restoring rolling moment for positive angles of attack. Conversely, at negative angles of attack, the roll stiffness becomes negative leading to aileron reversal [7].

2.4 Symmetric vs. Asymmetric Dihedral Angle

In the process of implementing an active dihedral system, consideration is given to asymmetric dihedral, where one wing of the aircraft has a larger dihedral angle than the other. In terms of steady state flight with no active dihedral, the outcome of this configuration is simply an aircraft whose fuselage roll attitude is non-zero (i.e. the fuselage is not level). In the case where the asymmetric dihedral is actively imposed, common in birds, the wing

with a larger dihedral angle produces a side force and a corresponding yawing moment, leading the aircraft into a sideslip, both of which can be used for lateral-directional control, as demonstrated by Paranjape et al. [8]. Similarly, this phenomenon can be induced through the use of twist in flexible wings. Flexible wings can deform naturally to produce a dihedral effect, but also the dihedral angle is enhanced with increased wing twist, and conversely reduced with a decrease in twist. These instances of perturbations in lateral forces due to asymmetric dihedral are leveraged and applied mainly by birds and aircraft lacking a vertical stabilizer [3]. The concept of asymmetric dihedral was ignored in this study, enforcing the requirement of symmetric dihedral through the coupling of left and right wing dihedral actuation. It is acknowledged that asymmetric dihedral may prove useful for lateral wind gust rejection, however, this study was focused on vertical gust rejection using active dihedral for direct control of lift. Removing the assumption of symmetric dihedral paired with the results of this study could lead to a vehicle capable of rejecting vertical and lateral wind gusts in multiple phases of flight.

2.5 Gust Alleviation Through Flapping Wings

This study looks to investigate the gust rejection capability, through wing actuation, available to small UAS flying at low Reynolds numbers. A distinction must be made between the terminology *gust rejection* and *gust alleviation*, as these assertions have different meanings. Gust rejection references the aircraft's ability to reject a wind gust in terms of position and attitude. Gust alleviation addresses the ability to reduce the forces and proportional acceleration experienced by aircraft. A bi-product of gust rejection may be gust alleviation, and visa versa, however, this is not guaranteed. A significant number of studies have been conducted to better understand the gust alleviation available to an aircraft

through actuation of the wings, typically through the use of mass and spring dampers [9]. Work by Castrichini et al. [9] showed that reductions in dynamic loads experienced by a commercial transport aircraft are possible with a wingtip positioned nominally at a 25° hinge angle. This result was obtained using a numerical aeroelastic model of the aircraft, tested against 1-cosine gusts disturbances, with a well-tuned torsional damping system in place for the hinged surface. This study noted that incorrect torsional damping resulted in exacerbated loading on the vehicle. A related experimental study was conducted by Cheung et al. [10] using a pulley mechanism to actuate the wingtip, dampening the response of the wing to the loading. A maximum 56% reduction in the rolling moment was obtained through this configuration, leading to experimental validation of the claim that wingtips can be used for gust alleviation. The concepts presented here invoke the flapping wing concept at the wing tip for gust alleviation, through the use of a hinged wing with springs and dampers employed. There is little published literature regarding the use of a motor or other similar means to actuate a rigid wing to employ a gust rejection control law. This study attempts to fill the void in this literature.

2.6 Dihedral Breakpoint

Dihedral breakpoint, defined as the spanwise position in which the dihedral angle begins, is of interest to an active dihedral system. The typical aircraft configuration imposes a fixed dihedral angle starting at the wing root, remaining fixed for the entire span. Design criteria, including structural requirements, aerodynamic performance, and wing clearance, often drive this decision.

While a dihedral breakpoint greater than zero is not typical for traditional aircraft, it is common to see birds implement this type of wing, providing similar stability characteristics

but with improved aerodynamic performance as previously seen in Figure 2.1. Mimicking this bird-like actuation, experimental investigations have been completed by Mills and Ajaj [7], showing the benefits of having an increased dihedral angle at the dihedral breakpoint significantly outboard from the root. The study showed that through the use of folding wingtips, an increase in roll authority can be obtained through asymmetry, and correspondingly augmented control over lateral-directional stability through symmetric folding. It was also found that the system's effectiveness was highly dependent on the dynamic pressure, with roll-reversal occurring at negative angles of attack. An aircraft configuration exhibiting an outboard dihedral breakpoint is depicted by the right aircraft in Figure 2.5, with the breakpoint located at a 50% span.

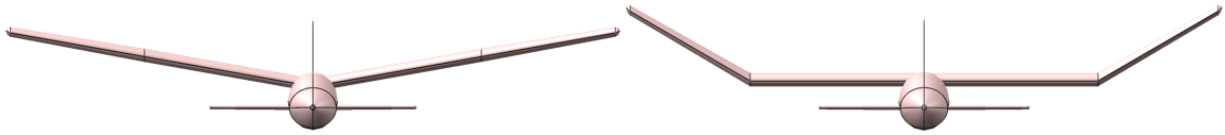

Figure 2.5: Standard dihedral vs. outboard dihedral breakpoint configuration

Previous studies have also been conducted by NASA in regards to the modification of the breakpoint configuration. NASA Report 548 [11] outlines the effects of transitioning the breakpoint to various spanwise locations. Wind tunnel experiments were conducted to study the characteristics of dihedral and wingtip shape on various Clark Y wings that would affect lateral stability and overall wing performance. A sample set of wing configurations tested are shown in Figure 2.6 [11]; similar configurations will be used for the basis of this study.

The study concluded that the dihedral effect was maintained at higher angles of attack with only the outboard sections of the wing containing a dihedral angle. The report also concluded that the theoretical prediction of C_{l_β} for the wing was within a tolerance of the experimental results, leading to a method of estimating C_{l_β} for the rectangular Clark Y wing.

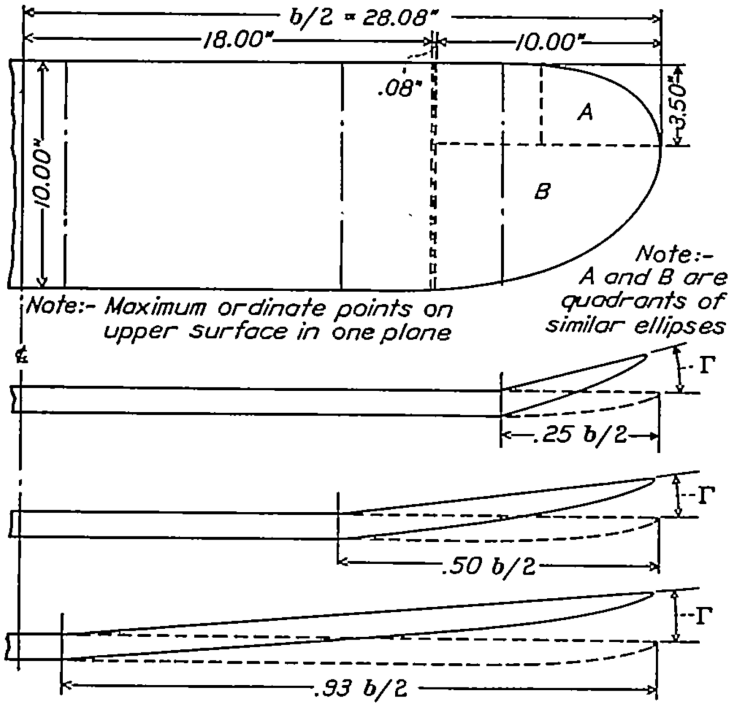

Figure 2.6: NASA wing platform used in variable dihedral breakpoint study, showing breakpoints at 7%, 50%, and 75% span [11]

Through additional review, the experimental data reveals that lateral-directional stability characteristics maintained through C_{l_β} can be held at various configurations. Sample data from Report 548 [11] is shown in Figure 2.7.

The report indicates that the change in C_{l_β} across configurations must be added to any additional dihedral effects (i.e. vertical stabilizer) for the aircraft. Notionally, the raw values for C_{l_β} will vary with airfoil, wing platform, and angle of attack. All angles of attack assessed from the paper were evaluated at $\alpha = 0°$. Figure 2.7 shows three curves corresponding to dihedral breakpoints located outboard, with 7% being closest and 75% being furthest from the root. The plot indicates, for example, that with a breakpoint of 7% and dihedral angle of 5°, a similar ΔC_{l_β} can be obtained using a configuration with a breakpoint of 75% and dihedral angle of 18°. These findings indicate that similar lateral-directional stability

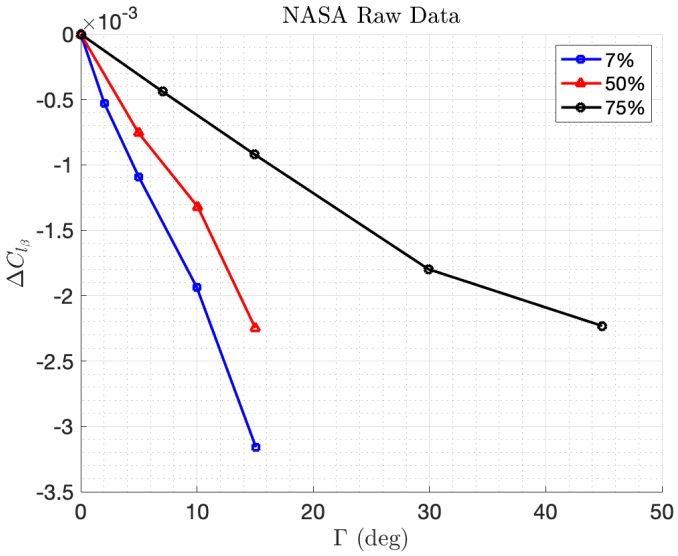

Figure 2.7: NASA wind tunnel estimates for change in Cl_β with respect to Γ for dihedral breakpoints of 7%, 50%, and 75% span [11]

properties can be maintained across various dihedral and wing breakpoint configurations, which this study investigates in the context of active dihedral.

Chapter 3

Methods of Modeling

3.1 The Dihedral Effect

An overview of the dihedral effect was provided in Section 2.2. A more in-depth investigation of the dihedral effect and its implications on the force and moment equations is provided here. Assume the aircraft enters a sideslip at an angle β, shown in Figure 2.2, experiencing a differential in normal velocity on the right wing compared to the left wing. The corresponding normal velocities were given in Equations (2.1) and (2.2). A two-dimensional depiction of the normal forces encountered is found in Figure 3.1. Due to this change in normal velocity, the angle of attack for each wing was modified, indicated by Equations (2.3) and (2.4). This differential in angle of attack leads to change in lift on each wing, corresponding to an induced rolling moment. The change in rolling moment coefficient

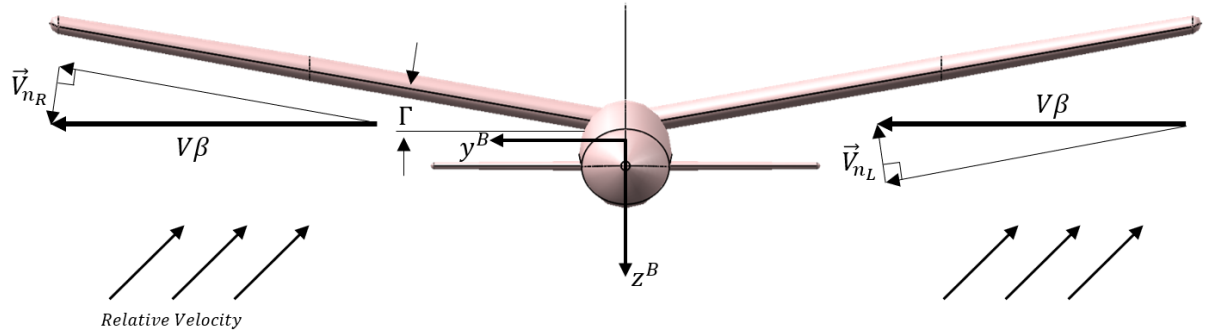

Figure 3.1: Front view of aircraft entering a sideslip, encountering a differential normal force on the left (V_{n_L}) and right (V_{n_R}) wing, altering the angle of attack for each side

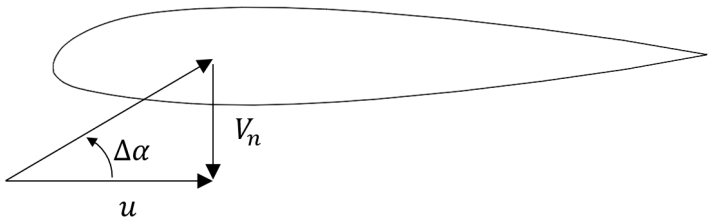

Figure 3.2: 2-D airfoil view when aircraft wing at zero angle of attack encounters a sideslip with dihedral, making the normal velocity, V_n, non-zero

is given as follows [5]:

$$\Delta C_l = \frac{\Delta L}{QSb} = -\frac{1}{2}(C_{L_\alpha}(\beta\Gamma)\frac{\bar{y}}{b} + C_{L_\alpha}(-\beta\Gamma)\frac{-\bar{y}}{b}) = -C_{L_\alpha}\Gamma\frac{\bar{y}}{b}\beta \tag{3.1}$$

The parameter $\bar{y}$ is the lateral distance from the center of gravity to the center of lift. The estimation of C_{l_β} is obtained by differentiating Equation (3.1) with respect to β [5]:

$$C_{l_\beta} = -C_{L_\alpha}\Gamma\frac{\bar{y}}{b} \tag{3.2}$$

Assuming a positive C_{L_α} and Γ, which is representative for conventional aircraft, there exists a restoring rolling moment due to a negative C_{l_β}. If Γ were to be negative, considered as anhedral, a positive C_{l_β} is created, leading to an unstable configuration such that the aircraft will continue to roll when entering a sideslip.

To incorporate the dihedral effect in the equations of motion, it was necessary to add the change in angle of attack to the aerodynamic forces and moments. The corresponding change in angle of attack for the right wing is defined as:

$$\Delta\alpha_R = \Gamma\beta \tag{3.3}$$

The change in angle of attack for the left wing is:

$$\Delta\alpha_L = -\Gamma\beta \tag{3.4}$$

3.2 The Flapping Effect

Consider an aircraft with $\Gamma = 0$ that is capable of flapping its wings from this static configuration. The effect of flapping the wings through a controller generates a similar effect to that of a roll rate experienced by the wings, where a positive flapping rate, $\dot{\Gamma}$, indicates both wings are flapping in the positive Γ direction, equivalently rotating upwards. This results in a direct change of angle of attack, with the right wing experiencing a negative roll rate (decreased angle of attack) and the left wing encountering a positive roll rate (decreased angle of attack), leading to the corresponding decrease in lift due to flapping. The converse holds, as well, with a negative flapping rate generating an increased angle of attack for both wings. Note that this flapping phenomenon, while dependent on the changing dihedral angle, is distinct from the dihedral effect. The direct lift generated from flapping motion is dependent on the dihedral angle, as the vertical lift generated when the wings flap from $\Gamma \geq 0°$ is directly proportional to $\cos(\Gamma)$. The rate of change in wing dihedral, $\dot{\Gamma}$, directly determines the change in angle of attack as a function of spanwise location.

$$\Delta\alpha(y) = \tan\left(\frac{-\dot{\Gamma}y}{u}\right) \approx -\frac{\dot{\Gamma}y}{u} \tag{3.5}$$

Figure 3.3 depicts the flapping wing motion for an aircraft actuating the wings about the root. The aircraft begins at a positive dihedral angle and flaps downwards with $\dot{\Gamma} < 0\frac{°}{\text{sec}}$, stopping at $\Gamma = 0°$. The total change in dihedral angle is referenced as $\Delta\Gamma$. The change in local angle of attack perceived by an airfoil cross-section can be computed using Equation

(3.5). The local-normal velocity experienced by the cross-section is observed as a function of spanwise location, y, with the $y = \frac{b}{2}$ having the larger normal velocity component. The root does not generate any additional lift. The total change in lift generated at this cross-sectional

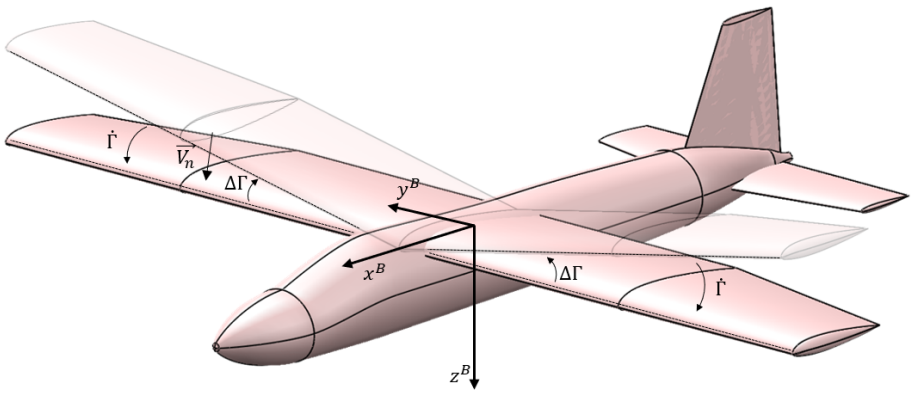

Figure 3.3: Flapping of the active dihedral system from a $+\Gamma$ to $\Gamma = 0°$, at a rate of $\dot{\Gamma}$, with the dihedral breakpoint located at the root

location due to altering the localized cross-section flow profile can be defined as follows:

$$dL_{\text{flapping}} = \frac{1}{2}\rho c(y) C_{l_\alpha}(y) \left(\frac{-\dot{\Gamma}y}{u}\right) (u^2 + (\dot{\Gamma}y)^2)\, dy \tag{3.6}$$

Assuming the local downward velocity of the wing, $(\dot{\Gamma}y)^2$, is much less than u^2, then it can be approximated for this cross-section of the wing, the differential contribution to lift from flapping is:

$$dL_{\text{flapping}} \approx -\frac{1}{2}\rho c(y) C_{l_\alpha}(y) \dot{\Gamma} y u\, dy \tag{3.7}$$

With the assumption of a constant chord, Equation (3.7) can be integrated along the wing, giving total lift generated due to actuating the wings. The instantaneous lift generated by the entire wing is:

$$L_{\text{flapping}} = -\frac{1}{8}\rho C_{L_\alpha} \dot{\Gamma} c b^2 u \tag{3.8}$$

Equation (3.8) indicates a positive $\dot{\Gamma}$ rotates the wing upwards, generating a downward force along the z^B axis. The converse is true with a negative $\dot{\Gamma}$, where the wing flaps downwards, generating a force upwards.

The previous set of equations was evaluated only with $\Gamma = 0$, as the entirety of the normal force created by the wing is aligned with the lift direction. It is of concern that the previous set of equations is not valid for an aircraft with a greater dihedral angle, noting that the normal force vector generated by the aircraft is not aligned with the lift vector. To account for this, the aircraft's instantaneous dihedral angle must be considered to properly rotate the differential in normal force due to the flapping effect, projecting the normal force onto the z^B axis. To project the normal force onto the z^B axis, the following rotation matrix must be applied:

$$R_{NL}(\Gamma) = R_x(\Gamma) = \begin{bmatrix} 1 & 0 & 0 \\ 0 & \cos(\Gamma) & -\sin(\Gamma) \\ 0 & \sin(\Gamma) & \cos(\Gamma) \end{bmatrix} \tag{3.9}$$

For positive dihedral angles, a negative rotation must be performed to determine the body force components. The projected vector for the right wing is defined in Equation (3.10).

$$\vec{F}_{\text{flapping}} = R_{NL}(-\Gamma) \begin{bmatrix} 0 \\ 0 \\ -\frac{1}{4u} C_{L_\alpha} \dot{\Gamma} b^2 \end{bmatrix} = \frac{1}{4u} C_{L_\alpha} \dot{\Gamma} b^2 \sin\Gamma \, \hat{j} + -\frac{1}{4u} C_{L_\alpha} \dot{\Gamma} b^2 \cos\Gamma \, \hat{k} \tag{3.10}$$

The rotation of the wing's normal force onto y^B and z^B axes leads to the lift and side force components. Of concern for this study is the component along the z^B axis, as this will contribute to vertical gust rejection. It is expected that the lateral force generated due to the flapping effect will cancel due to the aircraft symmetry. The derivation provided here, culminating in Equation (3.10), was used to show the total lift generated due to flapping

at an instantaneous dihedral angle. Due to the spanwise variation of chord and lift properties, Equation (3.5) is incorporated into the aerodynamic forces and moments to model the flapping effect. This provided increased model accuracy compared to the assumptions used to define Equation (3.10); the derivation shows the considerations required for modeling the flapping effect appropriately. The model also enforces the use of the full dihedral angle component (e.g. no small angle approximation) in terms of applying the rotation denoted in Equation (3.9).

It was important to distinguish the lift due to the flapping effect and the lift generated from the wing being fixed at an alternative non-equilibrium dihedral angle. For example, while flapping the wing downwards starting from a positive dihedral angle, an upward force is generated from flapping. Due to the now reduced dihedral angle, the wing normal force vector is angled such that the projected component onto the z^B axis is increased in magnitude, generating more lift independent of flapping. Distinguishing the two sources of lift force leads to an improved understanding of the variation of aircraft configurations and the anticipated system's response to perturbations. It is also acknowledged that the flapping effect modeled neglects the aerodynamic interaction of the wing and fuselage, in which the fluid dynamics near the root are modified with flapping. As well, the inertial interaction of the flapping wing with the fuselage, which occurs through the conservation of momentum, is neglected. Consider a large input torque to the wing from the actuation system, with the actuation system hosted internally to the fuselage. Conservation of angular momentum implies an equal and opposite torque is experienced by the housing hosting the actuation system, causing the fuselage to be perturbed. This effect is neglected in this study as the aircraft is treated as a rigid body.

3.3 Roll Damping

Consider the roll rate, p, and its effect on the angle of attack along each wing, commonly denoted as the roll damping term, C_{l_p}. A roll moment generated by an aircraft is commonly induced through a lift differential between the wings generated by rolling, turbulence, aileron deflection, or yaw rate. The roll damping term is of increased interest due to its similarity to the flapping effect, generated through $\dot{\Gamma}$. Begin by establishing the distance between the center of gravity and the acting center of lift in the spanwise direction, denoted by $\bar{y}$. For an elliptic wing $\bar{y}$ would correspond to $\frac{4}{3\pi}\frac{b}{2}$ and the effect of p would be linear in the dynamic equations, observed as:

$$\Delta\alpha = \tan\left(\frac{\bar{y}p}{u_0}\right) \approx \frac{\bar{y}p}{u_0} \tag{3.11}$$

A formula for increased modeling accuracy is imposed for a wing with a non-elliptic lift distribution, with varying spanwise parameters such as c and C_{l_α}. The general formula for roll damping at a spanwise cross-section on the right wing is:

$$\Delta\alpha_R(y) = \frac{yp}{u} \tag{3.12}$$

A positive roll rate induces an increase in the angle of attack on the right wing and a decreased angle of attack on the left wing. The contribution of roll damping is included in the aircraft model due to its similarity to the flapping effect.

3.4 Effect of Dihedral on Ailerons

Ailerons are placed outboard an aircraft as means of roll authority for banking and turning the vehicle. For an aircraft maintaining a fixed dihedral angle, a side force is gener-

ated by the deflection of the ailerons. This side force can be advantageous when attempting to maintain a trajectory, however, it can also be considered adverse in attitude control when attempting to maintain $\phi = 0°$ due to reduced roll authority. Figure 3.4 shows the forces generated when actuating the ailerons, inducing this side force effect. A set of equations can

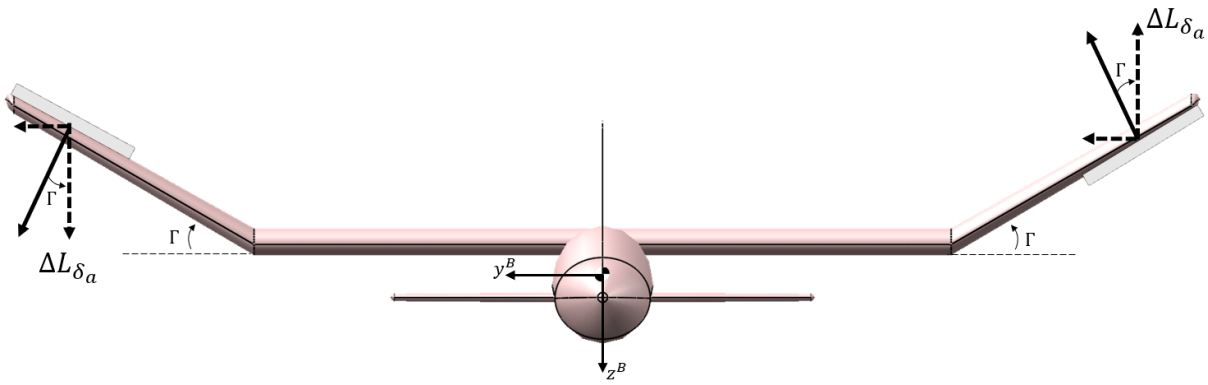

Figure 3.4: Aircraft with dihedral employed show positive side force generated when actuating ailerons, with the right-wing deflecting upwards, generating negative lift, and reciprocally for the left wing

be derived estimating the side force generated by the ailerons, coupled with the change in roll moment. Begin with the traditional piece-wise differential spanwise lift contribution.

$$\Delta\text{Lift}(y) = \begin{cases} 0, & 0 < y < y_1 \\ -(C_{L_{\delta_a}}\delta_a)q_\infty c(y), & y_1 \leq y \leq y_2 \\ 0, & y_2 \leq y \leq \frac{b}{2} \end{cases} \tag{3.13}$$

where $C_{L_{\delta_a}}$, the aileron effectiveness, is defined as:

$$C_{L_{\delta_a}} = C_{L_{\alpha_w}}\tau_a \tag{3.14}$$

The aileron effectiveness parameter, τ_a, can be estimated using a mapping from the control surface to wing chord ratio defined by Sadraey [12]. The term y_1 corresponds to the spanwise

position where the ailerons begin and y_2 is the spanwise position where the aileron ends. Note that $y_1 < y_2$, $0 \leq y_1$ and $y_2 \leq \frac{b}{2}$. From Equation (3.13), the net force, due to dihedral, contributing to the lateral motion can be denoted as:

$$Y_{\delta_a} = -2\sin(\Gamma)\int_0^{b/2} \Delta\text{Lift}(y)\,dx \tag{3.15}$$

The adverse side force is of significant importance in modeling the aircraft's response to aileron deflection at various dihedral angles. In the traditional linearized set of dynamic equations, the Y_v term (notionally Y_β) is characterized by a static C_{Y_β}. Analytically, this stability derivative is commonly assessed by factoring only the vertical stabilizer and its associated properties, including $C_{L_{\alpha_{vt}}}$, S_{vt}, and $\frac{d\sigma}{d\beta}$ (sensitivity of sidewash angle σ to β). Depending on the dihedral angle of the aircraft being assessed, the contribution of adverse side force from the wings, independent of ailerons, can become of similar magnitude to that of the vertical tail. Birds have no vertical stabilizer to impact C_{Y_β}, and hence this side force at high dihedral angles is used to their advantage in steering. Similarly, in the case of active dihedral, at higher dihedral angles there exists greater authority in maintaining a lateral position [3]. This implies that less aileron is required to maintain a directional course, reducing the required change in roll attitude to return to a specified trajectory.

While the dihedral angle provides this increased lateral authority, the roll authority remains constant assuming the dihedral breakpoint is located at the root, as the acting roll moment arm remains unmodified. The total roll moment generated by the aircraft's ailerons is given as follows:

$$\Delta L_{\text{roll}} = -2\int_0^{b/2} y\Delta\text{Lift}(y)\,dy \tag{3.16}$$

where the conventional non-dimensional form of roll moment due to aileron is computed as:

$$C_{l_{\text{aileron}}} = \frac{2C_{L_{\alpha_w}}\tau\delta_a}{Sb}\int_{y_1}^{y_2} c(y)y\,dy \tag{3.17}$$

3.5 Spanwise Lift Variation

The aerodynamic parameter C_{L_α} is frequently considered fixed for the wing planform when used in the aircraft equations of motion. For active dihedral, this assumption is insufficient as the root exhibits a greater coefficient of lift than the outboard portion of the wing for a constant chord aircraft with no twist. For a flapping-wing aircraft, it is proper to model the spanwise aerodynamic forces, C_l and C_d, as this would significantly modify the impacts of the dihedral effect and flapping effect.

Figure 3.5 indicates how the lift vectors were approximated for this study. The lift for the inner wing section was computed using the integrated lift distribution, indicated by $L_{R_{\text{inner}}}$, with the center of lift assumed at the midpoint, $\bar{y}_{\text{inner}}$. This assumption was considered valid due to the zero dihedral angle in this section. The normal force generated by the outer wing section, $L_{L_{\text{outer}}}$, contributing to the dihedral effect and flapping effect, was computed through the integrated lift distribution. The center of lift for this section was given by $\bar{y}_{\text{outer}}$, calculated based on the outboard lift distribution. Due to the significant contribution of C_{L_α} on C_{l_β}, indicated in Equation (3.2), it was necessary to properly model C_l, C_{l_α}, and the point which the force was acting in the spanwise direction. These aerodynamic parameters and their variation across the span can be estimated using numerical methods such as the Vortex Lattice Method (VLM).

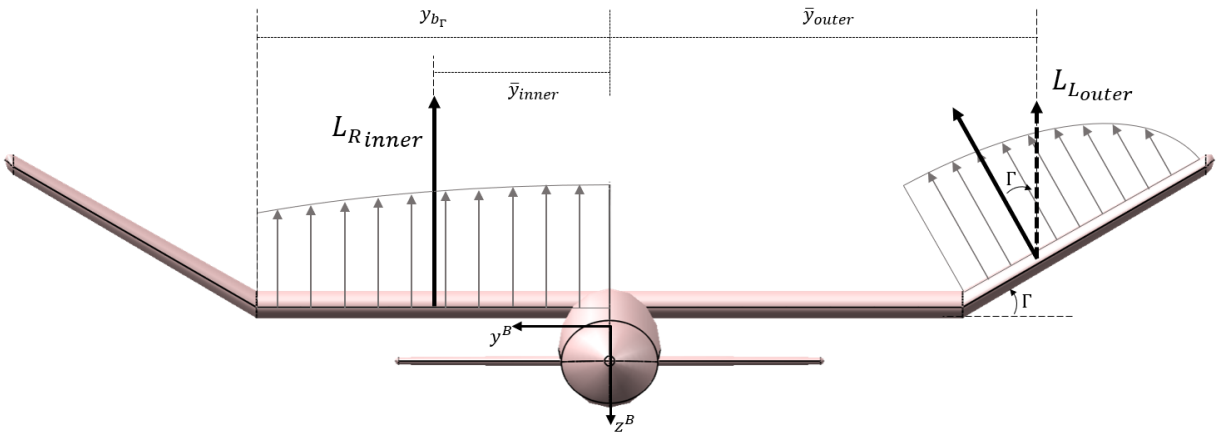

Figure 3.5: Lift distribution for inner and outer sections of the wing, with L_{inner} approximately located at the inner section midpoint, and L_{outer} located at the center of lift for the outboard section.

3.6 Dynamic and Kinematic Equations of Motion

To model the motion of an aircraft, it is required that a rigid body system be defined such that the dynamics of the system can be reduced to a set of first-order differential equations. The aircraft is treated as a single rigid body in space, having six degrees of freedom, with the aircraft's kinematics and dynamics being modeled about this point. In its simplest form, the system is composed of forces, moments, masses, and inertia, for which the six degrees of freedom can be modeled.

There are three primary coordinate frames of interest in this study: the body-fixed frame, stability frame, and earth-fixed frame. Each of these coordinate frames is depicted in Figure 3.6. The body-fixed coordinate system is assumed fixed at the vehicle's center of mass, due to the rigid body assumption, with the x^B, y^B, and z^B axes being positive out of the nose, the right wing, and the aircraft's downward direction. With an active dihedral system, the right wing will actuate, but the body-frame remains fixed. The stability frame corresponds with the instantaneous location of the relative wind velocity vector. The x^S axis

sits at an angle of α below the x^B axis, with z^S axis rotated similarly. The y^S axis remains collinear with y^B axis, acting as a rotation axis for x^S and z^S. The angle in which the velocity vector is offset from the $x^S z^S$ plane is the sideslip angle β. The earth fixed system is the corresponding inertial frame of reference in which the rigid body operates. The x^E, y^E, and z^E axes of the frame correspond to the north, east, and down directions from any fixed point in space.

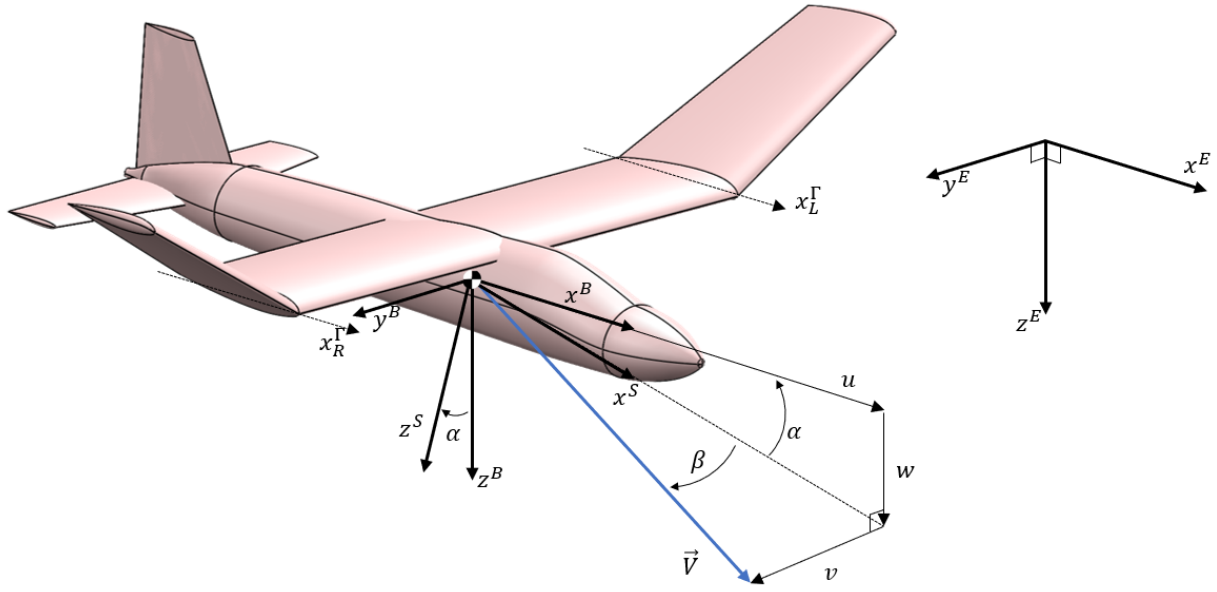

Figure 3.6: Body, stability, and earth-fixed coordinate systems describe relevant reference frames to the problem. The dihedral actuation axis is shown for a non-zero breakpoint dihedral angle.

Assuming a flat-earth approximation, Euler's equations give the force and moment equations necessary to model the aircraft's dynamics and kinematics. Etkin and Reid explain the 12 total state equations, 6 dynamic and 6 kinematic, which can be used to model the vehicle [13]. The 12 states modeled are x_e, y_e, z_e, ϕ, θ, ψ, u, v, w, p, q, and r. The x_e, y_e, and z_e states determine the vehicle's northern, eastern, and downward position in the earth-fixed frame, from a fixed point in space. The Euler angles, ϕ, θ, and ψ, give the aircraft's roll, pitch, and yaw (or heading) angle with respect to the earth-fixed frame. The states u, v,

and w are velocities expressed in the body-fixed frame, corresponding to the x^B, y^B, and z^B axes respectively. The body-fixed angular velocities, given by p, q, and r, correspond to the roll, pitch, and yaw axes, respectively.

The 12 equations associated with these states are given as follows. The translational forces on the aircraft and their effect on the translational acceleration are given in Equations (3.18)-(3.20). The associated kinematic relationships to the inertial frame are given in Equations (3.21)-(3.23).

$$X = m(\dot{u} + qw - rv + g\sin\theta) \tag{3.18}$$

$$Y = m(\dot{v} + ru - pw - g\cos\theta\sin\phi) \tag{3.19}$$

$$Z = m(\dot{w} + pv - qu - g\cos\theta\cos\phi) \tag{3.20}$$

$$\dot{x}_e = u(\cos\theta\cos\psi) + v(\sin\phi\sin\theta\cos\phi - \cos\phi\sin\psi) + w(\sin\phi\sin\psi + \cos\phi\sin\theta\cos\psi) \tag{3.21}$$

$$\dot{y}_e = u(\cos\theta\sin\psi) + v(\sin\phi\sin\theta\sin\phi + \cos\phi\cos\psi) + w(-\sin\phi\cos\psi + \cos\phi\sin\theta\sin\psi) \tag{3.22}$$

$$\dot{z}_e = u(-\sin\theta) + v(\sin\phi\cos\theta) + w(\cos\phi\cos\theta) \tag{3.23}$$

The moments encountered by the system are captured in the rotational dynamics, given in Equations (3.24)-(3.26). The corresponding rotational kinematic equations, modeling the attitude profile of the aircraft using Euler angles and associated rates, are provided in Equations (3.27)-(3.29).

$$L = I_x\dot{p} - I_{yz}(q^2 - r^2) - I_{zx}(\dot{r} + pq) - I_{xy}(\dot{q} - rp) - (I_y - I_z)qr \tag{3.24}$$

$$M = I_y\dot{q} - I_{zx}(r^2 - p^2) - I_{xy}(\dot{p} - qr) - I_{yz}(\dot{r} - pq) - (I_z - I_x)rp \tag{3.25}$$

$$N = I_z\dot{r} - I_{xy}(p^2 - q^2) - I_{yz}(\dot{q} - rp) - I_{zx}(\dot{p} - qr) - (I_x - I_y)pq \tag{3.26}$$

$$p = \dot{\phi} - \dot{\psi}\sin\theta \tag{3.27}$$

$$q = \dot{\theta}\cos\phi + \dot{\psi}\sin\psi\cos\theta \tag{3.28}$$

$$r = -\dot{\theta}\sin\phi + \dot{\psi}\cos\psi\cos\theta \tag{3.29}$$

Throughout this study, it is assumed that the dihedral of the aircraft is actuated symmetrically about the $C_{x^B z^B}$ plane of the aircraft, and therefore implies symmetry about this plane. Due to this, $I_{xy} = I_{yz} = 0$, simplifying the equations. If all measurements are taken from the center of gravity, and the axes principal, then I_{zx} also reduces to zero. This study assumes the axes are principal, hence Equations (3.24)-(3.26) simplify to Equations (3.30)-(3.32).

$$L = I_x\dot{p} - (I_y - I_z)qr \tag{3.30}$$

$$M = I_y\dot{q} - (I_z - I_x)rp \tag{3.31}$$

$$N = I_z\dot{r} - (I_x - I_y)pq \tag{3.32}$$

It is acknowledged that this simplification may not hold at higher dihedral angles. This assumption is held to reduce the order of complexity of the LPV system, restricting the study's scope from the inertial impacts of flapping wing vehicles. It is known this decision could reduce the accuracy of the system's pitch dynamics, directly affecting the total lift produced [14].

An additional axis of reference that must be considered is the dihedral rotation axis. The dihedral rotation axis, x^Γ, an axis parallel to x^B, was assigned to allow for the characterization of an active dihedral system and its associated dynamics. The x^Γ axis is depicted in Figure 3.6. The x^Γ axis remains fixed along the chord line which the active dihedral

system is actuating; this chord line can be a fixed angle offset from the body axis, such as the wing incidence angle, i_w. If the wing incidence angle is zero, which is assumed during this study, the x^Γ axis is located in the $C_{x^B y^B}$ plane. The distance from x^Γ to the x^B axis is given by $\frac{b}{2} y_{b_\Gamma}$. Defining a positive and negative rotation, the right hand rule is used for the left wing, and conversely the left hand rule for the right wing. Using this convention ensures that at $\Gamma = 0°$, a positive rotation of the wing gives a positive dihedral angle for both sides. Stemming from this axis definition, there exists a single equation of motion used to describe the rotation induced through applied torque, δ_τ, to the dihedral system, given by Equation (3.33).

$$\ddot{\Gamma}(\delta_\tau) = \frac{\delta_\tau}{I_W} \tag{3.33}$$

The equation for applied torque from the actuator undermines the true total torque required to counteract the aerodynamic forces and moments generated by the aircraft wing, as only the wing inertia is considered. The wing moment of inertia, I_W, was estimated using wing geometric properties, weight, and a uniform density assumption; this provided the best estimate of wing inertia. Through state-space decomposition, Equation (3.33) leads to first-order ODEs for Γ and $\dot{\Gamma}$, indicative of two additional state equations. The total number of states established for the system is 14 total, being expressed as:

$$\vec{x} = [x_e, y_e, z_e, u, v, w, p, q, r, \phi, \theta, \psi, \Gamma, \dot{\Gamma}] \tag{3.34}$$

There exists 4 conventional inputs to an aircraft that can be used for controlling the vehicle: aileron (δ_a), elevator (δ_a), rudder (δ_r), and throttle (δ_T). Equation (3.33) indicated the use of the additional torque input, δ_τ, to actuating the wing. The total number of inputs to the system is five, represented as:

$$\vec{u} = [\delta_a, \delta_e, \delta_r, \delta_T, \delta_\tau] \tag{3.35}$$

3.7 Defining Aerodynamic Forces and Moments

The forces and moments for an aircraft are commonly expressed using stability derivatives, with these factoring directly into a derived set of dynamic equations. This study takes the approach of explicitly defining the forces and moments acting on the system through the aircraft surfaces to allow for manipulation of the dynamic equations to better model the active dihedral system. The associated stability derivatives of the system can be derived thereafter. The forces and moments identified as follows are directly incorporated into the equations of motion provided in Equations (3.18)-(3.20) and Equations (3.30)-(3.32). The equations for modeling the aerodynamic forces and moments are provided here forward, however, portions of the equations related to the dihedral effect and flapping effect are highlighted to indicate where this project makes contributions to system modeling. Additional aircraft force and moment contributions, such as the fuselage, propulsion system, and vertical and horizontal stabilizer, are well documented by authors such as Etkin [1], and therefore in-depth discussion of these terms is not required. This study also assumes the effect of flapping and its implications on the horizontal stabilizer are negligible, though it has been shown the change in wake due to flapping does affect horizontal tail performance [15]. The dihedral breakpoint is assumed collinear with the x^B axis, $y_{b_\Gamma} = 0$, for the following equations.
The forces acting on the aircraft, X, Y, and Z, are given as:

$$X = -D\cos(\alpha) + L\sin(\alpha) + T \tag{3.36}$$

$$Z = -D\sin(\alpha) - L\cos(\alpha) \tag{3.37}$$

$$Y = (L_{W_L} - L_{W_R})\sin(\Gamma) + Y_{vt} \tag{3.38}$$

The lift (L) generated by the vehicle is comprised of the contributions from the wing and horizontal tail.

$$L = q_\infty \cos(\Gamma) C_{L_W} S_W + q_\infty C_{L_{ht}} S_{ht} \tag{3.39}$$

The lift generated by the wing is described such that integration across the span is possible.

$$L_W = q_\infty \cos(\Gamma) C_{L_W} S_W = q_\infty \cos(\Gamma) \left(\int_0^{\frac{b}{2}} c(y) C_{l_{W_R}}(y)\, dy + \int_0^{\frac{b}{2}} c(y) C_{l_{W_L}}(y)\, dy \right) \tag{3.40}$$

The terms $C_{l_{W_R}}$ and $C_{l_{W_L}}$, corresponding to the spanwise coefficient of lift, vary with y due to the variation in C_{l_α} and changing angle of attack with the flapping effect.

$$C_{l_{W_R}}(y) = C_{l_{\alpha=0}}(y) + C_{l_\alpha}(y) \alpha_R(y) \tag{3.41}$$

Conversely for the left wing:

$$C_{l_{W_L}}(y) = C_{l_{\alpha=0}} + C_{l_\alpha}(y) \alpha_L(y) \tag{3.42}$$

The angle of attack, α, for the wing is given by:

$$\alpha = \tan^{-1}\left(\frac{w}{u}\right) \tag{3.43}$$

While the dependency of α on spanwise location, y, is not denoted here, this dependency is described in Sections 3.2 and 3.3. The drag created by the fuselage, wing, horizontal stabilizer, and vertical stabilizer, summing to the total vehicle drag, is given as:

$$D = q_\infty C_{D_F} S_{wet,F} + q_\infty C_{D_W} S_W + q_\infty C_{D_{ht}} S_{ht} + q_\infty C_{D_{vt}} S_{vt} \tag{3.44}$$

The drag generated by the wing alone can be computed via spanwise integration for both sides of the wing.

$$D_W = q_\infty C_{D_W} S_W = q_\infty \left(\int_0^{\frac{b}{2}} c(y) C_{d_{W_R}}(y)\, dy + \int_0^{\frac{b}{2}} c(y) C_{d_{W_L}}(y)\, dy \right) \tag{3.45}$$

The drag coefficient varies across the span due to the varying spanwise lift and angle of attack. The coefficient of drag for low Reynolds numbers is the combination of the zero-lift parasite drag and the induced drag due to lift. The coefficient of drag for the right wing is defined as:

$$C_{d_{W_R}}(y) = C_{d_0} + \frac{(C_{l_{W_R}}(y))^2}{\pi A R e} \tag{3.46}$$

And correspondingly for the left wing:

$$C_{d_{W_L}}(y) = C_{d_0} + \frac{(C_{l_{W_L}}(y))^2}{\pi A R e} \tag{3.47}$$

The total aerodynamic pitching moment on the aircraft about the center of gravity is given as:

$$M = q_\infty S \bar{c} C_m \tag{3.48}$$

The parameter S corresponds to the projected wing area and the term $\bar{c}$ the mean aerodynamic chord. The moment coefficient, C_m, is defined as follows for equilibrium flight.

$$C_m = C_{m_0} + C_{m_\alpha}\alpha + C_{m_{\delta_e}}\delta_e \tag{3.49}$$

The total pitching moment generated by the wing, $C_{m_\alpha}\alpha$, is decomposed as follows:

$$C_{m_\alpha} = C_{m_{\alpha_w}} + C_{m_{\alpha_t}} + C_{m_{\alpha_f}} + C_{m_{\alpha_p}} \tag{3.50}$$

The contribution of $C_{m_{\alpha_f}}$ and $C_{m_{\alpha_p}}$ are ignored due to lack of higher-order fuselage and propulsion system characterization. Equation (3.50) can then be reduced to:

$$C_{m_\alpha} = C_{L_{\alpha_W}}(h - h_{ac_w}) - V_H C_{L_{\alpha_t}}(1 - \frac{d\epsilon}{d\alpha}) \tag{3.51}$$

The effect of the dihedral angle and flapping effect were captured in $C_{L_{\alpha_W}}$, using the lift force at a given angle of attack. The terms h and h_{ac_w} are the center of gravity and aerodynamic center, respectively, locations along the x^B axis.

The forces and moments, Y, L, and N, correlated to the lateral-directional stability derivatives, are given as follows. Consider the lateral force component Y to be comprised of contributions from the vertical tail and wing

$$Y = Y_W + Y_{vt} \tag{3.52}$$

where Y_{vt} can be defined as

$$Y_{vt} = C_{L_{\alpha_{vt}}}(-\beta + \sigma(\beta))q_\infty S_{vt} \tag{3.53}$$

with β defined in Equation (3.2). The stability derivative C_{Y_r} is expressed through the contribution of the vertical tail to side force in Equation (3.53). This term results due to Equation (3.54), indicating a sideslip induced through yaw moment.

$$\Delta\beta = -\frac{r l_{vt}}{u} \tag{3.54}$$

The contribution of the wing to side force, incorporating the dihedral angle, is:

$$Y_W = (-L_{w_R} + L_{w_L})\frac{\sin(\Gamma)}{\cos(\Gamma)} + Y_{\delta_a} \tag{3.55}$$

This equation shows that there exists a component of the force generated by the wing acting along the y^B axis, when there is a differential in lift generated by the wings, such as during a sideslip. The trigonometric terms are used to identify the projected normal force component along the y^B axis, giving the side force. This equation ensures that stability derivatives C_{Y_β} and C_{Y_p} are modeled. The aerodynamic roll moment on the aircraft is approximated by:

$$L_{\text{roll}} = L_{\text{roll}_W} + L_{\text{roll}_{vt}} \tag{3.56}$$

The contribution of L_{roll_W} and $L_{roll_{vt}}$ correspond to the wing and vertical tail, respectively. The contribution of the vertical tail to the aerodynamic roll moment is estimated by:

$$L_{\text{roll}_{vt}} = Y_{vt}\bar{y}_{vt} \tag{3.57}$$

The acting center of lift on the vertical stabilizer was $\bar{y}_{vt}$, and Y_{vt} was previously defined in Equation (3.53). The contribution of the wing to roll moment is given in Equation (3.58).

$$L_{\text{roll}_W} = (-L_{W_R} + L_{W_L})\bar{y} \tag{3.58}$$

The acting center of lift on the wing, $\bar{y}$, is assumed fixed with variation in dihedral angle. It was expected that the acting arm distance from the center of gravity to the center of lift shifts marginally with a change in dihedral angle. The stability derivatives, C_{l_β} and C_{l_p} are reflected in this roll moment term, with the dihedral effect and roll damping are incorporated in the equations for L_{W_R} and L_{W_L}. Modeling of the effect drag has on the pitching moment was neglected, as at lower dihedral angles, it is near zero. At larger values of Γ, the active drag force location exists well above the center of gravity, generating additional positive pitching moment; this can be incorporated in future models.

The aerodynamic yaw moment on the aircraft is defined as:

$$N = N_W + N_{vt} \tag{3.59}$$

The vertical tail primarily contributes to the yaw moment, due to its weather vane-like response to sideslip. The contribution of the vertical tail is defined as:

$$N_{vt} = l_{vt} Y_{vt} \tag{3.60}$$

The distance along the x^B axis from the center of gravity to the aerodynamic center of the vertical stabilizer is defined as l_{vt}. The contribution of the wing to this term results from a differential in drag, obtained in instances of differential lift. The formulation for N_W is:

$$N_W = (D_{W_R} - D_{W_L})\bar{y} \tag{3.61}$$

Similar to the pitching moment, the yaw moment could include a dependency on the dihedral angle. An increased dihedral angle results in the drag forces from each wing being located closer z^B, reducing the net yaw moment. This could be incorporated in future models.

These equations summarize the primary contributing forces and moments required for modeling the active dihedral system. It is necessary for the various effects described in Sections 3.1, 3.2, 3.3, 3.4, and 3.5, to be included in aerodynamic forces and moments equations. Discussion of the fuselage, propulsion system, elevator, and rudder contributions to the forces and moments are not explicitly designated or derived for all equations shown, however, their relevance to the dihedral effect and flapping effect is described as necessary. These terms are included in the equations of motion through means described by Etkin [1], as they are required for building a baseline controller for gust rejection evaluation.

3.8 Effects of a Varying Breakpoint Dihedral on Equations of Motion

There existed a need to re-define the aerodynamic forces and moments generated by an alternative dihedral breakpoint, describe by the term y_{b_Γ}, for the aircraft. The primary force and moment changes occur due to modeling the inner and outer wing sections differently. The inner section of the wing is modeled as a fixed-wing with $\Gamma = 0$, and the outer wing is modeled similar to previously, incorporating the dihedral effect and flapping effect.

3.8.1 Aerodynamic Forces

Begin by defining the dihedral breakpoint, y_{b_Γ}, as the outboard point in which the dihedral begins, given as a percentage in terms of half span. The term y_{b_Γ} can range from 0% to 100%, with 0% corresponding to a breakpoint at the root, and 100% corresponding to a breakpoint at the wingtip ($\frac{b}{2}$). The lift on the inner portion of the wing, with a dihedral angle of zero, is defined as follows:

$$L_{R_{\text{inner}}} = q_\infty \int_0^{y_{b_\Gamma}\frac{b}{2}} c(y) C_{l_{W_R}}(y)\, dy \tag{3.62}$$

Similar to Equation (3.41), $C_{l_{W_{R_{\text{inner}}}}}$ is defined for the inner portion as:

$$C_{l_{W_{R_{\text{inner}}}}}(y) = C_{l_{\alpha=0}}(y) + C_{l_\alpha}(y)\alpha_{R_{\text{inner}}}(y) \tag{3.63}$$

Note that the integration of this portion of the wing is only from the root to the breakpoint. The angle of attack for the inner right wing is defined as follows:

$$\alpha_{R_{\text{inner}}}(y) = \alpha + \frac{yp}{u} \tag{3.64}$$

The additional term due to roll damping is still incorporated, however, the flapping effect and dihedral effect are negated due to the inner portion of the wing included in the active dihedral system. Defining the lift generated by the inboard portion of the left wing, taking a similar form to Equation (3.62):

$$L_{L_{\text{inner}}} = q_\infty \int_0^{y_{b_\Gamma}\frac{b}{2}} c(y) C_{l_{W_L}}(y)\, dy \tag{3.65}$$

The term $C_{l_{W_{L_{\text{inner}}}}}$ is defined similarly to Equation (3.63), except with $\alpha_{L_{\text{inner}}}$ being subjected to the opposing roll damping:

$$\alpha_{L_{\text{inner}}}(y) = \alpha - \frac{yp}{u} \tag{3.66}$$

Due to the normal force vector generated by the inner portion of the wing being aligned with the negative z^B axis, seen previously in Figure 3.5, there is no need for additional rotation of the vector. The term was factored directly into aerodynamic force Z.

The drag forces for the inner and outer wings must also be defined independently due to induced drag's dependence on the lift generated. The drag for the inner right wing is given as:

$$D_{W_{R_{\text{inner}}}} = q_\infty \int_0^{y_{b_\Gamma}\frac{b}{2}} c(y) C_{d_{W_{R_{\text{inner}}}}}(y)\, dy \tag{3.67}$$

The integration across the wing was subject only from the root to y_{b_Γ}. The coefficient of drag was defined as:

$$C_{d_{W_{R_{\text{inner}}}}}(y) = C_{d_0} + \frac{(C_{l_{W_{R_{\text{inner}}}}}(y))^2}{\pi ARe} \tag{3.68}$$

With $C_{l_{W_{R_{\text{inner}}}}}$ being defined in Equation (3.63). Conversely, for the left wing, the term $D_{W_{L_{\text{inner}}}}$ was given as:

$$D_{W_{L_{\text{inner}}}} = q_\infty \int_0^{y_{b_\Gamma}\frac{b}{2}} c(y) C_{d_{W_{L_{\text{inner}}}}}(y)\, dy \tag{3.69}$$

Where $C_{d_{W_{L_{\text{inner}}}}}$ is similar to Equation (3.68), but being dependent on $C_{l_{W_{L_{\text{inner}}}}}$. These terms were denoted with intention of highlighting no intrinsic coupling to the dihedral effect or flapping effect.

The forces acting on the outboard wing section, where $y \geq y_{b_\Gamma}\frac{b}{2}$ and the dihedral angle is in effect, are defined as follows. The lift generated by the outer right wing is computed as:

$$L_{R_{\text{outer}}} = q_\infty \cos(\Gamma) \int_{y_{b_\Gamma}\frac{b}{2}}^{\frac{b}{2}} c(y) C_{l_{W_{R_{\text{outer}}}}}(y)\, dy \tag{3.70}$$

With $C_{l_{W_{R_{\text{outer}}}}}$ being defined as in Equation (3.41), except the angle of attack for the outer wing was modified to account for the dihedral effect and flapping effect, given in Equation (3.71).

$$\alpha_{R_{\text{outer}}}(y) = \alpha + \frac{yp}{u} + \Gamma\beta - \frac{\dot{\Gamma}(y - y_{b_\Gamma}\frac{b}{2})}{u} \tag{3.71}$$

The dihedral effect is approximated by $\Gamma\beta$. The rolling damping term, $\frac{yp}{u}$, is approximated by the distance to the spanwise cross-section when the wing has $y_{b_\Gamma} = 0$, given as $\bar{y}_{\text{outer}}$. Figure 3.7 shows how the dihedral angle is required to most accurately model the roll damping, as the true arm length is longer than the estimated $\bar{y}_{\text{outer}}$ used in the roll damping term. The approximation shortens the effective arm in which the roll damping is acting. This assumption was assumed for all dihedral angles and breakpoints.

Neglecting the effect of dihedral angle on the change in this roll damping effect has a small impact on the total moment arm, with approximately an 8% maximum reduction

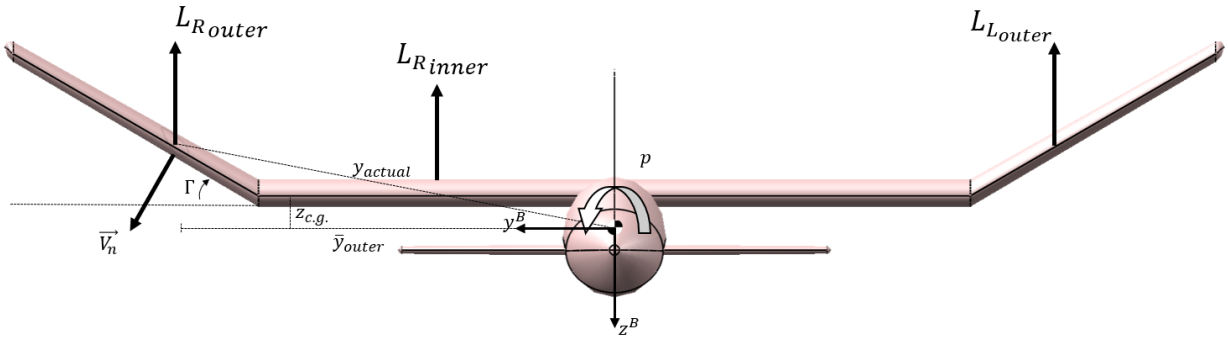

Figure 3.7: Aircraft with $y_{b_\Gamma} = 50\%$ and $\Gamma = 30°$, showing lift moment arm approximation contributing to the rolling moment.

of acting arm length for the roll moment. This maximum occurs with a dihedral angle of 30° and $y_{b_\Gamma} = 40\%$. The error in this measurement can be considered within reason, as the movement of z_{cg} will alter the approximation error as depicted in Figure 3.7. Additionally, notice the term containing $\dot{\Gamma}$ modeling the flapping effect, in Equation (3.71), which was modified from the previous definition in Equation (3.5). The new equation accounts for the hinge point of flapping being shifted outboard, meaning that at $y = y_{b_\Gamma}$, the $\dot{\Gamma}$ term resolves to zero as the local cross-section is fixed. Increased model accuracy is obtained by updating this term, removing an artificially increased flapping effect due to a large moment arm. Similar to the right wing outboard section in Equation (3.70), the lift generated by the left wing outboard section is given as:

$$L_{L_{\text{outer}}} = q_\infty \cos(\Gamma) \int_{y_{b_\Gamma}\frac{b}{2}}^{\frac{b}{2}} c(y) C_{l_{W_L}}(y)\, dy \tag{3.72}$$

With the coefficient of lift for the outer portion of the left wing is defined similarly to (3.42), except the angle of attack is defined by Equation (3.73).

$$\alpha_{L_{\text{outer}}}(y) = \alpha - \frac{yp}{u} - \Gamma\beta - \frac{\dot{\Gamma}(y - y_{b_\Gamma}\frac{b}{2})}{u} \tag{3.73}$$

The definition for the left outboard portion of the wing takes a similar form to that of Equation (3.71), but with the signs altered respectively for the dihedral effect and roll damping effect. All normal force generated by the wing with $y > y_{b_\Gamma}$ incorporates the projection of the normal force generated onto the z^B axis using the rotation matrix defined in Equation (3.9), seen as $\cos\Gamma$ in Equations (3.70) and (3.72).

It is also necessary to define the drag for the outboard portion of the wing. The drag for the right side of the wing outboard of y_{b_Γ} is defined as:

$$D_{W_{R_{\text{outer}}}} = q_\infty \int_{y_{b_\Gamma}}^{\frac{b}{2}} c(y) C_{D_{W_{R_{\text{outer}}}}}(y)\, dy \tag{3.74}$$

With $C_{d_{W_{R_{\text{outer}}}}}$ defined as:

$$C_{d_{W_{R_{\text{outer}}}}}(y) = C_{d_0} + \frac{(C_{l_{W_{R_{\text{outer}}}}}(y))^2}{\pi A R e} \tag{3.75}$$

The parasitic drag component remains unchanged with location along the wing. Comparably, the drag for the left side is:

$$D_{W_{L_{\text{outer}}}} = q_\infty \int_{y_{b_\Gamma}}^{\frac{b}{2}} c(y) C_{d_{W_{L_{\text{outer}}}}}(y)\, dy \tag{3.76}$$

With $C_{d_{W_{L_{\text{outer}}}}}$ defined as:

$$C_{d_{W_{L_{\text{outer}}}}}(y) = C_{d_0} + \frac{(C_{l_{W_{L_{\text{outer}}}}}(y))^2}{\pi A R e} \tag{3.77}$$

The induced drag components of these equations vary directly with $C_{l_{W_{R_{\text{outer}}}}}$ and $C_{l_{W_{L_{\text{outer}}}}}$, defined previously, for the right and left sides respectively. Summarizing the established

forces generated by the wing, the total lift generated by the system is:

$$L = L_{R_{\text{inner}}} + L_{L_{\text{inner}}} + L_{R_{\text{outer}}} + L_{L_{\text{outer}}} \tag{3.78}$$

where the lift contributions are summed from the inner and outer portions of the right and left sides of the wing. The total drag for the system is defined similarly as:

$$D = D_{W_{R_{\text{inner}}}} + D_{W_{L_{\text{inner}}}} + D_{W_{R_{\text{outer}}}} + D_{W_{L_{\text{outer}}}} \tag{3.79}$$

The lift and drag forces defined now correct for a shift in the spanwise breakpoint and are used in the equations of motion Equations (3.36) and (3.37).

With the rotation of the normal force generated by the outer wing section, a component of the normal force is projected onto the y^B axis. A differential in lift generated by the wings will result in an adverse side force, similar to the effect previously described with the ailerons in Section 3.4. Due to small angle approximations typically associated with the dihedral angle, the $\sin(\Gamma)$ term is often neglected and therefore any adverse side force is ignored; this however cannot be ignored at higher dihedral angles due to the exacerbated magnitude of $\sin(\Gamma)$. The increased side force due to this term at large dihedral angles was captured in the LPV system. Note that it is expected for breakpoints further outboard, a larger dihedral angle will be required. This likely requirement is due to the implicit reduction in lateral-directional stability and gust rejection bandwidth with outboard breakpoints. To compute the translational force encountered along the y^B axis, the previously identified normal force generated by the outboard portion of the wing can be projected onto the y^B axis using the Equation (3.9), where the final contribution by the right wing to this effect is given by:

$$Y_{W_R} = q_\infty \sin(\Gamma) \int_{y_{b_\Gamma}}^{\frac{b}{2}} c(y) C_{l_{W_R}}(y)\, dy \tag{3.80}$$

Denoting the same effect generated by the left wing:

$$Y_{W_L} = -q_\infty \sin(\Gamma) \int_{y_{b_\Gamma}}^{\frac{b}{2}} c(y) C_{l_{W_L}}(y)\, dy \tag{3.81}$$

Combining the contribution of both wings leads to the general contribution of the wing to the side force:

$$Y_W = Y_{W_L} + Y_{W_R} \tag{3.82}$$

3.8.2 Aerodynamic Moments

The change in roll moment due to p, C_{l_p}, is driven by the roll damping terms seen previously in Equations (3.64) and (3.71), in which the angles of attack drive the change in lift, creating a roll moment in both the inner and outboard portions of the wing. The roll moment generated from the inner and outer wing sections was approximated using the expanded definition in Equation (3.83).

$$L_{\text{roll}} \approx \bar{y}_{\text{outer}}(L_{L_{\text{inner}}} - L_{R_{\text{inner}}}) + \bar{y}_{\text{outer}}(L_{L_{\text{outer}}} - L_{R_{\text{outer}}}) + (\tan(\Gamma)(\bar{y}_{\text{outer}} - y_{b_\Gamma}\frac{b}{2}) + z_{cg})\Delta Y_W \tag{3.83}$$

The first term in the equation estimates the contribution of the inner wing to the roll moment. It is approximated that the acting center of lift, $\bar{y}_{\text{inner}}$, acts at $\frac{b}{2}\frac{y_{b_\Gamma}}{2}$, being the midpoint of the inner section. The second term, consisting of the spanwise center of lift on the outer portion of the wing, $\bar{y}_{\text{outer}}$, is used to estimate the point of lift for the outboard portion of the wing. The assumptions regarding the use of $\bar{y}_{\text{outer}}$ described in Section 3.8.1 are also used here for estimating the rolling moment arm. The third component attempts to capture the roll moment generated due to the side force component, where this term is prominent at higher dihedral angles and subject to the positioning of z_{cg}.

To model the new pitch moment associated with the change in breakpoint, the previous equations required minimum modification to incorporate these changes. It was previously established that:

$$C_{m_{\alpha_W}} = C_{L_{\alpha_W}}(h - h_{ac_W}) \tag{3.84}$$

Equation (3.84) provides the ability to compute the moment generated by the wing, M_W, at a given angle of attack. This term is now modeled as:

$$M_W = L(h - h_{ac_W}) \tag{3.85}$$

Where the total lift generated, L, was given in Equation (3.78). The term M_W is factored into the pitching moment, M, along with the contributing horizontal stabilizer moment.

The yaw moment created by the wing varied minimally from the previous definition. Equation (3.61) showed the differential in drag contributing to the yaw moment, with dependence on $\bar{y}$; it is now required to isolate the inner and outer portions of the wing in this equation. This formulation is given in Equation (3.86).

$$N_W = (D_{W_{R_{\text{inner}}}} - D_{W_{L_{\text{inner}}}})\bar{y}_{\text{inner}} + (D_{W_{R_{\text{outer}}}} - D_{W_{L_{\text{outer}}}})\bar{y}_{\text{outer}} \tag{3.86}$$

Again, it is acknowledged that an increased dihedral angle results in the drag force being located closer to the z^B axis, and therefore reduces the yaw moment generated through a differential in drag. The dependency of this term can be added in future work.

3.8.3 Active Dihedral Actuator

A known benefit of moving the dihedral breakpoint outboard is a direct reduction in torque required to actuate the wing, due to the reduction of wing inertia and reduction

in lift generated outboard. To estimate the moment of inertia variation of the wing as a function of the dihedral breakpoint, the wing thickness was measured at multiple points, then averaged, giving the third reference dimension required to estimate the variation of mass assuming constant density. Equation (3.87) shows how the moment of inertia of the wing was approximated.

$$I_W(y_{b_\Gamma}) = \int_{y_{b_\Gamma}}^{\frac{b}{2}} \int_{-\frac{c}{2}}^{\frac{c}{2}} \int_{-\frac{t_w}{2}}^{\frac{t_w}{2}} \rho(y - y_{b_\Gamma})^2 \, dz dx dy \tag{3.87}$$

The varying wing mass moment of inertia, as a function of the dihedral breakpoint, was incorporated into the torque equation. Equation (3.88) reflects the updated angular acceleration equation for the wing in terms of y_{b_Γ}.

$$\ddot{\Gamma}(\delta_\tau, y_{b_\Gamma}) = \frac{\delta_\tau}{I_W(y_{b_\Gamma})} \tag{3.88}$$

By selecting a larger value for y_{b_Γ}, there exists a reduction in I_W, and a corresponding linear reduction in torque required to generate a given angular acceleration.

3.9 Linear Multi-Parameter Varying System

Consider the complex set of nonlinear equations defining an aircraft's equations of motion, given in Section 3.6. These equations are commonly reduced to a set of first order linear ordinary differential equations representing perturbations from a single equilibrium point. Consider the following nonlinear model:

$$\begin{cases} \dot{x} = f(x(t), u(t), w(t)) \\ y = h(x(t), w(t)) \end{cases} \tag{3.89}$$

The state is given by $x(t)$ and the output by $y(t)$, where $u(t)$ is the system input, and $w(t)$ is any additional reference input or disturbance. There exists significant literature on the reduction of these nonlinear equations to a set of linear equations about a single equilibrium point [16]. The linear equations are given as:

$$\begin{cases} \dot{x} = A(t)x + B_w(t)w + B_u(t)u \\ y = C(t)x + D_w(t)w + D_u(t)u \end{cases} \tag{3.90}$$

Where $A(t)$, $B(t)$, $C(t)$, and $D(t)$ correspond to the Jacobian for the system of equations, evaluated at an equilibrium state (x_0), input (u_0), disturbance (w_0), and time (t); if no dependence on time, these matrices reduce to A, B, C, and D. Notionally, the $\dot{x}$ given in Equation (3.90) is $\Delta\dot{x}$, being an artifact of the Taylor series expansion, such that there exists a small difference over time between the actual and nominal values, such that higher-order terms of the expansion can be continually ignored [17]. For an active dihedral system, it is possible for Γ to deviate significantly from its nominal value, leading to a large $\Delta\Gamma$. Assuming violation of the small perturbation constraint, with $\Delta\Gamma$ being large, LTI equations become challenging to use with assurance for the active dihedral problem.

In order to accurately model a nonlinear flapping wing system, a linear parameter-varying system can be used such that a set of linear systems conform to the appropriate aircraft configuration. The use of an LPV system allows accuracy in capturing model dynamics at states deviating significantly from equilibrium, through a purely linear plant that changes with time-varying parameters, which an LTI system lacks [18].

An LPV system is consistent with that of a linear time-varying (LTV) system, such as in Equation (3.90), operating with the state, input, output, and feed-through matrices, with the state vector $x(t)$ being $n \times 1$ dimensional. The system becomes parameter-dependent

when the state, input, output, or feed-through matrices, are functions of time-varying parameters for which there is missing *a priori* knowledge of how the parameter-dependent matrices change with time. This parameter dependence may also include the feedback imparted on the system due to an unknown disturbance that varies with time [19]. The general form of an LPV system can be given as:

$$\begin{cases} \dot{x}(t) = A(\rho(t))x(t) + B_w(\rho(t))w(t) + B_u(\rho(t))u(t) \\ y(t) = C_y(\rho(t))x(t) + B_{yw}(\rho(t))w(t) + D_{yu}(\rho(t))u(t) \end{cases} \tag{3.91}$$

with the range of parameter dependencies, ρ, being:

$$\rho(t) = [\rho_1(t)...\rho_{n_\rho}(t)] \tag{3.92}$$

where ρ_{n_ρ} is the number of parameter dependencies of which all n_ρ states are available to the controller. The number of parameter dependencies, n_ρ, is not constrained to the number of system states, n, as the system may be parameter-dependent on output states or disturbances.

A common way of building the LPV system and the set of parameter-dependent matrices is using a linearization-based scheduling approach. This approach uses a finite set of pre-evaluated Jacobians in which the system has been linearized about some set of equilibriums, and assumes the dynamic system will operate within the pre-defined envelope of linearized equilibrium points through all perturbations [20]. An example of this is an aircraft flying in equilibrium conditions at a range of Mach numbers, altitude, and corresponding angles of attack. The set of linearized models can be understood as follows. Consider the set of all possible operating points, R, and assume there exists a subset of equilibrium operating

points $R^0 \subset R$, with:

$$\begin{cases} 0 = f(x_0, u_0, w_0) \\ y_0 = h(x_0, u_0) \end{cases} \tag{3.93}$$

such that $(x_0, u_0, w_0) \in R^0$ and the function $f(x, u, w)$ is continuously differentiable at all equilibrium points in R^0, then the LPV model based on a set of Jacobian linearized matrices can be defined as:

$$\begin{cases} \dot{\tilde{x}} = A(\rho)\tilde{x} + B_w(\rho)\tilde{w} + B_u(\rho)\tilde{u} \\ \tilde{y} = C(\rho)\tilde{x} + D_w(\rho)\tilde{w} + D_u(\rho)\tilde{u} \end{cases} \tag{3.94}$$

where $\tilde{x}$, $\tilde{w}$, and $\tilde{u}$ remain close enough to equilibrium such that the higher order terms of the Taylor series expansion maybe neglected (i.e. $\Delta x = x - \tilde{x}$ remains small). The term ρ is the set of varying parameterized states defined in Equation (3.92). It can also be enforced that the parameterized states are limited to the set of equilibrium values, such that $\rho \in R^0$. When a parameter dependency (i.e. ρ_m) changes in value such that the LPV system switches, the Jacobian is evaluated at the new equilibrium point. A well-designed feedback controller will alter the input to maintain the system at its new operating point, to return Δx back to zero [18]. A simple example for an aircraft is an LPV system dependent only the Mach number, ρ_m, such that the state can be represented as $A(\rho_m)$. For the aircraft to fly at a new value of ρ_m (i.e. the Mach number is increased), the system will now require a select amount of additional throttle for the aircraft to maintain the Mach number due to increased drag. The LPV example provided can be extended to n_ρ parameters.

This definition of an LPV system constructed from the equilibrium linearized points does not capture the system's dynamics in its entirety, with respect to an active dihedral system. Let $\rho = [\rho_{1_\rho}, \rho_{2_\rho}] = [\Gamma, \dot{\Gamma}]$, then based on the previous derivation for equilibriums, the set of $\rho \in R^0$ would allow ρ_{1_ρ} to be any desired equilibrium dihedral angle, but would restrict ρ_{2_ρ} such that $\dot{\Gamma} = 0$, as $\dot{\Gamma} \neq 0$ is not an equilibrium point. This implies the LPV

system captures only the effect of Γ on the system. This is visualized in Figure 3.8, where the points indicate various dihedral angle equilibrium states in R. In order to accurately model the system, additional operating points must be considered where $\dot{\Gamma} \neq 0$.

To allow for operating points where $\dot{\Gamma} \neq 0$, an extension of ρ must be made to include the varying parameter $\dot{\Gamma}$, such that $\rho \in R$. This inclusion does not change the fact that a subset of equilibrium points, ρ_0, still remains within the operating range, as $\rho_0 \subset \rho$ and $\rho_0 \in R^0$. Equation (3.94) is still valid, however, the extension of ρ must be observed, such that $\rho \in R$. The modeling method used in this study consists of constructing the system to

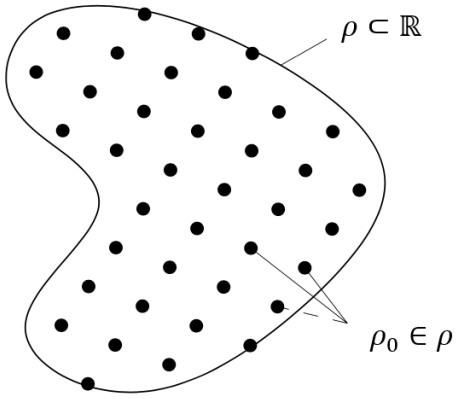

Figure 3.8: Discrete set of equilibrium operating points, ρ_0, within the operating envelope ρ [18]

a select set of operating points such that the LPV system varies this with ρ within a given envelope. The system can be constructed as

$$\begin{cases} \dot{\tilde{x}} = A(\Gamma, \dot{\Gamma})\tilde{x} + B_w(\Gamma, \dot{\Gamma})\tilde{w} + B_u(\Gamma, \dot{\Gamma})\tilde{u} \\ \tilde{y} = C\tilde{x} + D_w\tilde{w} + D_u\tilde{w} \end{cases} \tag{3.95}$$

where:

$$A(\Gamma, \dot{\Gamma}) = \left(\frac{\partial f}{\partial x}\right)\Bigg|_{\tilde{x}^*_{\text{eq}}, \Gamma, \dot{\Gamma}} \tag{3.96}$$

Note that $\tilde{x}^*_{\text{eq}}$ in Equation (3.96) represents the equilibrium states excluding Γ and $\dot{\Gamma}$. The Jacobian can be evaluated at any input values of Γ and $\dot{\Gamma}$ to obtain the corresponding dynamics for the aircraft. Consider the example of an aircraft flying with a fixed dihedral angle of Γ_0, in equilibrium conditions. This implies the previous set, ρ, is no longer varying, with the state matrix evaluated as:

$$A(\Gamma_0, 0) = \left(\frac{\partial f}{\partial x}\right)\Bigg|_{\tilde{x}^*_{\text{eq}}, \Gamma_0, 0} \tag{3.97}$$

The resulting state matrix is the traditional LTI version of the aircraft with a fixed dihedral angle. If it were desired to determine the aircraft's state while operating at the same equilibrium conditions (i.e. u_{eq}, θ_{eq}, etc.) but with a higher dihedral angle, Γ_m, and positive flapping at a rate, $\dot{\Gamma}_m$, then the following state matrix would be used:

$$A(\Gamma_m, \dot{\Gamma}_m) = \left(\frac{\partial f}{\partial x}\right)\Bigg|_{\tilde{x}^*_{\text{eq}}, \Gamma_m, \dot{\Gamma}_m} \tag{3.98}$$

The resulting state matrix gives the aircraft sinking in altitude at a rate corresponding to the increased dihedral angle, and creating associated downward forces with the flapping wings upwards. Evaluating $A(\Gamma, \dot{\Gamma})$ for a range of Γ and $\dot{\Gamma}$ generates a gridded operating region in which the local dynamics of the system can be predicted, providing improved accuracy of the nonlinear system's response for various values of Γ and $\dot{\Gamma}$. Given a finite set of discrete points, which ρ can be discretized by, an LPV switched system can be constructed. To synthesize a finite and stable LPV system, the parameters, ρ, will be constrained to a bounded operating region later defined. There arises an additional need for discussion of the stability and feedback control applied to the LPV switched system, given in Chapter 5.

3.10 Gust Disturbances

Consideration is given to both discrete and continuous gust models in aircraft design to evaluate structural performance and dynamic stability. The FAA 14 CFR Part 25.341 in combination with Advisory Circular 25.341-1 provides a set of discrete gusts and continuous turbulence requirements that aircraft and their components must be capable of handling. Both gust requirements were used for this study to evaluate the ability of the aircraft to reject wing gusts through an active dihedral system. In terms of structural performance, consideration was given to the total acceleration of the aircraft's center of mass encounters, giving a comparison of the active dihedral system relative to a standard aircraft configuration. The aircraft's wing and fuselage structure, and the associated restriction on the number of g's that can be encountered, will not be considered in determining the optimal dihedral or breakpoint configuration, nor the best active dihedral controller for the system, as this assessment falls outside the scope of this project. There is consideration of aircraft stability and gust rejection performance in this study against both gust profiles.

3.10.1 Discrete 1-Cosine Gusts

The FAA defines the use of discrete gust requirement to be constrained to a one-dimensional perturbation that acts normal to the aircraft's path of flight. The discrete gust takes the form of a 1-cosine velocity profile, such that the gust is a function of space and not of time. The velocity profile uses multiple parameters to define the gust field including, a reference gust velocity U_{ref}, a flight profile alleviation factor F_g, and a gust gradient H, driving the maximum velocity encountered by the aircraft. The reference gust velocity, U_{ref}, is an effect gust velocity that would occur once every 70,000 flight hours for aircraft, which the reference velocity is a function of altitude specified in FAA Part 25.341.1. This leads to

the Equation (3.99), giving the design gust velocity [21].

$$U_{ds} = U_{ref} F_g \frac{H}{350}^{1/6} \tag{3.99}$$

Assuming a gust gradient of 350 feet, the reference gust velocity would be the design gust velocity, the peak of the 1-cosine gust. The gust gradient itself is defined as the distance over which the 1-cosine gust will reach its peak amplitude from zero initial disturbance, where its value is specified as ranging from 30 to 350ft. This gradient drives how quickly the aircraft will accelerate, and could potentially correlate to the rate of flapping in terms of an active dihedral controller. For example, a large gust gradient would give the aircraft's active dihedral feedback controller an extended period of time to respond to the gust, requiring a significantly lower $\dot{\Gamma}$ to reject the wind gust, and the elevator may prove as a sufficient means for rejecting the gust. A small gust gradient would perturb the aircraft significantly faster than a traditional elevator controller may be capable of reacting to, whereas direct lift from active dihedral may prove beneficial. The FAA recommends a gust gradient distance be assigned to 12.5 times the mean chord of the aircraft. Knowing the general purpose of the discrete gust is to test aircraft structural and dynamic stability performance, the gust gradient may be modified as suitable for testing the active dihedral mechanism, as the active dihedral may have limitations on how steep a gust gradient may be used. The 1-cosine gust created, which is a function of the aircraft's distance traveled, S_x, is given by Equation (3.100).

$$U = \frac{U_{ds}}{2}(1 - \cos(\frac{\pi S_x}{H})) \tag{3.100}$$

For this study, to simplify computation, it is assumed that the aircraft is traversing at a fixed speed, u_∞, over the course of the simulation, leading to a 1-cosine gust velocity profile

dependent on time. This assumption will hold for all simulations even if the aircraft is perturbed more than desired in the longitudinal direction.

3.10.2 Continuous Turbulence

An additional type of gust aircraft are commonly subjected to is continuous turbulence often modeled using the von Kármán wind turbulence model. This model is typically favored in aircraft design and is used in 14 CFR Part 25.341.1 for continuous gust modeling. When evaluating aircraft response in terms of design, it is assumed in 14 CFR Part 25 that the gust velocity is acting in one dimension, that being in either the vertical or horizontal direction, holding the velocity constant in the direction normal to the aircraft's trajectory. The von Kármán model of isotropic atmospheric turbulence in the vertical and lateral direction is modeled using the following spectrum functions:

$$\Phi_{22}(\Omega_1) = \Phi_{33}(\Omega_1) = \frac{\sigma^2 L}{\pi} \frac{1 + \frac{8}{3}(1.339 L\Omega_1)^2}{[1 + (1.339 L\Omega_1)^2]^{\frac{5}{6}}} \tag{3.101}$$

Where L is the observed characteristic length scale, σ^2 is the mean-square velocity fluctuation of the turbulence, and Ω_1 is the spatial frequency [13]. These terms are selected in many cases to perturb the aircraft by specific peak frequencies, exciting the aircraft such that dynamic and structural modes can be analyzed, particularly in aeroelastic problems. At lower altitudes (i.e. 200ft) the length scale is selected using:

$$L_w = L_v = \frac{h}{2} \tag{3.102}$$

Where h is the corresponding altitude and L_w and L_v correspond to the vertical and lateral length scales respectively [22]. Due to and assumed 200ft altitude, a length scale of 100ft

was selected for the turbulence model. The frequencies of vehicle excitement were not of high interest in this current study, therefore any variation of a lower characteristic length scale would be sufficient for perturbing the vehicle. A mean-square velocity of 1 was selected for the atmospheric turbulence with intent to modify the disturbance by a scalar gain if desired to increase the magnitude of perturbation. Further explanation of the von Kármán atmospheric turbulence model and associated input parameters are described by Etkin and in 14 CFR Part 25 [1].

Chapter 4

Methods of Analysis

4.1 Aircraft Configuration Selection

A baseline aircraft was selected from the Nonlinear Systems Laboratory (NSL) at Virginia Tech for a theoretical performance assessment of an implemented active dihedral system. The My Twin Dream (MTD), shown in Figure 4.1, was selected at the beginning of this study based on platform usage throughout the NSL for a variety of flight dynamics and control research projects. The methods used for analysis of the theoretical active dihedral system is translatable across platform, and hence the general modeling equations given in Chapter 3.

Figure 4.1: My Twin Dream fixed-wing experimental aircraft used at the Nonlinear Sytems Laboratory (NSL) at Virginia Tech [23]

The mass, inertia, and geometric properties of the MTD were required to define and develop the theoretical model describing the effect of active dihedral. In a study conducted by Gresham et al. [23], a complete flight dynamic model was identified for the MTD. The mass and inertia properties for the testbed are provided, along with basic wing geometry parameters in Table 4.1 as identified experimentally by Gresham et al. [23].

Property	Symbol	Value	Unit
Mass	m	0.195	slug
Mean Aerodynamic Chord	$\bar{c}$	0.833	ft
Projected Wing Span	b	5.91	ft
Projected Wing Area	S	4.92	ft^2
Roll Moment of Inertia	I_{xx}	0.178	slug-ft^2
Pitch Moment of Inertia	I_{yy}	0.152	slug-ft^2
Yaw Moment of Inertia	I_{zz}	0.297	slug-ft^2
Products of Inertia	I_{xy},I_{yz},I_{xz}	0	slug-ft^2

Table 4.1: My Twin Dream (MTD) mass and geometric properties [23]

Additional geometric measurements were taken of the aircraft and are provided in Appendix B. Note the importance of understanding the wing properties due to change in moment of inertia with a variation of the dihedral breakpoint, and the direct sensitivity of torque requirements, described in Section 3.8.3,

The following additional assumptions were made based on flight test data from Gresham et al. [23] and the estimated aircraft shape. The MTD operates at a cruise speed of approximately 65 $\frac{\text{ft}}{\text{s}}$. The MTD's variable chord was estimated for the wing due to the increased sensitivity of a flapping wing system to the wing area. The vertical and horizontal stabilizers were approximated by rectangular surfaces using their respective spans, b_{vt} and

b_{ht}, paired with their mean aerodynamic chord, $\bar{c}_{vt}$ and $\bar{c}_{ht}$ respectively. It was assumed the contribution of the tail to C_{l_β} would remain fixed. The airfoil used for modeling the wing is the Clark-Y, characterized by the cross-section's flat lower camber typically associated with the airfoil. The vertical and horizontal stabilizers, each having symmetric airfoils, were assumed to be NACA0012 airfoils, with the horizontal stabilizer having zero incidence angle, but trimmed in flight.

The fuselage and its associated drag are estimated using numerical tools, but its effect on the system is only allocated to drag, increasing thrust requirements. It was acknowledged that the fuselage directly impacts C_{l_β}, which is exacerbated with high wing configurations, but is ignored in this study. It was assumed the 0° dihedral wing persists as an accurate model for spanwise lift distribution for all configurations and can be used for higher dihedral angles to compute C_{l_β}. This assumption was later proven valid through numerical estimation of the spanwise lift distributions.

4.2 Numerical Estimation of Aircraft Aerodynamic and Stability Parameters

In order to estimate the aerodynamic force and moment coefficients required as input to the active dihedral MATLAB model, XFLR5 [24] was used to estimate the aerodynamic coefficients for the predefined static wing and tail configurations. It was also possible with XFLR5 to estimate dynamic stability performance parameters with the input of aircraft inertia values, giving a baseline estimate for the MTD dynamic modal responses. XFLR5 uses the Vortex Lattice Method (VLM), an extension of the Prandtl lifting-line theory, to numerically estimate the performance of wing bodies, using a lattice of horseshoe or ring

vortices to identify the lift and drag characteristics for the surfaces [25]. The lattice is comprised of a user-specified number of panels, in which the thickness of airfoils and wings are neglected, with the mean camber line being used to represent the thin wing. Pertaining to fixed dihedral systems, XFLR5 excels in estimating the static equilibrium performance with viscous effects, given *a priori* knowledge of the vehicle configuration; additional means of simulation and estimation are required to compute the effect of flapping wings [24]. A depiction of the static configuration, with the breakpoint at 50% span and dihedral angle of 15°, is shown in Figure 4.2.

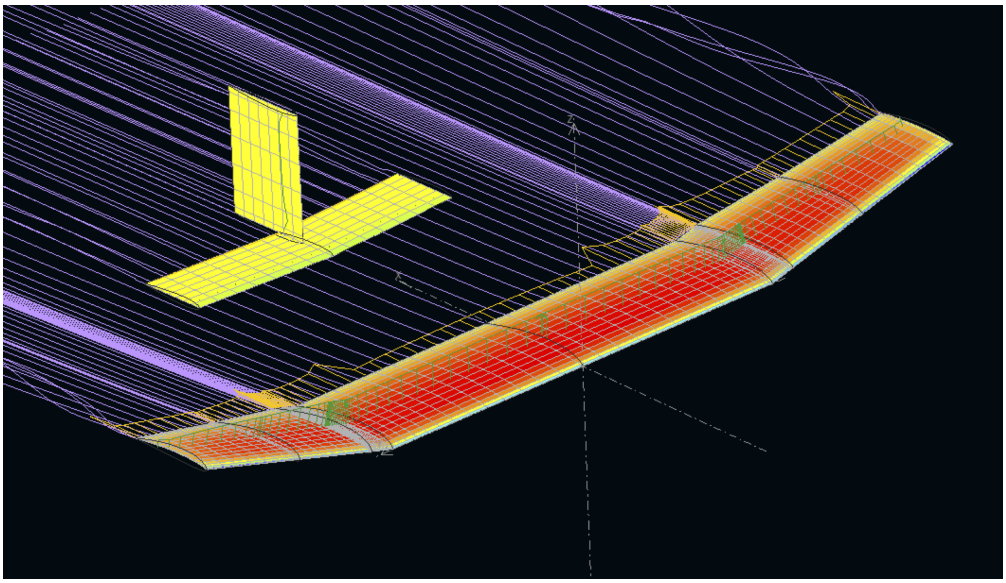

Figure 4.2: XFLR5 model of the static dihedral configuration with $y_{b_\Gamma} = 50\%$ and $\Gamma = 15°$

To characterize the modeled aircraft's aerodynamic performance, XFLR5 first requires the geometric inputs including the span, chord, and airfoil, for the wing, vertical stabilizer, and horizontal stabilizer. Center of gravity and moments of inertia are also required for properly estimating static and dynamic stability. The geometric inputs provided in Appendix B are used for modeling the vehicle; these geometric parameters are similarly used in the MATLAB model. The complexity of a spanwise variation in the chord is accounted for in

both VLM and MATLAB models, as accuracy in wing inertia modeling is required for a varied breakpoint implementation of active dihedral. The fuselage is not modeled in XFLR5 based on the software's recommendation, due to the inability to resolve overlap between panels that are in union [24]. The estimated cruise speed of $65\frac{\text{ft}}{\text{s}}$ for zero dihedral angle obtained through flight test data could be validated using XFLR5 with its fixed lift capability paired with previously defined mass properties. The Clark Y and NACA0012 were initially evaluated at a variety of Reynolds numbers, bounding the operational Reynolds number. This was completed to allow XFLR5 to interpolate between Reynolds numbers, as the airfoils were subjected to variation of chord with wing taper, and inherently increasing freestream velocity with increased dihedral angle.

Dynamic performance and stability derivatives were obtained through a separate stability analysis in XFLR5, using defined values of inertia, mass, and center of gravity location. It is assumed that in all static configurations, the inertia is fixed; this assumption may be crude as the vehicle's inertia is changing when the static wing configuration is varied in breakpoint and dihedral angle. Additional experimental or theoretical measures would be required for estimating the variation in the static configuration inertias with increased dihedral angle. Defining a dynamic stability analysis in XFLR5 and executing the analysis for all configurations leads to computation of the stability derivatives and dynamic modal responses, which are primarily used as a check and balance with the MATLAB-defined model. The stability derivatives, specifically C_{l_β}, were used to indicate similarity between the VLM and MATLAB models, showing the MATLAB active dihedral system properly models the characteristics of the static dihedral configurations.

4.3 Cost Analysis

The need to assess incurred costs to implement a flapping wing system was identified by the author. From previous research completed by Fisher et al. [26], it is known that implementing an active dihedral system that actuates at the wing root significantly increases the required torque to actuate the wing, leading to additional actuator weight, and increased weight for maintaining structural integrity. This type of cost incurred is seen today on the Boeing 777 configuration, in which the wingtips fold inward to maintain airport compatibility; the factors driving the design of this system relate to structural and mechanism actuation limitations of the vehicle [27]. To this end, there persists a need to find the best breakpoint to implement the active dihedral system on an aircraft.

There exist additional factors which are not considered here, but should be considered in a true trade study for the implementation of an active dihedral control system. The mission at hand should be evaluated for the usefulness of active dihedral, as an active dihedral system changes the total acceleration observed by on-board instrumentation, potentially alleviating or exacerbating forces to the system that disturbances bring. Aircraft field of view (FOV) may also be considered in an attempt to keep the aircraft constrained to a trajectory or desired attitude for the purposes of a mission. Structural requirements should also be evaluated as the wing loading induced by an active dihedral system is greater than that which is experienced in normal flight operations, with the flapping motion creating additional root bending moment and spanwise variation in the lift. Aero-elastic effects may also be considered with the flapping wing motion, but this study assumes a rigid wing structure that does not deflect with increased wing loading. The additional system and design level requirements provide here should be evaluated in a robust trade study with the intent of implementing this on an air vehicle.

4.3.1 Actuation and Torque Requirements

Applied torque was identified as one of the physically demanding requirements that must be met with minimal margin for error with respect to aircraft design and analysis; improper evaluation can lead to the wings collapsing inward. The torque required for the aircraft to operate must bear the loading scheme of the wing for the entirety of the flight while having sufficient torque to actuate the wings mid-flight at a rapid enough rate to reject wind gusts. Consideration must also be given to providing the aircraft with the ability to maintain an off-equilibrium fixed dihedral angle for a persisting time period to meet additional lateral-directional dynamic stability requirements that may be desired at higher angles of attack in turbulent conditions.

Torque is often supplied directly through a servo or similar actuating mechanism, with the wing directly transferring its load into the servo. Methods including gearing, transfer rods, or pulley systems can be used to obtain a mechanical advantage for the servo, with the loading capability scaling directly with the associated mechanical advantage [7]. Work previously completed by Fisher et al. [26] demonstrated the concept of a geared flapping-wing aircraft which successfully actuated from 0° to 30°. For the aircraft considered in that study, it was shown that a 7:1 gearing ratio provided sufficient torque to maintain loading under nominal flight conditions, plus a factor of safety, using a set of two servos. The actuators used for flight were high throughput servos, 2.89lb-ft stall torque, limited to 270° actuation. The 7:1 gearing ratio limited the range of motion to 30° but increased the effective servo stall torque to 20.15lb-ft, meeting the torque requirement for the testbed used. This previously designed system proved functional, but limitations were imposed on Γ and $\dot{\Gamma}$ for the system. It was found that the servo actuation rate was $333\frac{^\circ}{\text{sec}}$ before gearing, and hence limited the wings effective actuation rate to $47.6\frac{^\circ}{\text{sec}}$.

For the study at hand, the total actuator torque throughput is limited to ±20lb-ft, which was the equivalent feasible torque throughput previously demonstrated by Fisher et al. [26]. The maximum stall torque required for maintaining a single MTD wing at a constant dihedral angle was 4.63lb-ft based on the lift distribution and geometric profile of the aircraft. The stall torque requirement varies with change in breakpoint, being directly correlated to the spanwise lift distribution curve. The bounds of $\dot{\Gamma}$ were established as $90\frac{^\circ}{\text{sec}}$ with the notion that the system previously designed could be improved through additional mechanical advantage, providing increased torque and actuation rate. The assumption used for this study implies twice the previously demonstrated actuation rate, which in the author's opinion, was a feasible constraint to overcome through additional mechanical means beyond the scope of this paper.

Equations (3.33) and (3.88) were implemented in the simulation, with MATLAB enforcing the torque throughput and flapping rate constraint. The aerodynamic forces acting on the wing were not modeled in the torque equations, leaving the wing forces and the effect of stall torque disassociated with the controller. For example, it requires significantly more torque to actuate the wing downward due to the forces acting on the wing; this is not modeled. It is acknowledged that this is a shortcoming in the actuation equations of motion and a higher level simplification, however, the stall torque requirement was factored into the cost evaluation during post-processing, enforcing the true torque requirements in cost assessment. The post-processing assumptions associated with the current draw were as follows. The assumed current draw for the actuating system operating at the stall torque is $3A$ [26]. The torque required to actuate the wings at a positive $\dot{\Gamma}$ is marginal due to the lift generated by the wings having the tendency to rotate the wings in the positive Γ direction. The only torque required is to actuate the system's wing moment of inertia, as defined in Equations (3.33) and (3.88). It was also assumed that in addition to the nominal

torque required to actuate the wing under no loading, the stall torque was also invoked when actuating the wing downwards to counteract the lift force of the wing. The torque required was scaled based on lift distribution, such that breakpoints further outboard would have a reduced stall torque. To estimate torque variation with shift in breakpoint, it is assumed that variation in torque draws the linearly proportional amount of current, acknowledging the fact that this may no longer be the true stall torque of the actuator. For example, if a breakpoint location of 75% was used, and the outboard portion of the wing generates only a quarter of the lift, then a quarter of the stall torque is used to penalize the system. Incorporating constraints on the system limiting the minimum and maximum dihedral did not prevent the controller from attempting to actuate past these points through the application of additional torque, hence, post-processing used logic to ensure the elimination of any applied torque when the dihedral angle was at its upper or lower bound of 0° or 60° respectively.

Consideration was also given to the battery architecture of the active dihedral system, with the actuating system notionally being designed in series with the flight battery. The work previously completed by Fisher et al. [26] placed the active dihedral system in parallel to the traditional propulsion system battery, preventing consumption of the allocated active dihedral battery capacity, causing the wings to fold inward and a failure of the system [26]. Means of mitigating this type of failures, such as a clutch or rack and pinion, would allow the system to operate on batteries in series, reducing the overall system weight and complexity. The method of fixing the wing in a desired position when not rejecting a gust, alleviating the actuation system of required torque, was assumed when $\dot{\Gamma} = 0\frac{^\circ}{\text{sec}}$.

4.3.2 Perturbation from Trajectory

To evaluate gust rejection performance of the system and associated feedback controller for a given disturbance, it was required to define a cost to penalize the system. The LQR state cost, Q, was used as a means of evaluating cost between the elevator and active dihedral controllers, as they maintained a fixed Q across control systems. The simulation is resolved with a large set of finite points through MATLAB using an ODE solver, and a cost evaluated based on a uniformly discretized solution was developed using Equation (4.1) [28].

$$J = \frac{h}{2}\sum_{k=0}^{N-1}(x(kh)^T Q x(kh) + u(kh)^T R u(kh)) \tag{4.1}$$

The equally spaced N samples were separated by small step sizes of h. The penalty associated with controller input, given via R, varied between the elevator only and active dihedral controllers and therefore was not included in the penalty. Only the cost associated with Q was evaluated to indicate controller performance relative to state deviation. The cost evaluation takes the form of Equation (4.2). The cost for this system was derived from the discrete LQR cost formulation, and was implemented to simplify system performance evaluation with respect to the MATLAB ODE solver.

$$J_Q = \frac{h}{2}\sum_{k=0}^{N-1}(x(kh)^T Q x(kh)) \tag{4.2}$$

4.3.3 Dynamic Stability Performance Requirements

It was desired that the active dihedral aircraft meet the dynamic stability performance requirements outlined by MIL-F-8785C. To be fully compliant with the MIL-F-8785C standard, each aircraft configuration is to be evaluated against the minimum requirements

and must maintain these performance requirements throughout the flight. A hand-launched UAS, with active dihedral implemented, is considered to be a medium weight and medium-maneuverability aircraft falling under Class 2, using Category B as the requirement driver to ensure the experimental aircraft can complete its mission, with the handling qualities ideally being improved with active dihedral [29]. These definitions and classifications will drive the minimum requirements for the active dihedral aircraft in its mission phase of flight. It is desired that the Level 2 performance requirements be met and maintained throughout the mission phase for a given static configuration. Holding to this standard, the aircraft must handle adequately for the mission phase of flight with minimal pilot input or controller feedback; this was held true for the dynamics modes associated with static equilibrium aircraft configuration, while not necessarily held during the actuation of the active dihedral system. Table 4.2 outlines the minimum performance requirements for the system to meet Level 2 flying qualities.

Property	Value	Unit
Maximum Roll Mode Time Constant	1.4	seconds
Minimum Dutch Roll Damping	0.02	-
Minimum Dutch Roll Frequency	0.4	rad/sec
Minimum Time to Double Amplitude Spiral Mode	8	seconds
Minimum Phugoid Damping Ratio	0	-
Minimum Short-Period Damping Ratio	0.25	-

Table 4.2: MIL-F-8785C Level 2 worst-case dynamic stability performance requirements [29]

Chapter 5

Methods of Stability and Control Design

5.1 Lyapunov Stability Assessment

Lyapunov theory is commonly used for the stability assessment of linear and nonlinear systems. Using Lyapunov's direct method, it is possible to assess the set of differential equations for asymptotic stability and global asymptotic stability. Lyapunov theory is helpful for the evaluation of switched systems. Consider a system whose dynamics can be modeled by $\frac{dx}{dt} = f(x(t))$, where $f(0) = 0$ is an equilibrium point, and $x(t) \in R^n$ with n number of states. If there exists a positive definite function, $V(x)$, such that its derivative, $\dot{V}(x) = \frac{d}{dt}V(x(t))$, is continuously differentiable and satisfies $\dot{V}(x) < 0$, then the system is asymptotically stable about the equilibrium [30]. If the Lyapunov function is radially unbounded, such that $V(x) \longrightarrow \infty$ as $|x| \longrightarrow \infty$, then the system is globally asymptotically stable. Given the quadratic Lyapunov function:

$$V(x) = x^T P x \tag{5.1}$$

there must exist a matrix P, which is unknown, that is positive definite to ensure $V(x) > 0$. It then may be proven that for a first-order differential equation of the form, $\frac{dx}{dt} = Ax$, where

$A \in R^{n \times n}$, that the Lyapunov function derivative is:

$$\dot{V}(x) = (Ax)^T Px + x^T P(Ax) = -x^T Qx \tag{5.2}$$

The Lyapunov equation corresponding to this first-order system is given by:

$$A^T P + PA + Q = 0 \tag{5.3}$$

Where Q is a symmetric matrix. To solve for P in Equation (5.3), it must be enforced that $Q > 0$, such that the system can be proven asymptotically stable [31]. Due to this constraint, Q is commonly represented by the identity matrix. If the matrix P exists as a solution to Equation (5.3), reinforcing that P must be positive definite, symmetric, and unique, then the system is asymptotically stable as the Lyapunov function given in Equation (5.1) is fulfilled [30].

Using a fixed state matrix to represent the dynamics of some nonlinear systems can be restrictive and may lead to inaccurate model representation, requiring a parameter-varying state matrix to be used. Further extensions of the Lyapunov stability criterion must be used to assess a switched system and parameter-varying models and their associated stability. Take for example the LPV system in Equation (3.94), whose state matrix is $A(\rho)$, seen in Equation (5.4).

$$A(\rho)'P + PA(\rho) < 0 \tag{5.4}$$

In this case, P must exist and this is just sufficient for asymptotic stability. In fact, it may be very challenging to find a single P that satisfies Equation (5.4) depending on the complexity and order of $A(\rho)$. Equation (5.4) attempts to resolve stability about all values of ρ, however, it is often better to bound ρ to increase conservativeness in stability robustness. Consider the operating points to be restricted to a distinct and finite set, $\rho_{n_{\rho_m}}$, where there

are n_ρ parameter dependencies, and each dependency is constrained to operating at 1 of m number of discretized points at any given time. Assuming $\rho_{n_{\rho_m}}$ is defined, and there exists a P solving Equation (5.4), then the system is exponentially stable for all operating points [32]. Equation (5.5) shows the LMI which restricts the operating points.

$$A^T_{\rho_{n_{\rho_m}}} P_m + P_m A_{\rho_{n_{\rho_m}}} \leq -Q_\rho \tag{5.5}$$

$$V(x) = x^T P_m x \tag{5.6}$$

Restricting the operating region to $\rho_{n_{\rho_m}} \in \rho$, creating a switched system, assuming there exists a finite set of commuting Hurwitz matrices, A_p, then the switched linear system is globally uniform exponential stability (GUES) [33]. Note again that Q is commonly selected as the identity matrix in this case. Correspondingly, if there exists a single P_m that solves the linear matrix inequality (LMI) for all A_ρ, leading to a solution to the Lyapunov function, given in Equation (5.6), exponential stability is obtained. This theorem was used to identify a bounding set of $\rho_{n_{\rho_m}}$ for each active dihedral configuration, in which P_m was generated that solved the LMI in Equation (5.4). To ensure exponential stability, the system must be restricted to the operating points.

To allow for additional operating states between the previously defined switched system, which was constrained to the set of $\rho_{n_{\rho_m}} \in \rho$, additional analysis must be completed to ensure exponential stability. It is possible to define a set of homogeneous polynomial parameter-dependent Lyapunov functions for the system, which resolve the LMIs at all ρ, establishing a sense of exponential stability. As the degree of the polynomial increases and the number of LMIs increase, there is a reduction in conservativeness in a stability assessment [34]. A realized set of homogeneous polynomials may also be challenging to identify.

$$A^T(\rho)P(\rho) + P(\rho)A(\rho) \pm \frac{dP}{d\rho}\nu < 0 \tag{5.7}$$

where:

$$\frac{d\rho}{dt} \leq \nu \tag{5.8}$$

The parameter ν is used to incorporate the variation rate of change of ρ [35]. If bounds do not exist on ν, then there is a notion of asymptotic stability for the system. It is however challenging to test all ν and therefore, Wu shows that a discretized set of ν can be tested to show the system is parametrically-dependent asymptotically stable, for a finite set of ν [36].

Frozen-time theory is often considered to establish stability conditions for linear time-varying systems, where the time-varying component is introduced directly through parameter variation, whose rate of change is sufficiently small. The stability of the LTV system assessed via frozen-time theory can ensure stability for the system assuming the corresponding variation of $A(\rho(t))$ is sufficiently slow, where robustness is increased through the reduced variation in $A(\rho(t))$. Using this assumption, it has been proven that the LTV system inherits the worst-case stability robustness of the frozen-time LTI system for $A(\rho(\tau))$, where τ here corresponds to an instance in time [37]. Therefore, if at a given point in time, τ, all eigenvalues of the system lie within the left half-plane, it is known that the system inherits those stability conditions, irrelevant of $\dot{\rho}(t)$. The LPV system's inheritance of the frozen-time LTI system's stability robustness can be evaluated experimentally through simulations, observing the effects of an excess rate change on the system's stability, and limiting the controller's rate of change authority on the state $A(\rho(t))$ [38].

In terms of the active dihedral state dependency, the state matrix is dependent on Γ and $\dot{\Gamma}$ (e.g. $A(\Gamma, \dot{\Gamma})$), such that one would require restriction to the rate of change of Γ and $\dot{\Gamma}$. Due to the increased complexity of having two varying parameters, Γ and $\dot{\Gamma}$, dependent

on each other, this would likely lead to establishing overarching restrictions of $\frac{d\dot{\Gamma}}{dt}$, which translates directly to the torque input in Equations (3.33) and (3.88). It is acknowledged in this study that additional investigation should be conducted in the future in regards to the rate limitation of Γ and $\dot{\Gamma}$, and the implications of the two being dependent on each other. Frozen-time theory was first used as a baseline for defining available operating points, and Lyapunov stability is used to ensure asymptotic stability at a further refined set of points. While a rate limit on $\ddot{\Gamma}$ is not found in this study, the topic was discussed for purpose of author acknowledgment of rate-limited switched systems, bringing to the reader's attention that such constraints may exist.

5.2 Controller Design

The design of a feedback controller for the active dihedral system was required to actuate the system and reject wind gust disturbances. Defining an objective is necessary when building the feedback controller in order to establish the necessary gains to meet performance requirements. Feedback control laws for the active dihedral system discussed here are LQR-based, with gain scheduling being implemented due to its application to the LPV system.

5.2.1 Linear Quadratic Regulator (LQR)

LQR controllers are used for providing the optimal feedback control law for a given continuous-time linear system. The goal of LQR controllers is to reduce the quadratic cost function, which is constructed with *a priori* knowledge of the desired system response. The

quadratic cost function in typical form is provided in Equation (5.9) [39].

$$J(x) = \int_0^\infty (x(t)^T Q x(t) + u(t)^T R u(t))\, dt \tag{5.9}$$

The feedback control law solving the LQR problem, $u = -Kx$, for which the gain matrix K is the optimum gain for the system, can be solved using:

$$K = R^{-1} B^T P^* \tag{5.10}$$

Where the algebraic Riccati equation (ARE), given in Equation (5.11), can be solved to obtain the unique, positive semi-definite solution, $P*$.

$$A^T P + PA - PBR^-1B^T P + Q = 0 \tag{5.11}$$

The Q and R matrices correspond to the state and input control penalty matrices, where a large penalty associated with a state or input will attempt to mitigate its deviation from equilibrium. For the LQR controller to exist, Q and R must be positive semidefinite and positive definite, respectively, and (A, B) must be stabilizable. The LQR controller provides a simple means of feedback control for the system given a set of gust rejection goals. The optimal feedback control law can first be obtained for a static aircraft configuration, using the traditional control surfaces only to reject a wind gust. It was also possible to design a second control law allowing the use of actuator torque, δ_τ, such that the wings may actuate to reject the gust in parallel with the traditional control surfaces. These two controllers can be modified to obtain the best gust rejection performance for a given disturbance.

5.2.2 Classical Gain Scheduling

Gain scheduling is a common approach to controller design for nonlinear problems which has proven successful in industry and academia. Many approaches exist to gain scheduled controller development, some of which are discussed here, however, often the scheduling approach is designed to the control problem at hand. The concept behind gain scheduling is for the controller to modify its gain parameters based on scheduled operating point, bounded by the expected operating region for the system. The operation region of the controller is resolved via a finite set of local linear controllers about a set of equilibrium points, ideally providing an improved control law for the nonlinear system in the defined regime. Classical gain scheduling is based on identifying a finite set of equilibrium points to linearize the system, via Jacobian linearization, to build a mapping of operation points for the system and the controller to operate. The dimension of the gain scheduling controller is restricted to n number of parameters, limited by the number of observable states. An example of this, expanding upon the previous discussion of LPV systems, is an aircraft flying at various altitudes, Mach numbers, and angles of attack, which can be expressed as ρ. The aircraft's nonlinear dynamics would be linearized at the various equilibrium points and a controller would be designed for each equilibrium point. The steps required for designing a classical gain scheduling controller have been described in detail by Leith, Leithead, and Bruzelius, and the steps listed have been adapted as follows [38][40]:

1. Parameterize the equilibrium operating points, using n number of variables (Mach, altitude, angle of attack), which may be dependent on the controller input, output, states, or disturbance field. The dihedral angle was selected as the single scheduling parameter in this study.

2. Assuming the plant's dynamics can be captured at the various equilibrium operating points (x_0, u_0, y_0) which are denoted as ρ_0, then the linearized system can be given as:

$$\begin{cases} \dot{\tilde{x}} = A(\rho_0)\tilde{x} + B_w(\rho_0)\tilde{w} + B_u(\rho_0)\tilde{u} \\ \tilde{y} = C(\rho_0)\tilde{x} + D_w(\rho_0)\tilde{w} + D_u(\rho_0)\tilde{u} \end{cases} \tag{5.12}$$

The plant dynamics for the active dihedral system are resolved about various equilibrium dihedral angle operating points. An example of two equilibriums would be a low dihedral angle, low freestream velocity, with a specified elevator trim angle, and a higher dihedral, higher freestream speed, and a different elevator trim angle.

3. There then exists a desired controller to provide feedback to the system:

$$\begin{cases} \delta u = F(\rho_0)\tilde{y} + G(\rho_0)\tilde{w} \end{cases} \tag{5.13}$$

The feedback controller can be scheduled based on the observed system outputs and any additional observable disturbances. This step can use a variety of controller types including but not limited to, LQR, linear quadratic Gaussian (LQG), or H_∞ controllers. This study employs the LQR controller at each equilibrium point.

4. Steps 2 and 3 should be repeated m times to map the equilibrium points in the set of ρ_0, such that the family of controllers in use can be scheduled by the operating points ρ_m.

5. The nonlinear system must then be modeled in a manner that incorporates the designed controller. It is noted that proper modeling of the nonlinear system itself is paramount to a gain scheduled controller, as modeling will also drive the closed-loop performance of the

system, with the potential to limit the controller's operation capability [38]. This is another contributing factor to the use of an LPV system for properly modeling a variable dihedral aircraft. For example, if the active dihedral system assumed an LTI form for plant dynamics, the gain schedule may be insufficient for controlling the system due to deviation in the LTI's characteristic responses to inputs.

For the purpose of this study, ρ for the gain schedule is limited to the dihedral angle only, meaning a one-dimensional gain schedule can be created as $n = 1$. The classical gain scheduled controller for the active dihedral system is created using a finite set of linearly discretized equidistant dihedral values, denoting the equilibrium operating points $\rho_m \in \rho_0$. The equilibrium system is identified for each dihedral angle, with the associated throttle, airspeed, and elevator trim angle required being varied with each configuration. The corresponding LQR controller was found for each operating point in the finite set ρ_m, creating a set of optimal controllers for the system based on fixed state and input matrix penalties, Q and R, respectively.

An artifact of switching gains between equilibrium points can be chattering in feedback from the controller, similar to the characteristic observed in switching systems [33]. Two possible solutions exist to mitigate this phenomenon: increase the number of spatially discretized points in the gain scheduled or linearly interpolate between gain scheduled operating points. Increasing the spatial resolution in the gain schedule is the ideal solution due to the ability to model the feedback gains required for an increased number of equilibriums of the nonlinear system. This can become computationally heavy and is at some level unnecessary, as the system dynamics between two equilibrium points become sufficiently close when the LPV spatial resolution is highly discretized. Linear interpolation between gain scheduled points helps eliminate the chattering response incurred from switching sharply between gains, providing a smooth transition between operating points. The linear interpo-

lation method can be problematic with highly nonlinear systems, as a course gain schedule may be unable to control the system under sharp nonlinearities. To take advantage of both approaches, the gain scheduled controller for this study is developed using a spatial resolution in Γ of 2.5° between gain scheduled operating points, noting that a change in 2.5° between systems should allow for sufficient interpolation between points, accounting for the primary nonlinearity that comes from the dihedral angle.

5.2.3 Mixed Gain Schedule Controller

While designing a controller for the active dihedral system, a need for a modified gain scheduled controller was identified. While using a classical gain scheduled controller is appropriate for aircraft flying at multiple equilibrium points, the active dihedral system is designed to return to its nominal configuration upon completion of gust rejection; classical gain scheduling allows for the system to settle at a new equilibrium point as an optimal controller is being implemented at the new state.

The LQR weights in the classical gain scheduled controller are designed to significantly penalize deviation from the commanded trajectory, applying minimal cost deviation in equilibrium dihedral angle; a small cost was imposed with change in dihedral angle to prevent the controller from settling to non-equilibrium dihedral angles and enforcing the system return to the desired equilibrium dihedral angle. Consider the instance where weights corresponding to error from the commanded trajectory far outweigh the cost of not returning to the original dihedral angle. This case allows the system to settle in a configuration prioritizing those trajectory weights, neglecting roll stability requirements established at the equilibrium dihedral angle; this is an unexpected artifact of classical gain scheduling.

To obtain an improved controller for the system, a modified gain scheduled controller was created to leverage the robustness of a classical gain schedule controller with the authority of a heavily weighted LQR controller near equilibrium. This modified controller is a suitable fit as the classical gain scheduling provides robustness extending to a variety of large disturbances and dihedral angles, and fixed LQR controller provides the optimal controller to the system for small perturbations, returning the vehicle to the desired trajectory. The feedback controller given in Equation (5.13) is a function of the observed state and the observed disturbance; a similar feedback control function is defined in Equation (5.14).

$$K = \begin{cases} (1 - \frac{|\vec{w}|}{|\vec{w}|_{\max}})K_{\text{LQR}} + \frac{|\vec{w}|}{|\vec{w}|_{\max}}K(\Gamma), & \text{if } |\vec{w}| < |\vec{w}|_{\max} \\ K(\Gamma), & \text{if } |\vec{w}| > |\vec{w}|_{\max} \end{cases} \tag{5.14}$$

The wind disturbance observed by the vehicle, $\vec{w}$, was used with Γ to schedule the controller using a combination of the LQR gain, K_{LQR}, and the classical gain scheduled controller gain, $K(\Gamma)$. The disturbance threshold, $|\vec{w}|_{\max}$, defines a point at which the disturbance is small enough for the optimal LQR controller to maintain authority. This controller meshes gains from alternative control strategies, providing robustness through the ability to return the vehicle back to its equilibrium operating point. Implementation of this mixed gain scheduled controller helped meet lateral-directional stability criterion while maintaining gust rejection capability and eliminating undesirable effects of a discrete gain switching controller.

Chapter 6

Results and Discussion

6.1 Aircraft Aerodynamic Modeling

The wings level zero dihedral MTD aircraft was created in XFLR5 to characterize the required aerodynamic force and moment parameters for the active dihedral model previously defined. The outputs obtained were used directly in the MATLAB implementation of the active dihedral system. While attempting to verify the cruise speed using the constant lift functionality in XFLR5, the zero dihedral angle cruise speed for the model was found to be $67.8\frac{\text{ft}}{\text{s}}$, comparable to predictions by Gresham et al. [23]. Knowing that increased dihedral angles would further require increased airspeed, the analysis was conducted at a constant speed of $70\frac{\text{ft}}{\text{s}}$ with the horizontal stabilizer trimmed such that the required angle of attack was $0°$ to maintain steady level flight. The values used from XFLR5 for modeling aerodynamic properties of the wing, horizontal stabilizer, and vertical stabilizer in the MATLAB active dihedral model are defined in Table 6.1.

As previously discussed in Section 3.5, it was crucial to identify the spanwise force distribution, which was approximated through the VLM model generated in XFLR5. Figure 6.1 gives the spanwise variation for the coefficient of lift at dihedral angles of $0°$ and $30°$, with the breakpoint being located at the root. The lift distribution varied marginally between configurations, with $\Gamma = 30°$ having the greatest lift distribution. The lift curves presented show the normal force generated by the wing, not the projected component along

Symbol	Value
C_{L_α}	4.607
$C_{L_{\alpha=0}}$	0.51
C_{d_0}	0.02
e	0.836
C_{M_0}	0.020
$C_{L_{\alpha_{ht}}}$	1.853
$C_{d_{0_{ht}}}$	0.01
$C_{L_{\alpha_{vt}}}$	1.853
$C_{d_{0_{vt}}}$	0.01

Table 6.1: MTD wing, horizontal stabilizer, and vertical stabilizer aerodynamic coefficients determined using VLM with XFLR5

the z^B axis, as notionally a dihedral angle of 30° does not generate more vertical lift than the dihedral angle of 0°, all else being held constant. Generic aircraft equations of motion factor in the loss of lift due to dihedral through the projected area, S, which scales with $\cos\Gamma$. This study assumed the 0° dihedral wing acts as a sufficient baseline model for the spanwise lift distribution of all configurations, using Figure 6.1 to validate this assumption.

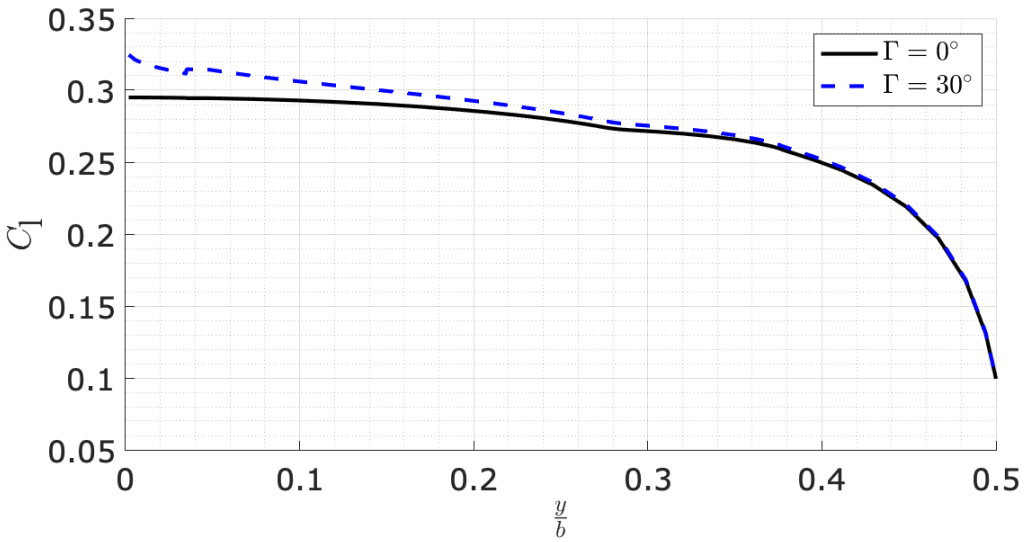

Figure 6.1: Spanwise variation of C_l for $\Gamma = 0°$ and $\Gamma = 30°$, noting C_l in this VLM analysis is indicative of wing normal force

To reduce error in the acting center of lift for the outer wing section, $\bar{y}_{\text{outer}}$, depicted in Figure 3.5, the center of lift was estimated using the $\Gamma = 0°$ lift distribution in Figure 6.1. The change in acting spanwise center of lift was plotted in Figure 6.2, indicating how $\bar{y}_{\text{outer}}$ moves with change in y_{b_Γ}. The VLM estimate was implemented in the model, giving the correct value of $\bar{y}_{\text{outer}}$ for configurations with different y_{b_Γ}. Notice that the mid-point approximation, with lift acting at the center of the section, was a close approximation to the VLM estimate. The mid-point approximation of the lift vector may have been sufficient, however, this approximation was only used for the inner wing section to determine $\bar{y}_{\text{inner}}$.

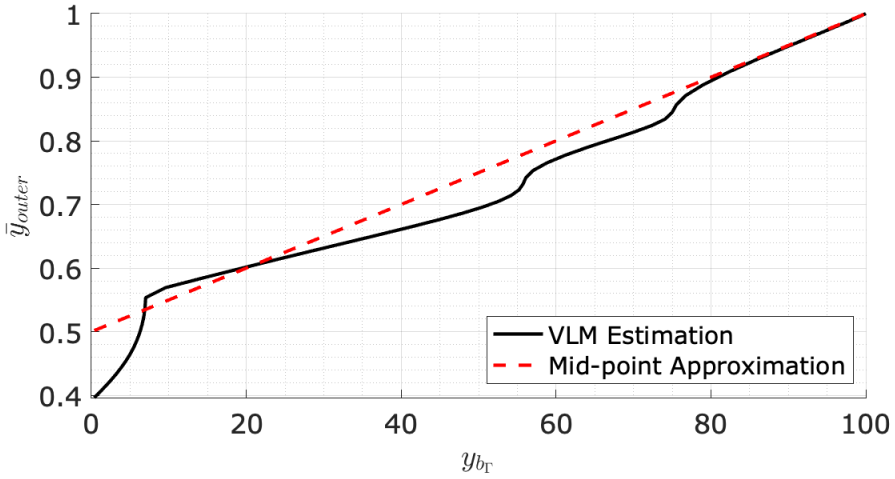

Figure 6.2: Change in the outer wing's acting center of lift, $\bar{y}_{\text{outer}}$, with variation of y_{b_Γ}, leading to improved C_{l_β} estimates

The aerodynamic parameter C_{l_α}, being the two-dimensional lift coefficient derivative with respect to α, was estimated across the wingspan to improve predictions of the stability derivative C_{l_β}. Figure 6.3 shows the change in C_{l_α} with span. Noting the dependency of the dihedral effect on C_{L_α}, and the change in y_{b_Γ} across configurations, using a constant C_{L_α} for the span is insufficient for use in vehicle modeling, particularly as y_{b_Γ} increases, indicated by Figure 6.3. For reference, the predicted constant wing C_{L_α} was 4.56. At lower values of y_{b_Γ} the use of a constant C_{L_α} may be sufficient, as C_{l_α} values close to the root contribute to

the dihedral effect more significantly than the outboard portion of the wing. It was found through the modeling process that significant error existed at larger values of y_{b_Γ} without this span-dependent term enforced.

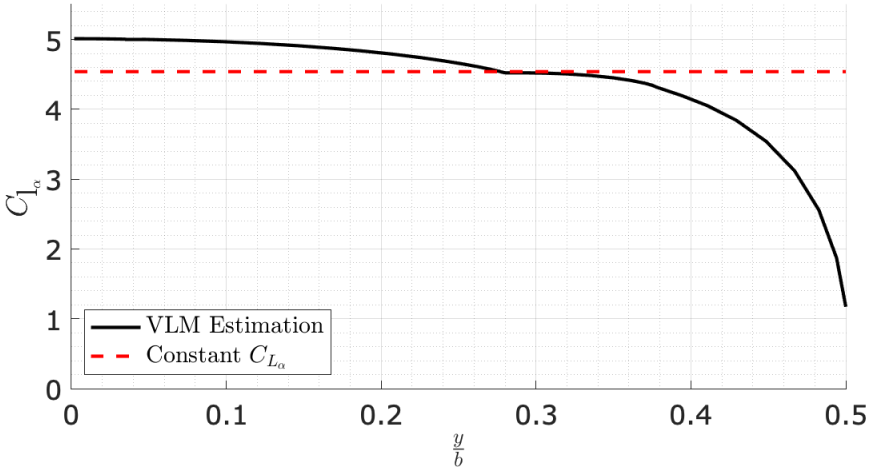

Figure 6.3: XFLR5 prediction of spanwise variation in C_{l_α}, used to improve modeling C_{l_β}

6.2 Predicted Dihedral Effectiveness

A refined grid of aircraft configurations was created for the MATLAB defined model with the intent to estimate changes in C_{l_β} across configurations. The equations of motion used to solve the varying aircraft configuration equilibriums assumed a fixed angle of attack, with the aircraft's speed, thrust, and horizontal stabilizer incidence angle being modified to resolve each configuration's equilibrium. The state matrices generated for the refined grid of aircraft configuration were resolved about $\dot{\Gamma} = 0\frac{^\circ}{\text{sec}}$. Equilibriums were evaluated for the follow configurations defined using the MATLAB active dihedral model: y_{b_Γ} varied from 0% to 95% in increments of 5% and Γ varied from 2° to 30° in increments of 5° starting at $\Gamma = 5°$. The VLM data points are generated based on a grid of dihedral angles and breakpoints similar to NASA Report No. 548, being dihedral angles of 5°, 10°, 15°, and

30°, and breakpoints of 0%, 7%, 50%, and 75%. The following set of results are reflective of the respective discretized grids, with linear interpolation used in the contours to give an understanding of the expected C_{l_β} between operation points.

The dihedral effect, C_{l_β}, mapped across Γ and $\dot{\Gamma}$, depicted in Figure 6.4, shows the expected response of the dihedral effect increasing with increased Γ with a fixed breakpoint. In general, the dihedral effect also decreases with Γ fixed and a breakpoint moving outboard. The MATLAB model shows a slight discrepancy in this, with $y_{b_\Gamma} = 10\%$ having the maximum C_{l_β}; this could be an artifact of modeling of wing C_{l_α} variation with span, of which an increased number of panels were used around $y_{b_\Gamma} = 7\%$. The VLM results displayed the expected result with the breakpoint located at the root maintaining the maximum dihedral effect. Equation (6.1) was developed from Etkin and Reid, and used to compute the MATLAB values of C_{l_β} from the model [13],

$$C_{l_\beta} = \frac{\rho u_0 S \frac{b}{2}}{L_v} \tag{6.1}$$

where L_v is the contribution of v to the aircraft roll moment, as given in the body frame. Using a contour mapping of C_{l_β}, similar results to that of NASA Report No. 548 are found, in which the equivalent dihedral effect of the traditionally root fixed dihedral can be maintained by shifting the breakpoint outboard and increasing the dihedral angle. For example, with $y_{b_\Gamma} = 0$ and $\Gamma = 5°$, a similar dihedral effect can be maintained by using $y_{b_\Gamma} = 75\%$ and $\Gamma = 15°$. These contour plots highlight the roll stiffness capability available to the vehicle given a specified breakpoint. If desired, a controller could be developed using this C_{l_β} delineation, providing increased dihedral angle while at increased angles of attack, to reduce the vehicle's perturbation to lateral gusts.

With the VLM estimates being used as method of verifying the MATLAB model,

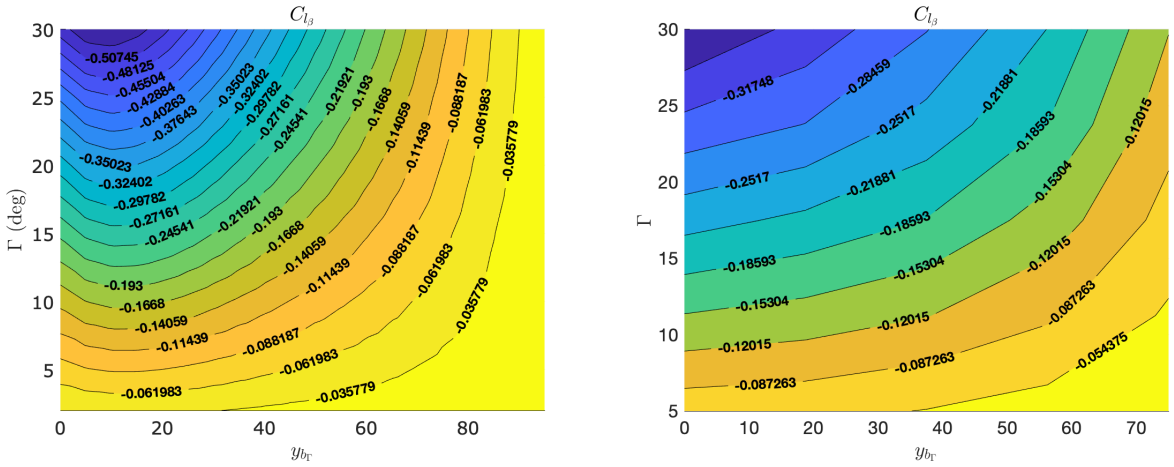

(a) MATLAB model C_{l_β} for $0\% < y_{b_\Gamma} < 95\%$ and $2° < \Gamma < 30°$

(b) VLM prediction of C_{l_β} for $0\% < y_{b_\Gamma} < 75\%$ and $5° < \Gamma < 30°$

Figure 6.4: Contour mapping of C_{l_β} for aircraft configurations with variation in $< y_{b_\Gamma}$ and Γ

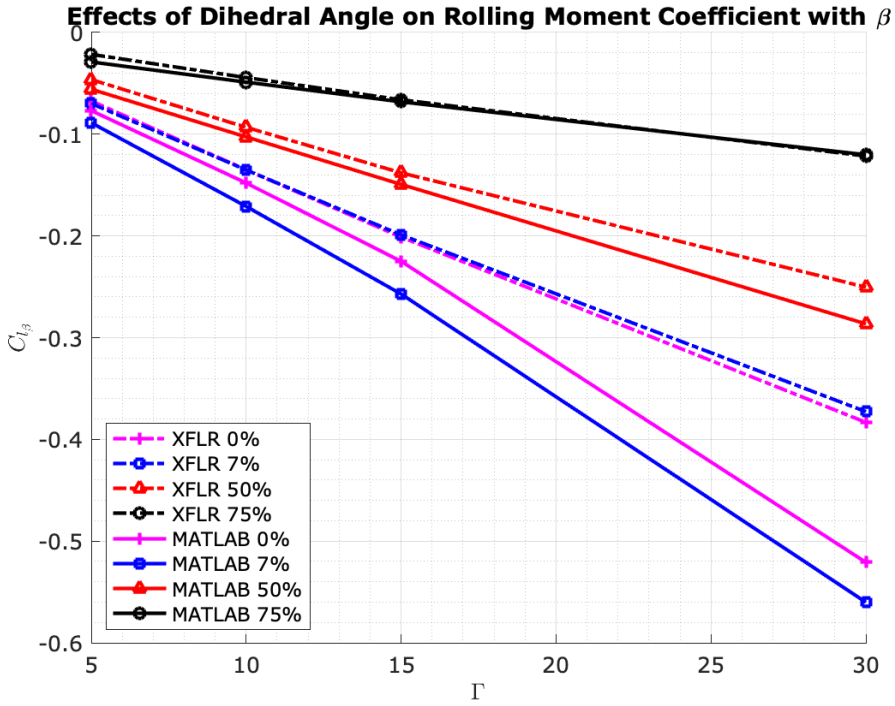

Figure 6.5: 2-D comparison of C_{l_β} between VLM prediction and MATLAB model for breakpoints 0%, 7%, 50%, and 75%

Figure 6.5 shows a 2-D plot of the contours, highlighting the general trend of C_{l_β} for the models is consistent across dihedral angles and breakpoints. For breakpoints further outboard, the MATLAB model better aligns with the VLM predictions. Breakpoints closer to the root (i.e. $y_{b_\Gamma} < 50\%$) measure C_{l_β} significantly larger at increased dihedral angles in the MATLAB model, lacking congruence with the VLM.

6.3 Dynamic Modal Responses

An investigation of the dynamic modal responses for various aircraft configurations was performed. The MATLAB and VLM models were evaluated for a set of Γ and y_{b_Γ} equilibriums, with the discretizations provided in Section 6.2. Each vehicle configuration was evaluated for the lateral and longitudinal dynamic stability parameters at their respective equilibriums. A description of the modal responses and their variation with Γ and y_{b_Γ} is provided. Linear interpolation was used in the contours to give an understanding of the expected dynamic modal responses between operation points.

It was expected that the Dutch roll damping ratio decrease with an increasing dihedral angle, leaving the vehicle more susceptible to the Dutch roll phenomenon at higher dihedral angles. Maintaining the breakpoint fixed at the root, this predicted response is visualized in both the MATLAB and VLM models in Figures 6.6a and 6.6b. Holding the dihedral angle constant, analyzing an increasing dihedral breakpoint, the Dutch roll damping ratio increases, indicating a reduction in excitation amplitude of this mode. Notice however there does appear to be two pockets in which the Dutch roll has a significantly reduced damping ratio. This was seen in the MATLAB model and coarsely in the VLM model; it was uncertain the root cause for this, however, it could be attributed to the increased number of panels in the VLM modeling schema. The natural frequencies for the MATLAB and VLM models

are depicted in Figure 6.6c and 6.6d respectively. The natural frequency varies marginally across the configurations, but peaks in both models in the area of $\Gamma = 30°$ and $y_{b_\Gamma} = 7\%$. In all cases, the minimum Dutch roll damping ratio and natural frequency specified by MIL-F-8785C in Table 4.2 was met for the MATLAB and VLM configurations.

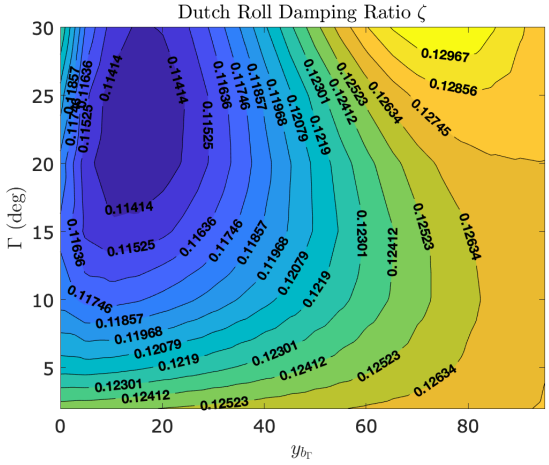

(a) MATLAB - Dutch roll damping ratio ζ

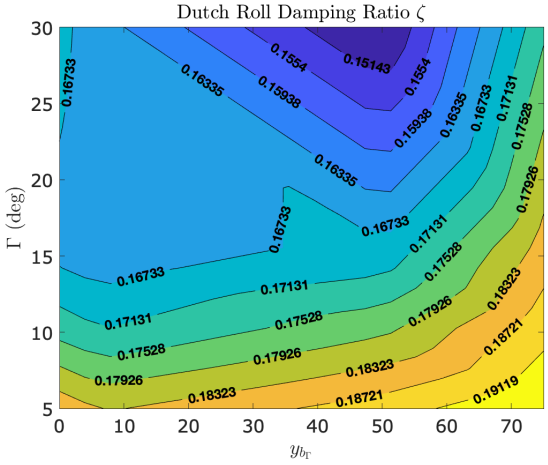

(b) XFLR - Dutch roll damping ratio ζ

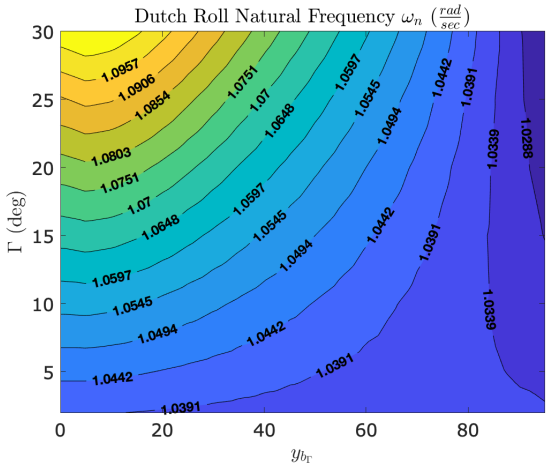

(c) MATLAB - Dutch roll natural frequency $\omega_n(\frac{rad}{\text{sec}})$

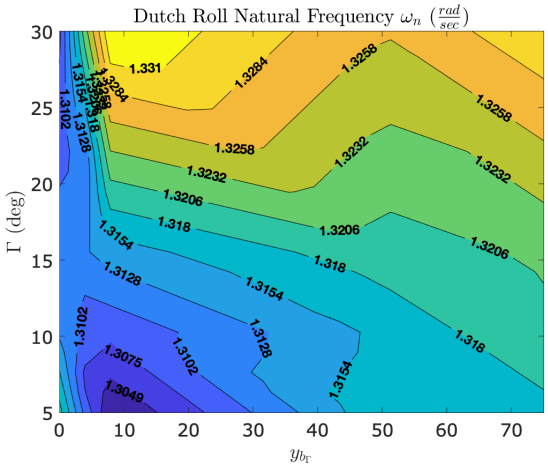

(d) XFLR - Dutch roll natural frequency $\omega_n(\frac{rad}{\text{sec}})$

Figure 6.6: Mapping of the Dutch roll modal characteristics, damping ratio and natural frequency, with changes in y_{b_Γ} and Γ for VLM predictions and the MATLAB model

The spiral mode response for the MATLAB and VLM models is shown in Figure 6.7. The expected response for spiral mode dependency on the dihedral angle was increased

stability with an increasing dihedral angle and consequently decreased time to half amplitude. This modal response was observed in the MATLAB model in Figure 6.7a, however, the VLM model in Figure 6.7b trended similarly but with some discrepancy. Investigation of the raw spiral mode eigenvalues for the VLM model shows that as the dihedral angle was reduced and the breakpoint moved outboard, the spiral mode became unstable at points, indicated by the negative spiral mode $t_{\frac{1}{2}}$ values. As well, there appears to be a local extremum in the VLM modeling at the $y_{b_\Gamma} = 50\%$ and $\Gamma = 10°$ point, which biases the contour mapping. Improved visualization of the eigenvalues given by the root locus plots for both the MATLAB and VLM models are found in Figures A.1 - A.4 in Appendix A. The MIL-F-8785C requirements allow for spiral mode instability, with a minimum time to double amplitude of 8 seconds, meaning the MATLAB model meets this requirement at all operating points. The VLM model meets this requirement, but only at points where $t_{\frac{1}{2}} > -8$ in Figure 6.7b.

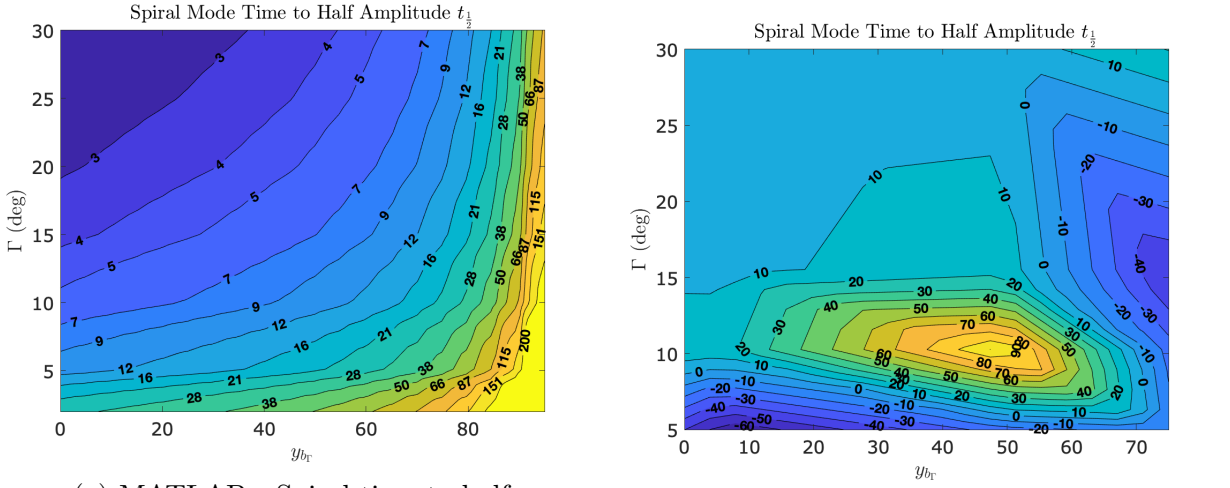

(a) MATLAB - Spiral time to half amplitude

(b) XFLR - Spiral time to half/double amplitude

Figure 6.7: Mapping of spiral mode time to half or double amplitude, $t_{\frac{1}{2}}$, with changes in y_{b_Γ} and Γ for VLM predictions and the MATLAB model

The phugoid and short-period modal responses of the MATLAB model are shown for purposes of verification of realistic system response of the longitudinal dynamics. It was

expected that at lower dihedral angles, no matter the dihedral breakpoint, the phugoid and short-period mode responses would have minimal variation. It was predicted that at higher dihedral angles, with breakpoints close to the root, there would be some deviation in the modal responses as the projected area of the wing would deviate most significantly at these points relative to a zero dihedral configuration. Figures 6.8a and 6.8b show the damping ratio associated with the phugoid and short-period modes, respectively.

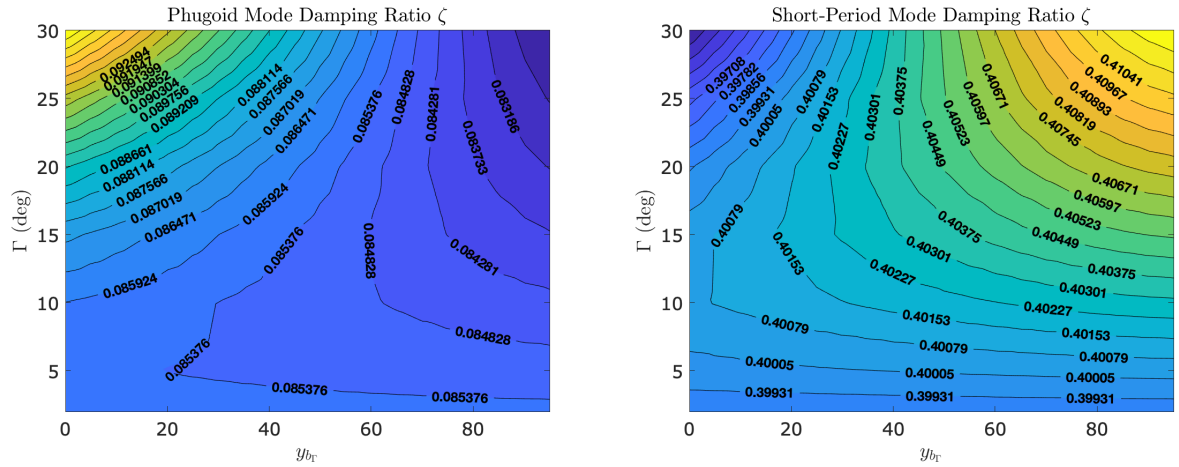

(a) Phugoid mode damping ratio (ζ)

(b) Short-period mode damping ratio (ζ)

Figure 6.8: Longitudinal dynamic modal response time constants, τ, with changes in y_{b_Γ} and Γ for the active dihedral model

Consider a perturbation in the vertical direction, such that the wings encounter a change in angle of attack. The phugoid mode shows a maximum damping ratio at $y_{b_\Gamma} = 0$ and $\Gamma = 30°$, indicating a quicker settling time to a disturbance in this mode. This modal response was investigated to acknowledge that given an impulse disturbance exciting the longitudinal modes, the large dihedral angle and small breakpoint configurations will be less perturbed by the excitation compared to smaller dihedral angles. While this is not factored into later results in terms of gust rejection, this could be considered as an added benefit to gust rejection, the fact of larger dihedral angles observing a more damped response to modal excitation. The response of the vehicle configurations to excitation of the short-period

mapped similarly to that of the phugoid mode but notably is significantly more stable, with damping ratio occurring at the largest dihedral breakpoints and largest dihedral angles. All combinations of y_{b_Γ} and Γ meet the MIL-F-8785C requirements specified in Table 4.2 for the phugoid and short-period damping ratios.

6.4 Need for Linear Multi-Parameter Varying System

Through the implementation of the LPV system, it was originally determined that an LPV system would increase the model accuracy for active dihedral. Order reduction of the LPV system's state dependencies is considered ideal for reducing computation times and model simplification. In order to capture the effects of flapping and various dihedral angles, the model must be dependent on Γ and $\dot{\Gamma}$. To visualize the change in the system state matrix, and its dependency on both Γ and $\dot{\Gamma}$, the change in state matrix, $A(\Gamma, \dot{\Gamma})$, for configuration $y_{b_\Gamma} = 0$ and $\Gamma = 5°$, is plotted in Figures 6.9 and 6.10.

Figure 6.9 shows the sensitivities of the rate terms $\dot{u}$, $\dot{w}$, $\dot{q}$ and $\dot{\Gamma}$ with respect to change in Γ for the system. There is no observed dependence of $\dot{u}$ with change in dihedral angle, as it remained constant across all Γ and $\dot{\Gamma}$, shown in Figure 6.9a. Holding all terms constant in the equations of motion, excluding the dihedral angle, a $\Delta\Gamma$ does not alter the normal force generated by the wing, but simply the vector in which the normal force is acting. Due to no change in normal force generated, the total drag generated remains fixed, and hence $\dot{u}$ remains unchanged. With this same method of thinking, Figure 6.9b shows that with a change in dihedral angle, it was expected $\dot{w}$ changes as the projected component of the normal force on the z^B axis changes, with the rotation matrix defined in Equation (3.9). In the same means, there is a direct dependence of the change in $\dot{w}$ with respect to the initial dihedral angle. For example, compare two cases of a 30° increase in dihedral

angle starting from $\Gamma_0 = 0°$ versus $\Gamma_0 = 30°$. Using the rotation matrix in Equation (3.9), starting at $\Gamma = 0°$ leads to an approximate 14% decrease in the vertical lift while starting at $\Gamma = 30°$ leads to a 42% decrease in vertical lift. This example corresponds directly to Figure 6.9b, with a larger dihedral angle increasing the sensitivity of $\dot{w}$. In relation to the rate of change in pitch rate, observed in Figure 6.9c, any positive increase in dihedral angle leads to a reduction in vertical lift, and hence a pitch up moment due to the restorative forces of a $-C_{M_\alpha}$. Noting the dependency of pitching moment on airfoil and elevator trim angle, there is no direct correlation to the peak sensitivity of $\dot{q}$ to the equilibrium dihedral angle or $\Gamma = 0°$. Finally, the sensitivity of $\dot{\Gamma}$ to changes in Γ is zero for all states as $\dot{\Gamma}$ is driven by the input torque to the actuator, δ_τ.

A similar analysis to the former is conducted for the state matrix dependency on $\dot{\Gamma}$. Figure 6.10 shows the sensitivity in $\dot{u}$, $\dot{w}$, $\dot{q}$ and $\dot{\Gamma}$ to a unit change in $\dot{\Gamma}$, and how the sensitivity varied with change in parameters Γ and $\dot{\Gamma}$. The change in $\dot{u}$ due to a positive unit change in $\dot{\Gamma}$ was seen to increase at the instance of actuation, which was due to the decrease in wing relative angle of attack, directly reducing drag, leading to increased longitudinal speed. Figure 6.10a shows this was plausible no matter the dihedral angle or rate of flapping. Notice however that the sensitivity of $\dot{u}$ does not vary with dihedral angle, similar to previously, where the total lift generated by the wing does not change, but only the direction in which the lift is acting. There was an observed state dependence on $\dot{\Gamma}$ which indicates that a positive unit change in $\dot{\Gamma}$ at large positive actuation rates affects $\dot{u}$ less than that of a positive unit change when actuating at a large negative rate. This can be thought of in terms of drag. Consider a sudden large positive actuation rate while actuating in the negative direction, this motion decreases the $\Delta\alpha$ experienced due to flapping, instantly reducing drag, leading to an acceleration in the opposite direction.

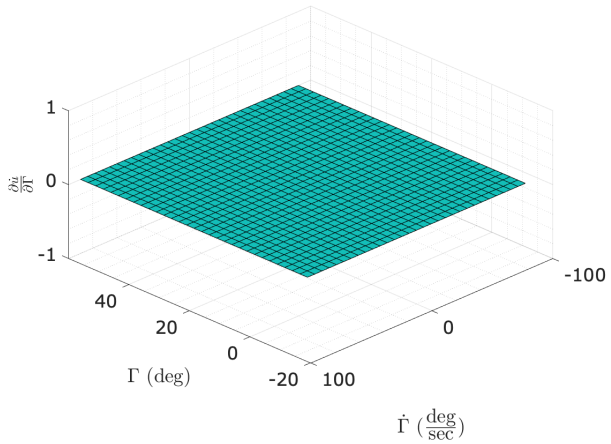

(a) Partial derivative of $\dot{u}$ with respect to Γ

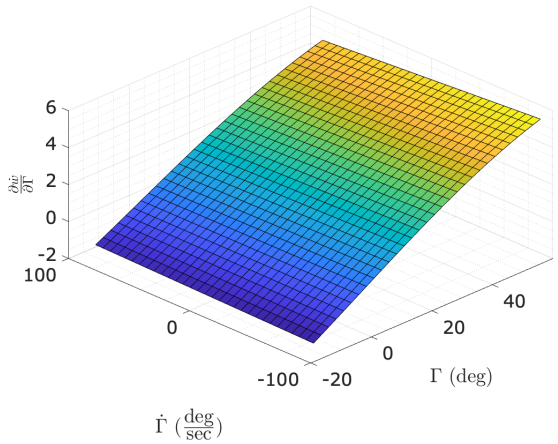

(b) Partial derivative of $\dot{w}$ with respect to Γ

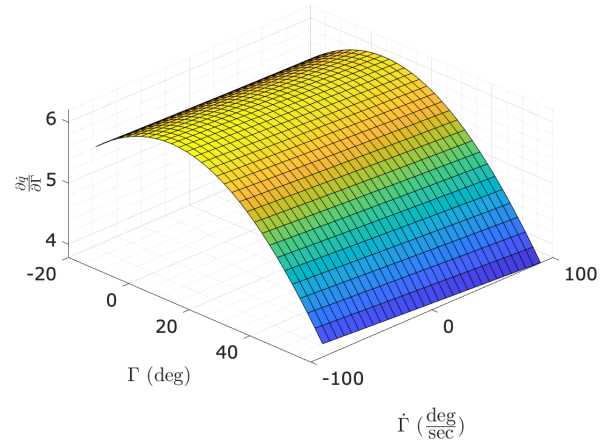

(c) Partial derivative of $\dot{q}$ with respect to Γ

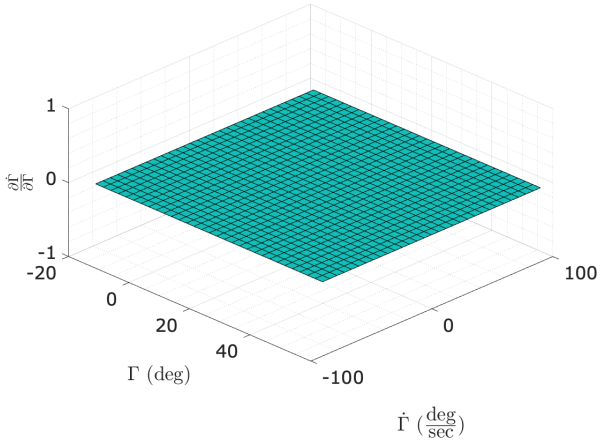

(d) Partial derivative of $\dot{\Gamma}$ with respect to Γ

Figure 6.9: First order partial derivatives of the LPV system state matrix, with respect to Γ, and their dependence on Γ and $\dot{\Gamma}$

The change in $\dot{w}$ to a positive unit increase in $\dot{\Gamma}$ is denoted in Figure 6.10b. It is shown that the sensitivity of this term to a varying state of $\dot{\Gamma}$ is minimal in comparison to that of Γ. Recalling that $\dot{w}$ is the acceleration acting along the $+z^B$ axis, that being downward, a positive increase in $\dot{\Gamma}$ causes the wing to actuate upward, leading to an instantaneous flapping force pushing the aircraft downwards, also given as a positive $\dot{w}$. Conversely, for a negative unit increase in $\dot{\Gamma}$, there exists a resulting increase in upward force, corresponding to a negative $\dot{w}$. The difference in sensitivity can be understood as the projected component of

vertical lift generated from the normal force create by $\Delta\dot{\Gamma}$ is highly sensitive to wing dihedral angle. Intuitively, the maximum lift generated occurs at $\Gamma = 0°$, indicative of Figure 6.10b.

Figure 6.10c shows the sensitivity of $\dot{q}$ to a change in $\dot{\Gamma}$. The minimum for this term occurs when the system has a large dihedral angle and a large negative flapping rate. In general, the change in $\dot{q}$ varied some with $\dot{\Gamma}$, but primarily with variation in Γ. This sensitivity can be visualized as a correlated combination of Figure 6.10a and 6.10b, as a plunging velocity would result in an increased angle of attack and hence increased pitching moment, and a surge in longitudinal velocity would result in a positive pitching moment. Figure 6.10d shows the dependency of $\dot{\Gamma}$ upon itself, giving a one-to-one correspondence as expected.

Though the development of the LPV system, the input matrix B was made parameter-dependent in Γ and $\dot{\Gamma}$ (e.g. $B(\Gamma, \dot{\Gamma})$) with expectation that such dependency was required; upon evaluation of B at various Γ and $\dot{\Gamma}$, dependence existed only on Γ, as B did not vary when evaluated at $\dot{\Gamma} \neq 0\frac{^\circ}{\text{sec}}$. Having $B(\Gamma)$ modeled proved useful in capturing the additional adverse side force incurred when actuating the ailerons at higher dihedral angles. Figure 6.11 shows how the $\frac{\partial \dot{v}}{\partial \delta_a}$ term is better estimated through a parameter dependent matrix, $B(\Gamma)$, for the aircraft configuration of $y_{b_\Gamma} = 0$ and $\Gamma = 5°$.

Figure 6.11a displays the variation in the raw value of $\frac{\partial \dot{v}}{\partial \delta_a}$ with changes in Γ and $\dot{\Gamma}$. The contour plot highlights that for all positive values of Γ, a positive input of aileron will induce a side force in the $-y^B$ direction, and increasingly in magnitude as Γ increases. The surface plot also shows that, as modeled, there is no dependency of the side force on $\dot{\Gamma}$. This makes sense from a linear modeling perspective as both wings flapping symmetrically change the angle of attack equivalently at the spanwise cross-section in which the ailerons acted, leading to no additional differential in side force. A nonlinear computational fluid dynamics (CFD) model would be required to capture the true effects of flapping paired with aileron

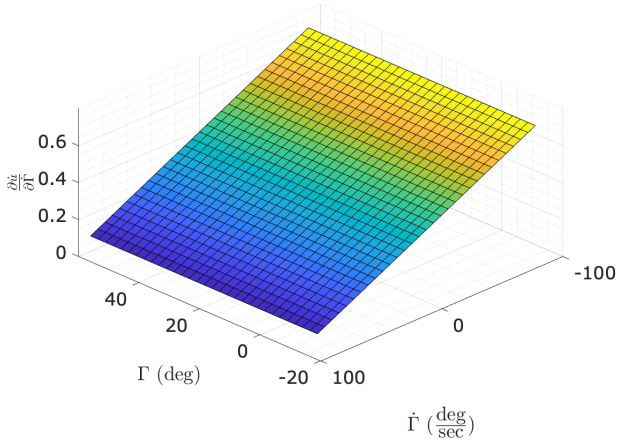

(a) Partial derivative of $\dot{u}$ with respect to $\dot{\Gamma}$

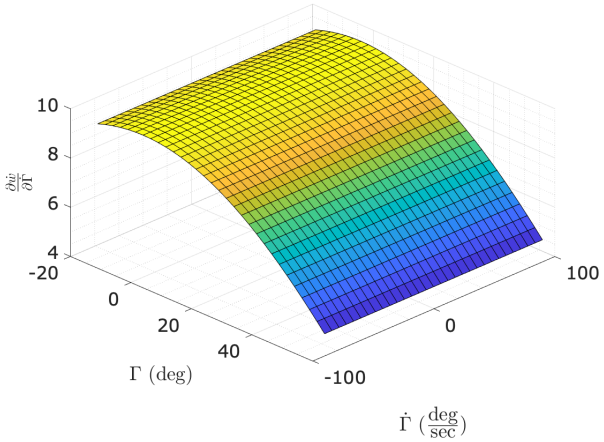

(b) Partial derivative of $\dot{w}$ with respect to $\dot{\Gamma}$

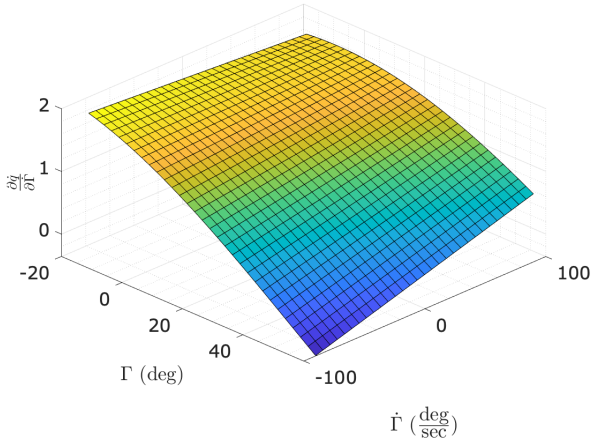

(c) Partial derivative of $\dot{q}$ with respect to $\dot{\Gamma}$

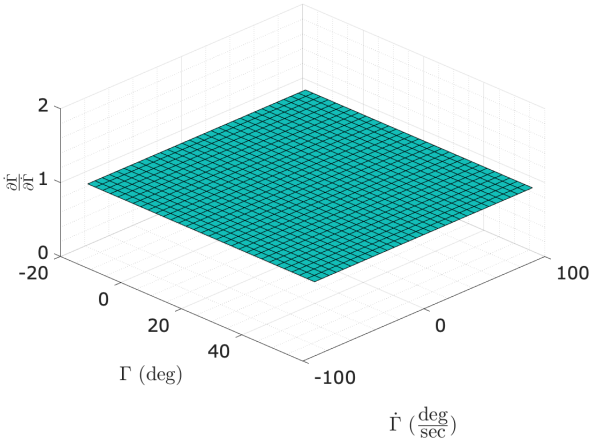

(d) Partial derivative of $\dot{\Gamma}$ with respect to $\dot{\Gamma}$

Figure 6.10: First order partial derivatives of the LPV system states, $A(\Gamma, \dot{\Gamma})$, with respect to $\dot{\Gamma}$, and their dependence on Γ and $\dot{\Gamma}$

deflection and the effect on side force, however, for this fidelity of modeling the results were inline and as expected. Figure 6.11b is similar to Figure 6.11a, but normalized with the equilibrium value to visualize how the side force is changing with a non-equilibrium dihedral angle. The red line shows the point at which $\Gamma = 5°$, with a normalized value of one, that spans all values of $\dot{\Gamma}$. It is observed that as Γ approaches zero, the term in the Jacobian does as well, corresponding to no side force associated with a deflection in the ailerons at $\Gamma = 0°$. Continuing with the same logic, as the dihedral angle becomes negative, the side

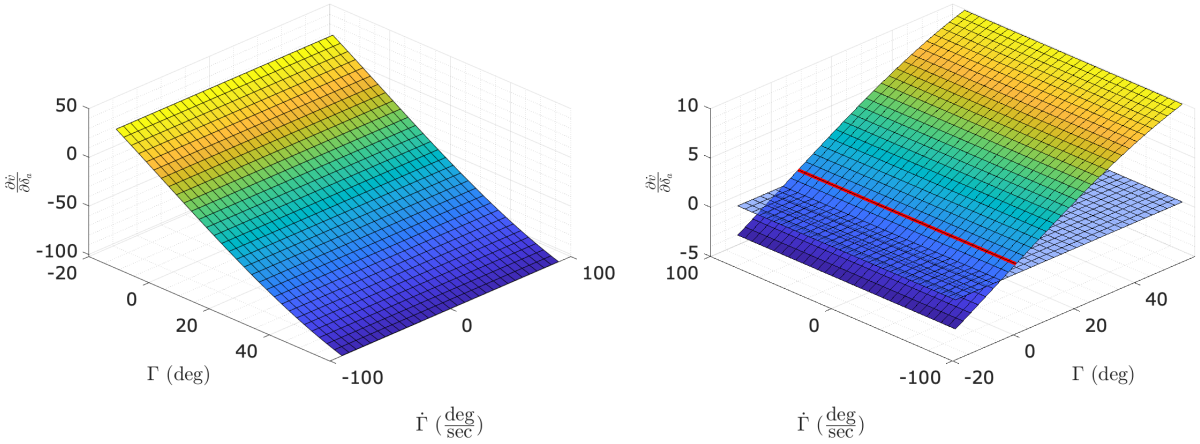

(a) Effect of δ_a on $\dot{v}$

(b) Effect of δ_a on $\dot{v}$ normalized

Figure 6.11: First order partial derivative of the LPV system inputs, $B(\Gamma, \dot{\Gamma})$, with respect to δ_a, and their dependence on Γ and $\dot{\Gamma}$

force generated by the ailerons begins to act in the opposing direction, with a positive aileron input leading to a force in the $+y^B$ direction; this can be visualized using Figure 3.4. The amplitude of the ailerons' effect on side force grows increasingly negative as the dihedral angle increases.

6.5 LPV System Stability Assessment

It was possible to test the stability of the active dihedral system with a single fixed state matrix through eigenvalue evaluation, as shown previously through the stable dynamic modal responses in Section 6.3. The stability of the LPV system proved more challenging to evaluate; the two main methods arising from Section 5.1 regarding solving the Lyapunov equation were attempted. The first method of resolving stability was to identify a solution, P_m, to the LMI given in Equation (5.5). To do so, the MATLAB Robust Control Toolbox was used to numerically evaluate a matrix P_m that solved a reduced set of LMIs structured like that of Equation (5.5). The state matrices, A_ρ, were defined through a finite discretization of

a bounded set of Γ and $\dot{\Gamma}$, evaluated using the state matrix $A(\Gamma, \dot{\Gamma})$, given in Equation (3.96). The spatial discretization, leading to a finite set being ρ_n, where $\rho_n \in \rho$, was determined through assessment of computational limitations, leading to the bounds of $-15° \leq \Gamma \leq 60°$ and $-90\frac{°}{s} \leq \dot{\Gamma} \leq 90\frac{°}{s}$, in increments of 2.5° and $6\frac{°}{s}$, respectively. A lower bound of $-15°$ was included in an attempt to consider the potential for operating at negative dihedral angles, giving additional gust rejection capability when flapping through $\Gamma = 0°$ with a $-\dot{\Gamma}$. An upper limit of $\Gamma = 60°$ was established for purpose of not allowing the UAS to dump more than 50% of its lift. The bounds of $\dot{\Gamma}$ were selected using engineering judgment based on previous work by Fisher et al. [26], in which the maximum flapping rate available for actuation was approximate $48\frac{°}{s}$; it is thought that double this rate could be obtained through improved mechanical system design and system integration, hence a maximum flapping rate magnitude of $90\frac{°}{s}$ [26].

The LPV system configurations evaluated for stability were $y_{b_\Gamma} = 0\%, 25\%, 50\%, 75\%$ and $\Gamma = 5°, 10°, 15°, 30°$. Table 6.2 shows the minimum and maximum dihedral angles and flap ratings identified, which could be included in the set of A_ρ, as an applicable P_m was found. By limiting the systems to these actuation bounds, and assuming the LPV state matrix is restricted to only the discretized set of A_ρ such that a true switched system exists, there existed exponential stability. Global exponential stability was not inherently found, as the Lyapunov functions, $V(\vec{x})$, for these systems were radially bounded. The parameter-dependent bounds presented in Table 6.2 indicate a minimum dihedral angle of 2.5°, which is a misnomer and an artifact of the discretized grid. Truly the system should be allowed to actuate down to, but not including, $\Gamma = 0$, as this is the point in which the system becomes marginally stable or sometimes given as neutrally stable in the spiral mode, leaving no solution to the Lyapunov equation.

y_{b_Γ}	Γ°_{eq}	$\Gamma^\circ_{\text{min}}$	$\Gamma^\circ_{\text{max}}$	$\dot{\Gamma}_{\text{min}}\frac{^\circ}{s}$	$\dot{\Gamma}_{\text{max}}\frac{^\circ}{s}$
0	5	2.5	60	-54	60
0	10	2.5	60	-54	54
0	15	2.5	60	-54	48
0	30	2.5	60	-54	48
25	5	2.5	60	-66	60
25	10	2.5	60	-66	60
25	15	2.5	60	-66	60
25	30	2.5	60	-78	54
50	5	2.5	60	-84	84
50	10	2.5	60	-84	72
50	15	2.5	60	-72	72
50	30	2.5	60	-60	54
75	5	2.5	52.5	-66	72
75	10	2.5	50	-90	90
75	15	2.5	50	-90	84
75	30	2.5	47.5	-90	84

Table 6.2: Proposed configuration operating ranges to improve stability conservatives

To indicate that a valid Lyapunov function was found and demonstrated stability, Figure 6.12 was created for the bounding configurations given in Table 6.2, corresponding to breakpoints of 0% and 75%, and dihedral angles of 5° and 30°. The Lyapunov function is plotted with perturbations of $\pm 5\frac{\text{ft}}{\text{s}}$ in both v and w to show the response of the system to excitation in both lateral-directional and longitudinal modes; the systems converge back to the equilibrium showing exponential stability.

With respect to the simulations presented here forward, the LPV system states were not restricted to the discretized states A_ρ. During initial development, with a low number of spatially discretized samples in Γ, the results were stable but chattery, indicative of a switched system's oscillatory behavior between states. To solve this, the states were not limited to the previously defined ρ_n, but were interpolated between states to provide a smoother transition and more accurate representation of the system dynamics. This method of interpolation did reduce the conservativeness of the stability assessment, as additional proofs are required to show that convex combinations of two state matrices share a smooth

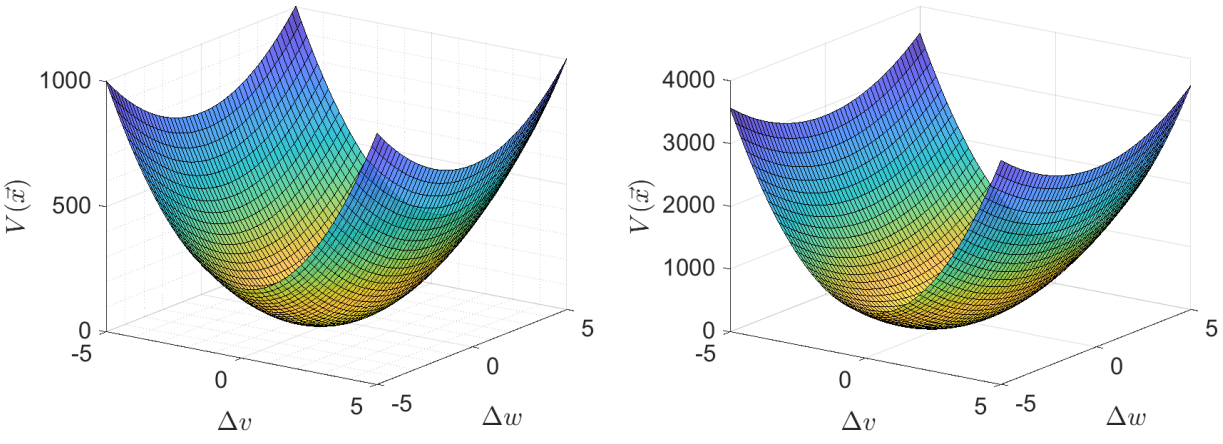

(a) $y_{b_\Gamma} = 0\%$ $\Gamma = 5°$

(b) $y_{b_\Gamma} = 0\%$ $\Gamma = 30°$

(c) $y_{b_\Gamma} = 75\%$ $\Gamma = 5°$

(d) $y_{b_\Gamma} = 75\%$ $\Gamma = 30°$

Figure 6.12: Lyapunov functions, $V(\vec{x})$, corresponding to the bounded operating ranges for specified configurations, showing exponential stability for perturbations of $\pm 5 \frac{\text{ft}}{\text{s}}$ in v and w

and common Lyapunov function, leading to exponential stability [33].

In terms of the active dihedral system's observed stability against artificial discrete 1-cosine gusts and continuous segments of turbulence, most simulation instances were found stable through the convergence of the system back to an equilibrium. The bounds for Γ and $\dot{\Gamma}$ in Table 6.12 were conserved in this study, with the exception of allowing the system to actuate past 2.5° to 0°, as discussed previously. No vehicle instability was immediately

observed when exceeding the Γ and $\dot{\Gamma}$ restrictions. There were instances encountered in which the feedback controller itself drove the system unstable. This primarily occurred in the case where the dihedral breakpoint was moved outboard, and the vehicle would diverge from equilibrium due to excessive penalty assigned to the vertically related states (z,w). As well, instability produced by the gain scheduled controller caused continual overshooting of the equilibrium.

As discussed by Xu et al. [34], it is possible to attempt the creation of a continuously differentiable polynomial fitting for a solution to the Lyapunov equation that solves the algebraic inequality for all operating points. An attempt was made to resolve a set of equations about the given operating points and the reduced set of previously constrained states, $A(\rho_n)$, leading to a solution to the Lyapunov equation. A search was conducted across a variety of polynomial orders, including higher-order solutions, and no set of polynomials successfully solved the algebraic inequality at all defined operating points. Through this inconclusive attempt at improving the quantification of system stability at all operating points, ρ, system stability was evaluated only on the ability to generate a solution, P_m, to the LMI for the individual operating states.

6.6 A Case for Active Dihedral

6.6.1 Discrete 1-Cosine Gust

A general case was developed to show the benefit of an active dihedral system on a fixed-wing air vehicle. A single aircraft configuration was defined and tested with two different controllers, with the steady state response also being observed for baseline comparison. A 1-cosine wind gust with a gust gradient of 100ft, depicted in Figure 6.13, was used to

perturb the system. The aircraft configuration selected for this analysis was the MTD with $\Gamma = 5°$ and $y_{b_\Gamma} = 0$, to closely model that of the traditional MTD in flight. The baseline LPV model was implemented for all three simulations with the parameter varying portion used only in the active dihedral case due to the LPV system's dependency on Γ and $\dot{\Gamma}$ only. The steady state response was given as means for evaluating the aircraft's expected response to a vertical 1-cosine wind gust; an increased angle of attack should result in an altitude increase and also increased drag, reducing the ground speed of the vehicle. These expected responses to perturbations were observed, giving an indication that the vehicle and gust perturbations were modeled correctly.

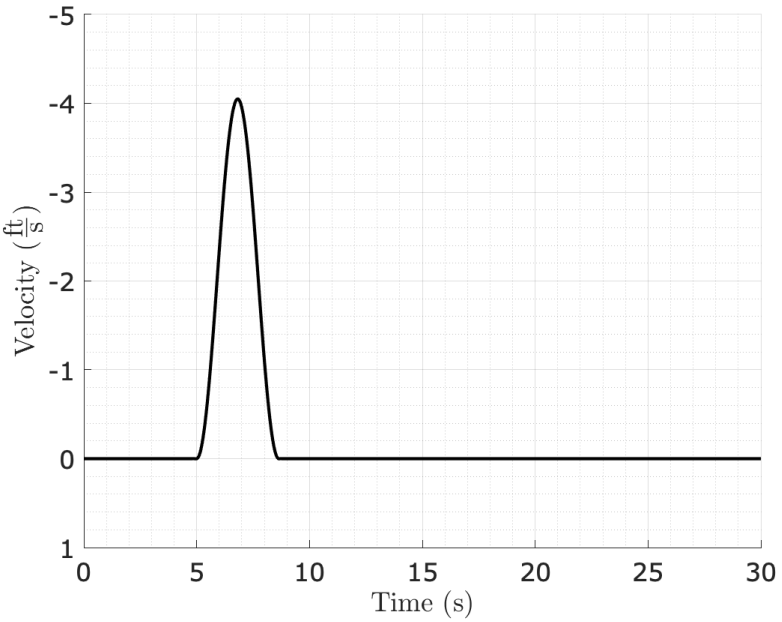

Figure 6.13: Discrete 1-cosine gust profile

The first controller evaluated was the traditional LQR elevator only controller, in which the elevator was used to change the vehicle's angle of attack in response to the wind gust. The second controller was the LQR active dihedral controller which directly dumps lift and flaps upward in response to an upward 1-cosine wind gust. The use of the elevator

is still incorporated in the active dihedral controller to maintain pitch authority over the aircraft; this assumption is maintained for active dihedral controller simulations here forward. The weights for these LQR controllers were each tailored such that the best response was obtained, with the best response being based on deviation in vertical position and velocity in the earth-fixed reference frame. Acceleration was considered for use in the controller to provide gust alleviation, however, to focus on gust rejection the LQR controllers here forward were designed with intention of keeping the aircraft on the desired trajectory, noting that active dihedral may cause additional increased load factor to meet this objective.

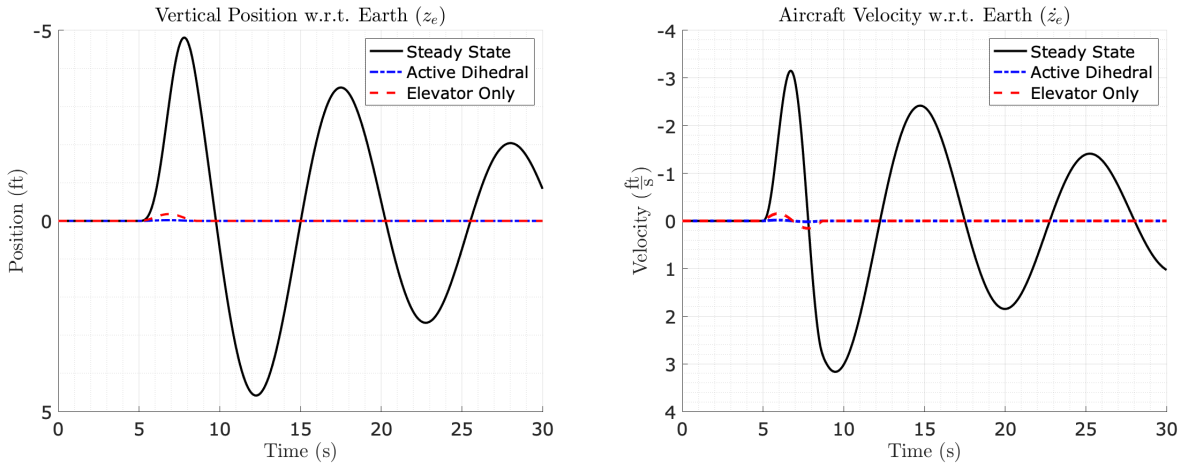

(a) Vertical position (z_e)

(b) Vertical velocity ($\dot{z}_e$)

The response for the three cases is displayed in Figure 6.14. The steady state response shows the aircraft's response to a general 1-cosine gust perturbation, resulting in a highly oscillatory change in position vertical position and velocity, with a peak amplitudes of -4.8ft and -3.15$\frac{ft}{s}$, respectively, shown in Figure 6.14a. The traditional elevator controller kept the vehicle's response to the perturbation minimal in terms of vertical position and velocity, reaching an absolute maximum position of 0.18ft and maximum absolute velocity of 0.155$\frac{ft}{s}$. The active dihedral controller provided a further reduction in trajectory deviation, with a maximum absolute position deviation of 0.020ft and a maximum absolute vertical velocity of 0.017$\frac{ft}{s}$.

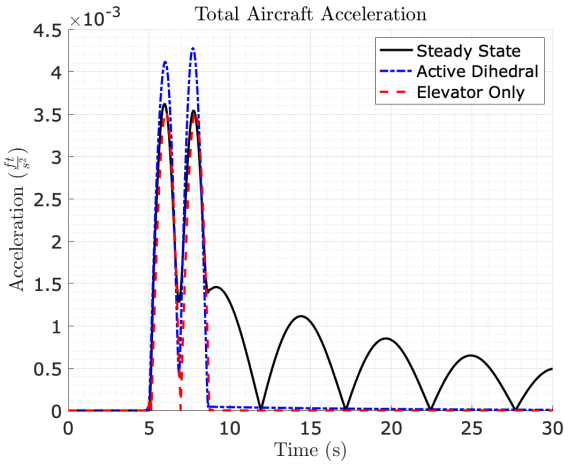

(c) Total vehicle acceleration

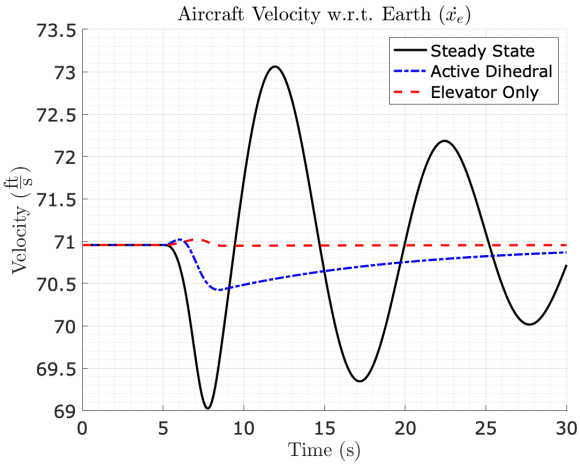

(d) Ground speed ($\dot{x}_e$)

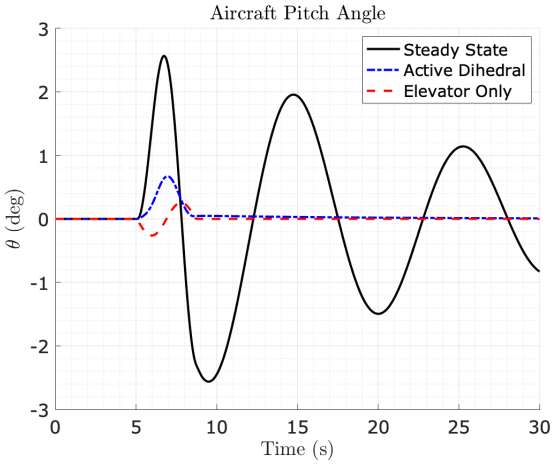

(e) Pitch angle (θ)

Figure 6.14: Evaluation of the steady state, elevator controller, and active dihedral controller responses to a single 1-cosine gust disturbance

The total acceleration for all three cases, depicted in Figure 6.14c, indicated the forces experienced by each system are on the same order of magnitude. Active dihedral did have the largest magnitude of acceleration. During the act of actuating the wings, the drag is increased, causing the reduction in $\dot{x}_e$, located in Figure 6.14d. The active dihedral system appears to maintain its vertical trajectory, but at the cost of a reduction in ground speed through drag. The pitch angle, shown in Figure 6.14e, highlights how the elevator controller attempts to pitch the vehicle nose down to reject the gust, leading to the increase in $\dot{x}_e$.

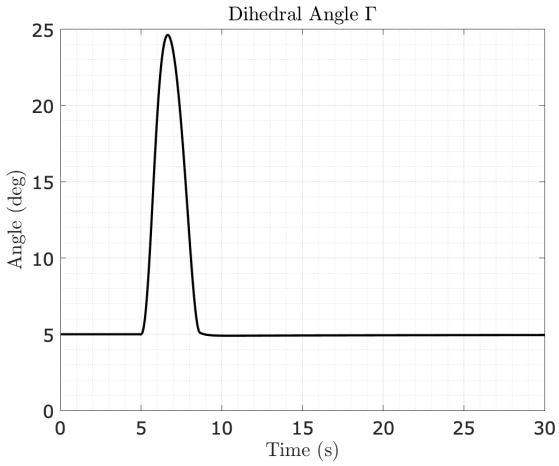

(a) Dihedral angle (Γ)

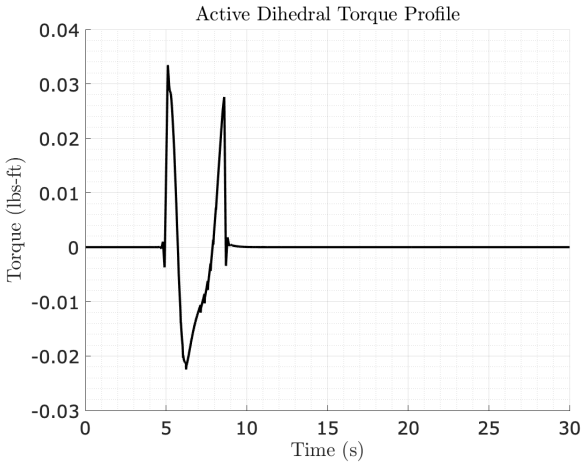

(b) Input torque (δ_τ)

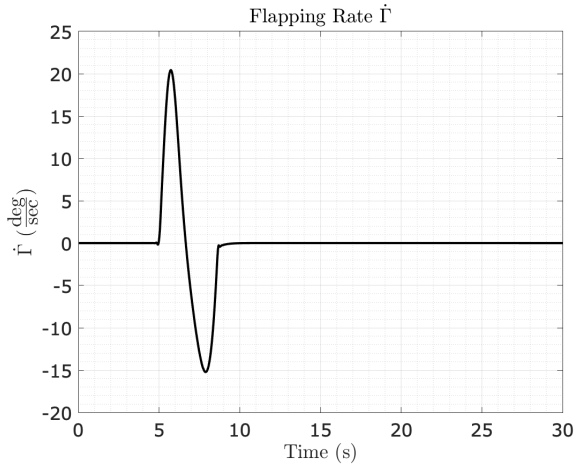

(c) Flapping rate ($\dot{\Gamma}$)

Figure 6.15: Active dihedral system actuating to reject a discrete gust disturbance

With respect to the active dihedral controller, the plot of dihedral variation over the course of gust rejection is shown in Figure 6.15a, with a maximum dihedral angle of 24.64° obtained. Figure 6.15c indicates the required torque, in which the controller inputs a positive torque, inducing a positive $\dot{\Gamma}$, increasing the dihedral angle. A negative torque is then applied to bring $\dot{\Gamma} = 0\frac{^\circ}{s}$ at the peak dihedral angle, and the inverse sequence for returning the dihedral angle back to its equilibrium position.

6.6.2 Continuous Turbulence

The active dihedral system was performance tested against a continuous turbulence gust, similar to that of turbulent boundary layers that could exist in low altitude flight or on ship decks. The wind gust tested against is shown in Figure 6.16, with the profile being generated through the von Kármán turbulence model described in Section 3.10.2. In the process of generating the gust, a 100ft length scale was selected for the disturbance, similar to that of the gust gradient for the 1-cosine gust. A standard deviation in the wind gust was selected to be $0.5\frac{\text{ft}}{\text{s}}$. The gust profile was created for an entire 30 second period, however, it was desired to test the system only for 10 seconds in a 30 second simulation, giving time to assure static stability with no gusts and sufficient settling time back to equilibrium. Due to this, the wind profile generated does not maintain a root mean square (RMS) of zero. This artifact does not deter the purpose or results of the simulation which is to make a comparison of active dihedral performance to the traditional elevator only controller subjected to this type of turbulence.

Figure 6.17 shows the response of the active dihedral controller, applied to the $y_{b_\Gamma} = 0$ and $\Gamma = 5°$ configuration, against the turbulent gust model. While the elevator only controller is able to keep the vehicle within 0.058ft of the desired vertical trajectory, the

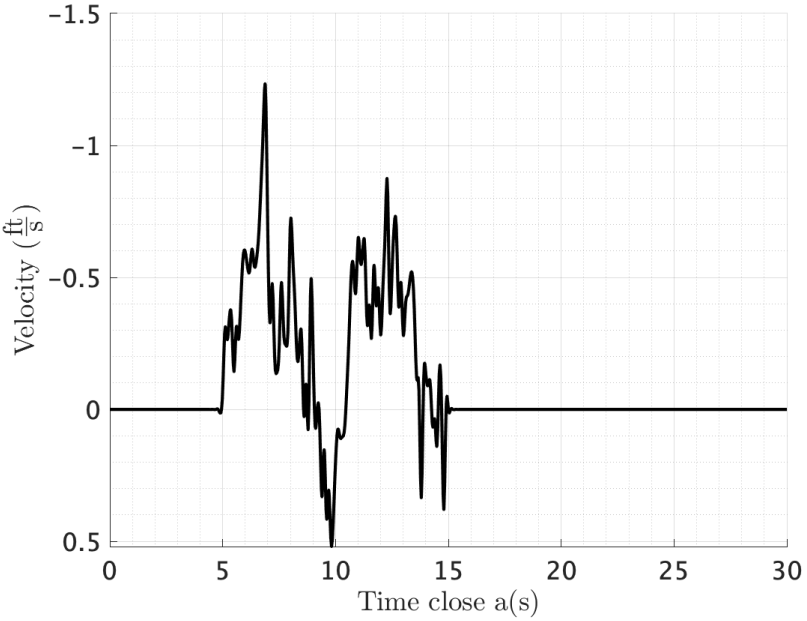

Figure 6.16: Continuous turbulent wing gust profile

active dihedral system does reduce the system's perturbation to 0.011ft, as seen in Figure 6.17a. Of note is the significant reduction of magnitude in vertical velocity the vehicle experiences with active dihedral, with the maximum vertical velocity being reduced from $0.29\frac{ft}{s}$ to $0.05\frac{ft}{s}$. In terms of acceleration, the active dihedral system does observe a large magnitude of acceleration compared to the elevator only controller, seen in Figure 6.17c. With respect to the force generated from the scale of acceleration, it is minimal; a larger wind gust would be required to observe any exacerbated acceleration effects of the active dihedral controller. Similar to the 1-cosine wind gust, the total ground speed is reduced while using active dihedral, but the total amount in which the ground speed decreases is small as the disturbance magnitude is also small. Due to the system flapping its wings in an attempt to reject the gust, the aircraft's pitch angle is increased due to the flapping effect, seen in Figure 6.17e, leading to the reduction in airspeed.

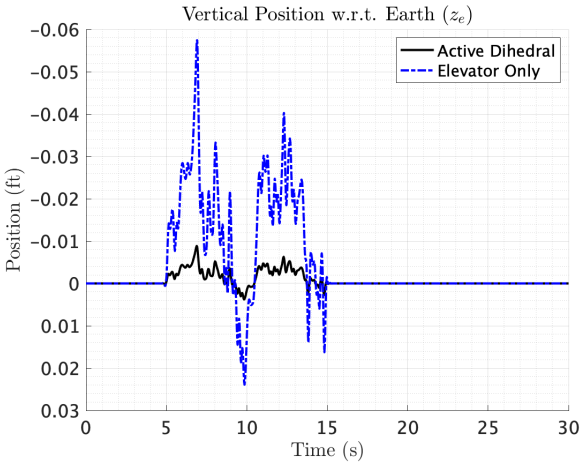

(a) Vertical position (z_e)

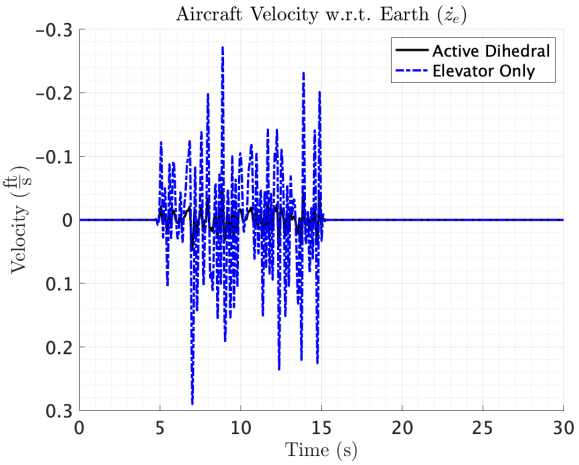

(b) Vertical velocity ($\dot{z}_e$)

The dihedral angle is shown in Figure 6.18a, with the dihedral angle increasing with an upward wind gust to dump lift, and decreasing with a downward wind gust to gain lift. The pitch angle of the vehicle somewhat corresponds with the dihedral angle as the vehicle is altering its angle of attack to reduce and gain lift. Notice that the dihedral angle does reach its railed lower limit at $\Gamma = 0$ while flapping downwards; this is intentional to prevent an unstable system. The maximum dihedral obtained while rejecting this wind gust is 26.5°. Shown in Figure 6.18b is also torque used by the controller to actuate the wing. The torque plotted is an unrealistic model of the true torque required to actuate the wing, as only the wing's inertia is accounted for and no lifting forces; the true torque required is calculated during post-processing. The input torque from the controller varies sharply over the course of the disturbance, leading to a fluctuation in flapping rate response, depicted in Figure 6.18c.

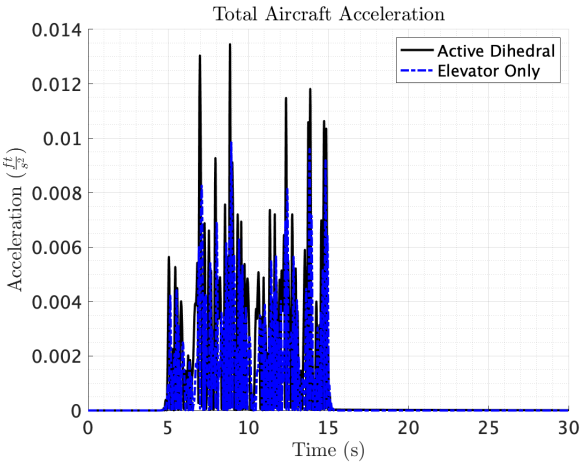

(c) Total vehicle acceleration

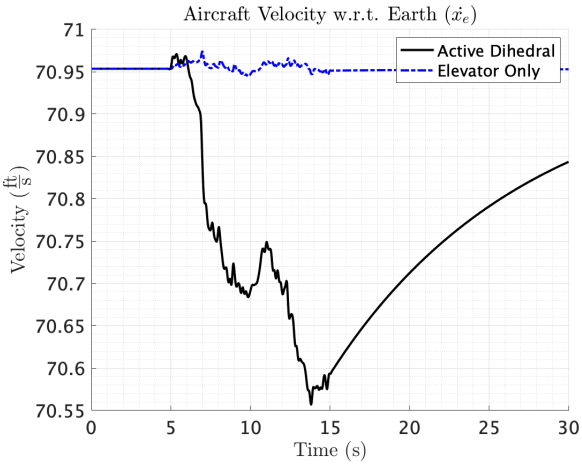

(d) Ground speed ($\dot{x}_e$)

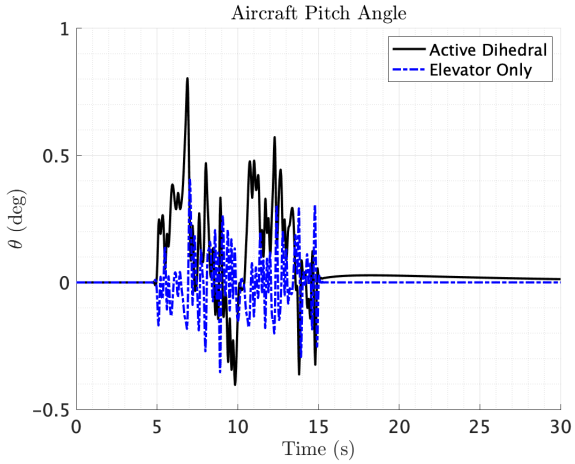

(e) Pitch angle (θ)

Figure 6.17: Evaluation of the elevator controller and active dihedral controller responses to a continuous turbulent gust disturbance

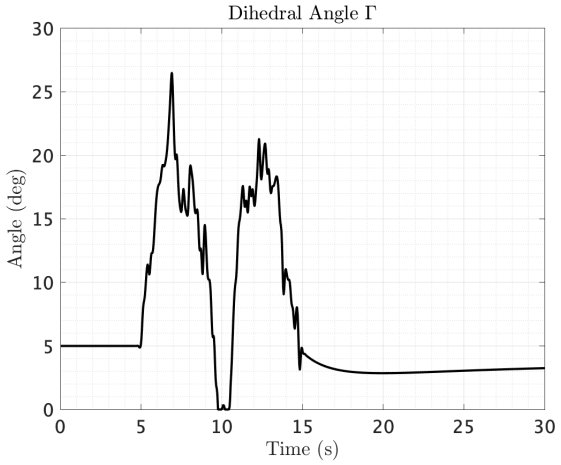

(a) Dihedral angle (Γ)

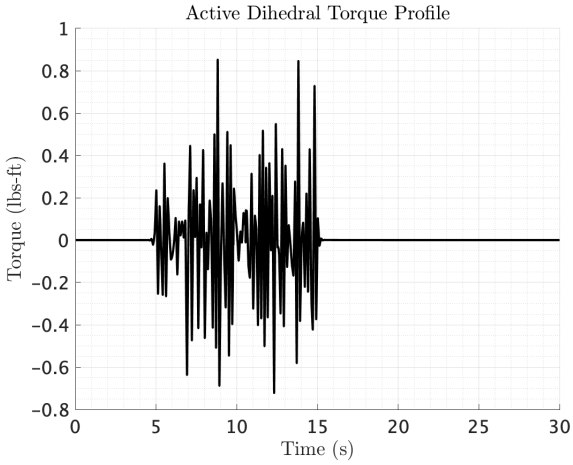

(b) Input torque (δ_τ)

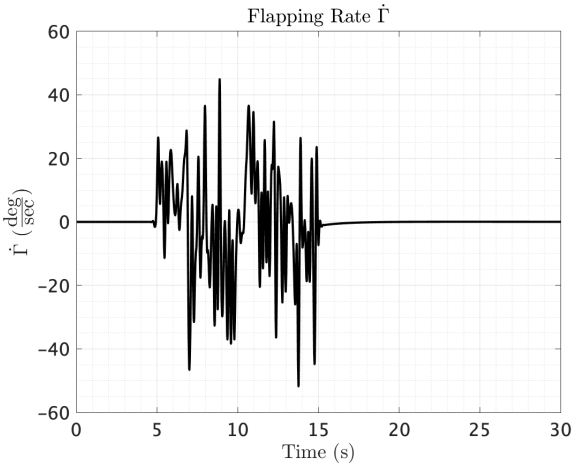

(c) Flapping rate ($\dot{\Gamma}$)

Figure 6.18: Active dihedral system rejecting continuous turbulent gust disturbance

6.7 Large Discrete Gust Rejection

The previous cases highlight the performance of the active dihedral system with respect to typical gust patterns UAS encounter operating at lower altitudes, but the question arises of system performance in extreme gust conditions. A large 1-cosine gust was generated and tested against the elevator only and active dihedral system; the wind gust depicted in Figure 6.19 is a 100ft gust gradient disturbance with a four times multiplier, creating a peak amplitude of $16.2\frac{\text{ft}}{\text{s}}$.

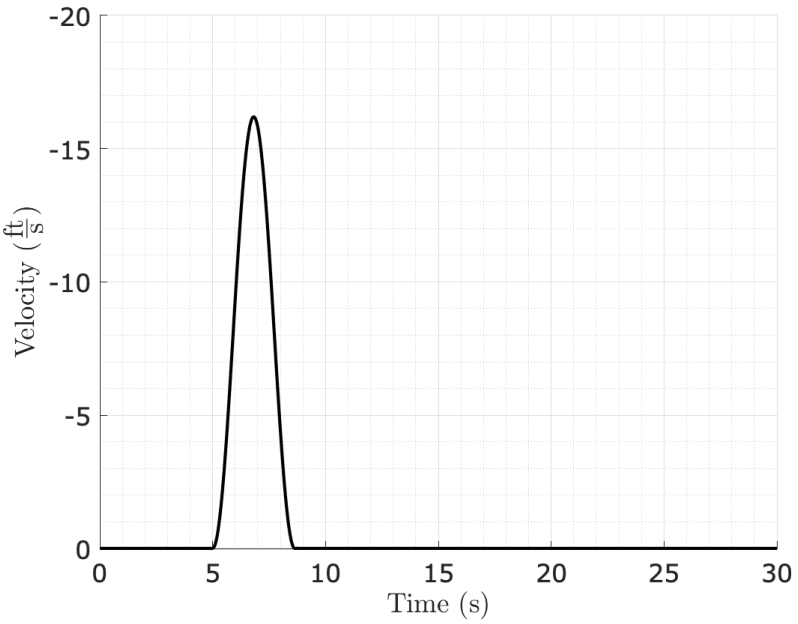

Figure 6.19: Amplified 1-cosine gust profile to increase vehicle perturbation

The controllers designed for the elevator only and active dihedral systems were developed independently and weighted such the best feasible controller was designed for rejecting this disturbance; this notion was proposed to eliminate any discrepancy in the active dihedral system performing better due to weightings variance in the Q and R penalty matrices. Figure 6.20 shows the response of both controllers to the large disturbance. The active dihedral system outperforms the elevator controller, reaching a maximum vertical position

deviation from the equilibrium trajectory of 0.32ft, which was a 45% reduction compared to the elevator performance. The active dihedral system allowed a maximum vertical velocity of $0.278\frac{\text{ft}}{\text{s}}$, also being a 45% reduction in deviation compared to the elevator controller. The reduction in perturbation is denoted in Figures 6.20a and 6.20b.

Similar to the general case previously shown, there is a significant decrease in ground speed due to the use of active dihedral, seen in Figure 6.20d. Notice how the active dihedral system begins pitching upward, indicating an increase in the angle of attack in Figure 6.14e, and hence drag, leading to the decreased ground speed. Opposingly, the elevator controller is constrained to pitching downward to decrease the lift generated. The magnitude of acceleration experienced by the vehicle was larger for the active dihedral system compared to the elevator controller. Differing from the general simulations, the total acceleration of the active dihedral system peaks at $0.0188\frac{\text{ft}}{\text{s}^2}$, being a 25% increase from that of the elevator controller. The contributing factor to increased acceleration for the active dihedral system is the deceleration experienced along the x^E axis. The total acceleration was again marginal in terms of g rating.

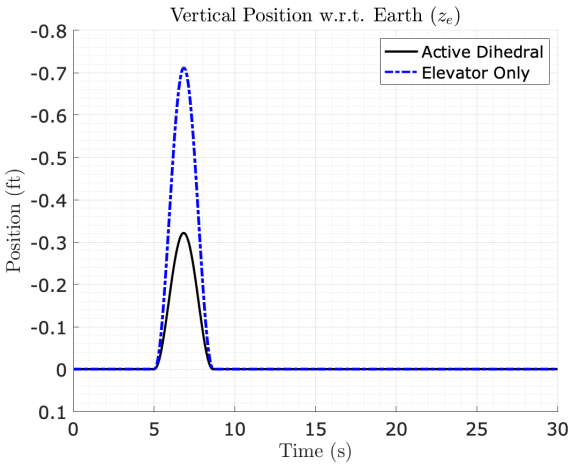

(a) Vertical position (z_e)

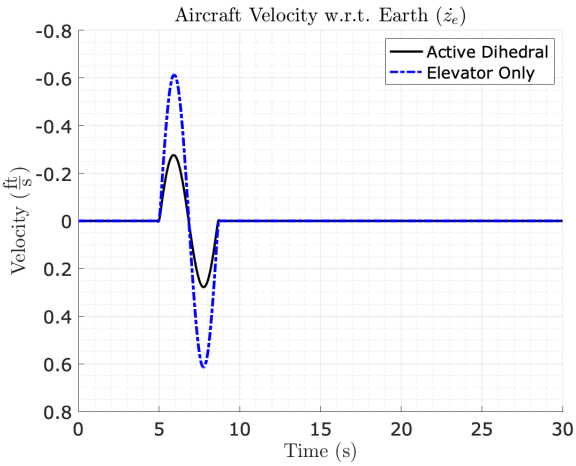

(b) Vertical velocity ($\dot{z}_e$)

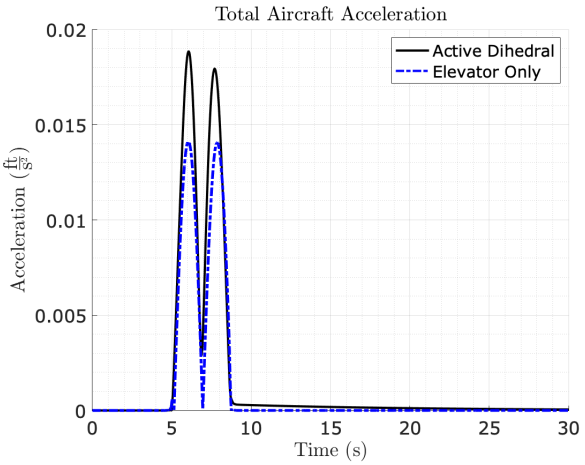

(c) Total vehicle acceleration

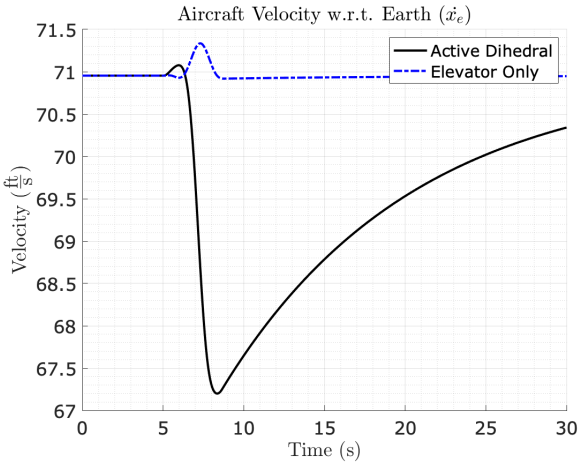

(d) Ground speed ($\dot{x}_e$)

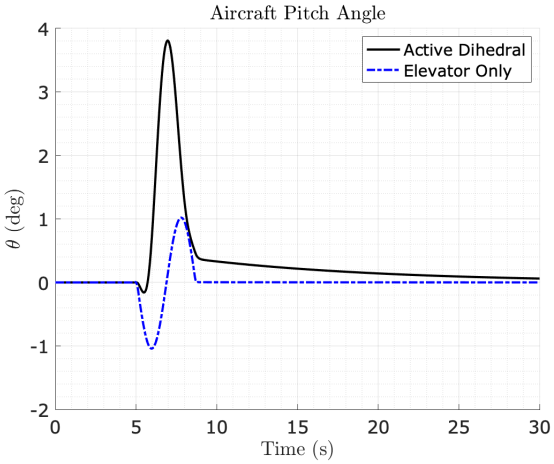

(e) Pitch angle (θ)

Figure 6.20: Amplified 1-cosine disturbance applied to the elevator controller and active dihedral controller

6.8 Variable Gust Gradient Rejection

The FAA 14 CFR Part 25.341.1 indicates that aircraft are to be evaluated for stability and gust rejection performance with the variation of gust gradient, H, from 30ft to 350ft. An investigation of the two controller's performance against the sequence of wind gust gradients was completed. Figure 6.21 shows how the 1-cosine gust profile varies with change in gust gradient, H, ranging from 30ft to 350ft in increments of 50ft starting at 50ft.

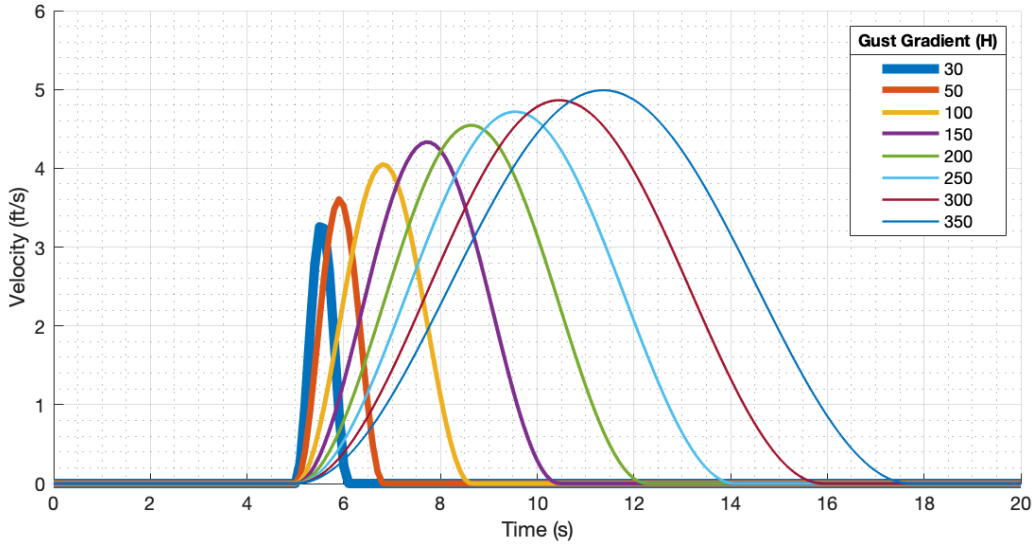

Figure 6.21: 1-cosine wind gust profile variation with change in gust gradient length

The gust profiles generated were created from the formulations provided in Equations (3.99) and (3.100), using a reference velocity, U_{ref}, of $5\frac{\text{ft}}{\text{s}}$ and flight profile alleviation factor, F_g, equal to 1 due to assumed low altitude flight. Figure 6.21 shows that with an increase in gust gradient also comes an increase in maximum gust velocity and an increase in half-cycle period, meaning the aircraft would encounter a larger total wind gust but have an increased period of time to counter the wind gust. A gust gradient of 30ft induced an impulsive type gust perturbation, with a half-cycle period of one second. The elevator and active dihedral control systems were posed against the sequence of gust gradient profiles using the $\Gamma = 5°$

and $y_{b_\Gamma} = 0$ configuration. The position, velocity, acceleration, and ground speed for the vehicle with an elevator only controller subjected to the gust gradients are shown in Figure 6.22.

It is observed in Figure 6.22a that the gust rejection capability of the elevator keeps the aircraft within 0.235ft of its trajectory with the maximum perturbation existing at the maximum gust gradient of 350ft. With increasing gust gradient exists an increased total net wind velocity perturbation, but this does not directly translate to the vertical velocity experienced by the vehicle. Figure 6.22b indicates the vertical velocity of the aircraft is reduced with an increased half-cycle period associated with the larger gust gradient. The maximum vertical velocity experienced by the vehicle is $0.44\frac{\text{ft}}{\text{s}}$, with this occurring at the lowest gust gradient of 30ft, indicating the aircraft is experiencing more of an impulsive disturbance, with the vehicle and LQR controller having a shorter period of time to respond to the perturbation. Corresponding to this behavior with the small gust gradient, the maximum total aircraft acceleration experienced by the vehicle is $0.013\frac{\text{ft}}{\text{s}^2}$, shown in Figure 6.22c, with this occurring primarily in the vertical direction, as Figure 6.22d shows a small change in magnitude of longitudinal speed.

Figure 6.23 depicts the response of the active dihedral model to the gust gradients. The response of the aircraft showed a decreased deviation in vertical trajectory compared to the elevator controller, with a maximum vertical perturbation of 0.024ft occurring at the largest gust gradient. Similar to the elevator only LQR controller, the maximum vertical velocity of $0.046\frac{\text{ft}}{\text{s}}$ occurs at the smallest gust gradient, due to the aircraft having a short period of time to respond to the perturbation. These measured values for vertical position and velocity are a magnitude smaller than the total aircraft perturbation experienced with the LQR controller. The maximum total aircraft acceleration experienced by the vehicle was $0.011\frac{\text{ft}}{\text{s}^2}$ at the gust gradient of 30ft, again being an indication of the impulsive type

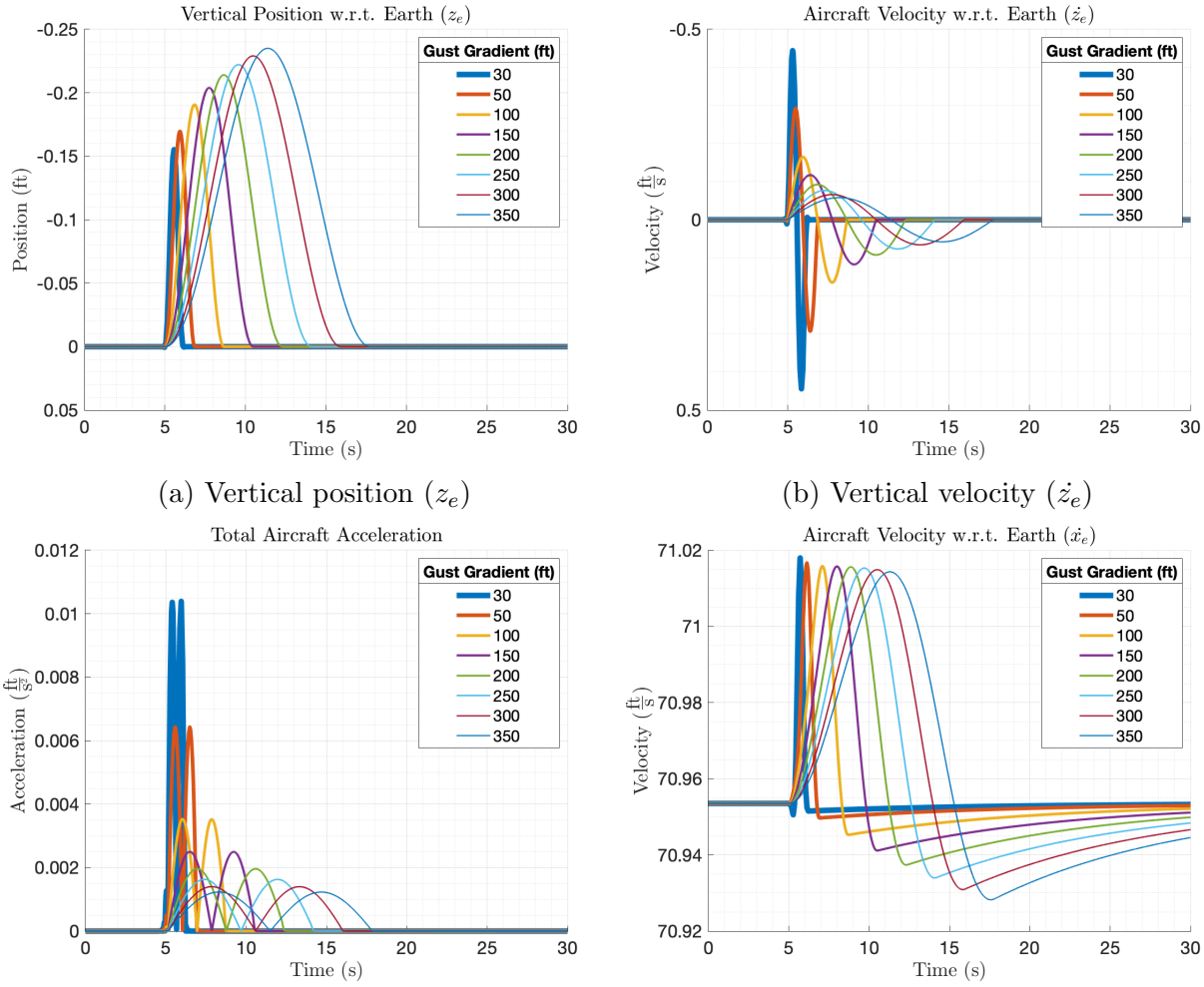

(a) Vertical position (z_e)

(b) Vertical velocity ($\dot{z}_e$)

(c) Total vehicle acceleration

(d) Ground speed ($\dot{x}_e$)

Figure 6.22: Elevator controller response, subjected to gust gradients ranging from 30ft to 350ft

disturbance. Of note is the maximum reduction in ground speed, $\dot{x}_e$, of $2.12\frac{\text{ft}}{\text{s}}$, occurring with the largest wind gust gradient. This decrease in ground speed significantly differed from the response of the elevator. The dihedral angle variation with gust gradient, shown in Figure 6.24a, shows a maximum dihedral deflection from the equilibrium of 26.15° corresponding to the 350ft gust gradient, with the controller attempting to reduce the lift generated due to the increased angle of attack.

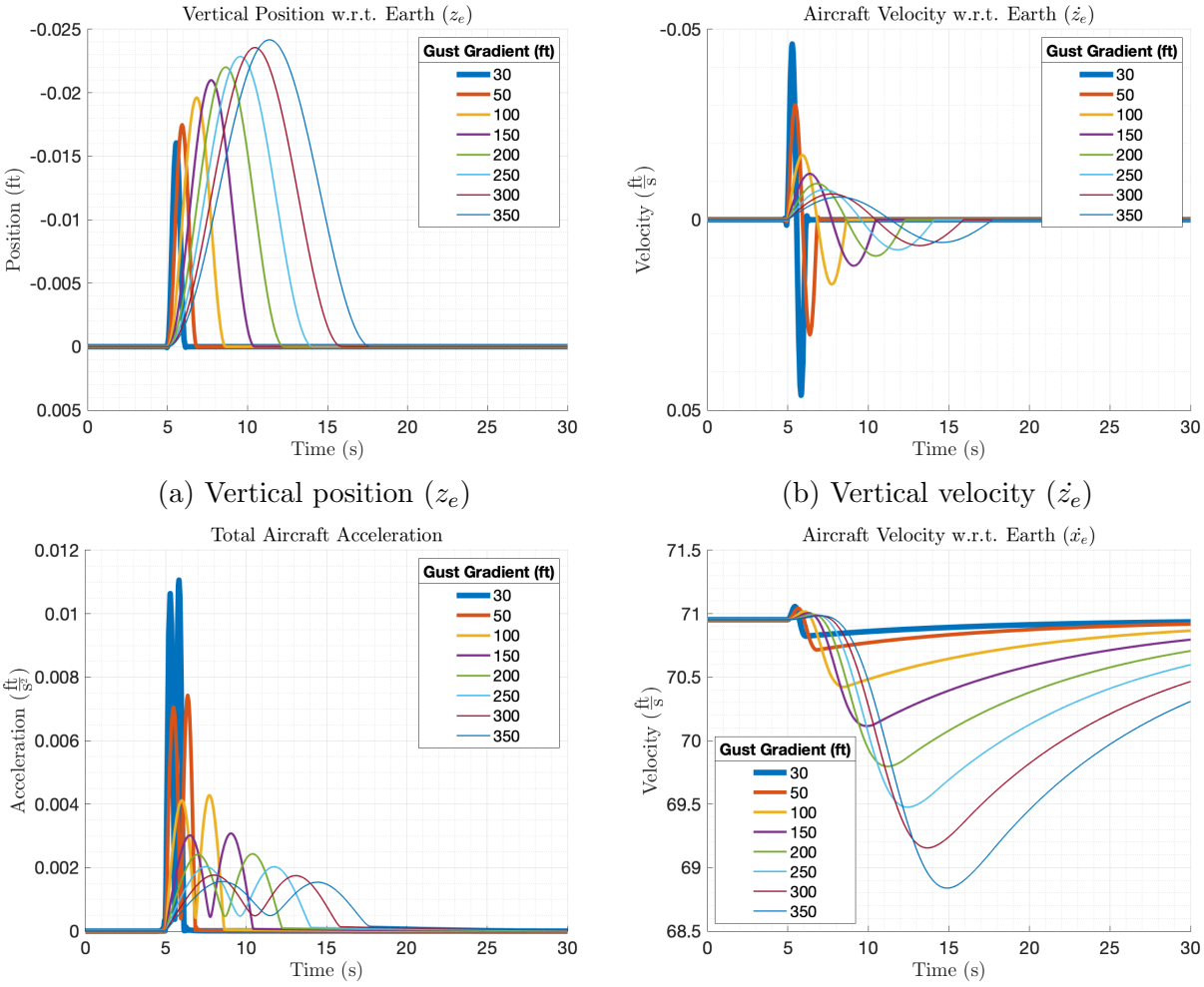

(a) Vertical position (z_e)

(b) Vertical velocity ($\dot{z}_e$)

(c) Total vehicle acceleration

(d) Ground speed ($\dot{x}_e$)

Figure 6.23: Active dihedral controller response, subjected to gust gradients ranging from 30ft to 350ft

Attention must be drawn to this decrease in ground speed and the acceleration equivalency between the two controllers. Comparing Figures 6.22c and 6.23c, it is easy to see the experienced acceleration between the two controllers was approximately equivalent, hence the question arises of where the energy is expended in the active dihedral case. It appears the system with the dihedral controller acts in a manner to realize the deceleration in $\dot{u}$ instead of $\dot{w}$, maintaining the desired trajectory. Of note is the response of the LPV to a change in $\dot{\Gamma}$, as seen previously in Figure 6.10a, with a positive $\dot{\Gamma}$ leading to a decrease in

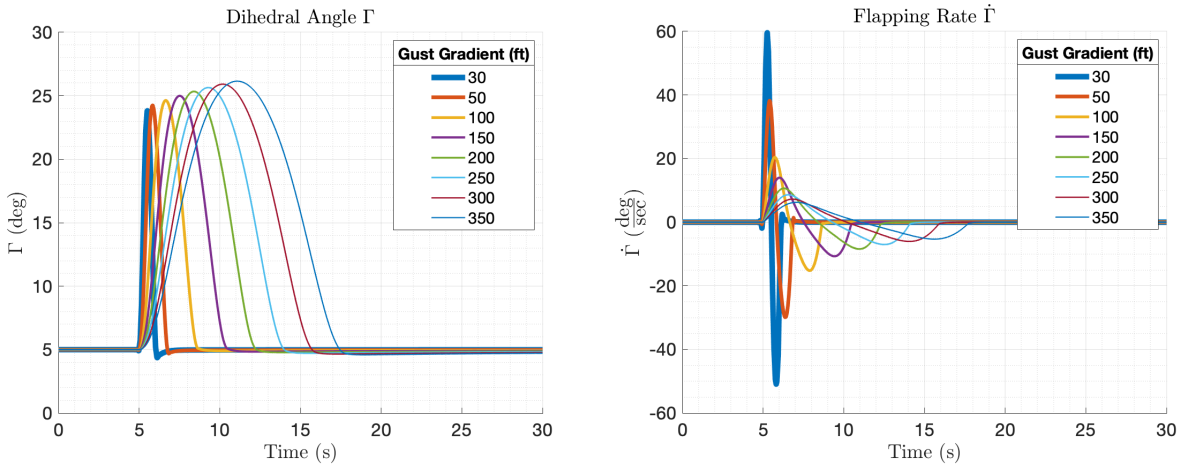

(a) Dihedral angle (Γ) (b) Flapping rate ($\dot{\Gamma}$)

Figure 6.24: Change in Γ and $\dot{\Gamma}$ using the active dihedral controller in response to variation of gust gradients from 30ft to 350ft

the change in $\dot{u}$; this effect directly impacts the results observed in Figures 6.23d and 6.24b.

To characterize the response of the controllers independent of the peak amplitude associated with variation in gust gradient, the normalized change in altitude due to the perturbation is plotted in Figure 6.25. These plots show the expected response of the vehicle controllers to a 1-cosine gust with unit peak amplitude, showing that one can expect a change in altitude of -0.047ft and -0.004ft for the elevator only LQR controller and the active dihedral controller, respectively, per unit peak amplitude of a normally distributed positive 1-cosine gust disturbance. The linear relation between the disturbance and aircraft response should be expected due to the use of a single LQR controller, whose feedback also scales linearly with system deviation from equilibrium.

The question may arise as to the validity of the posed controllers and the true equivalence of comparison, hence requiring an explanation of the controller design and assumptions. The LQR controller was designed such that the same state cost matrix, Q, was used for all gusts gradients, with no penalty associated to use of the elevator. Adding exponential cost

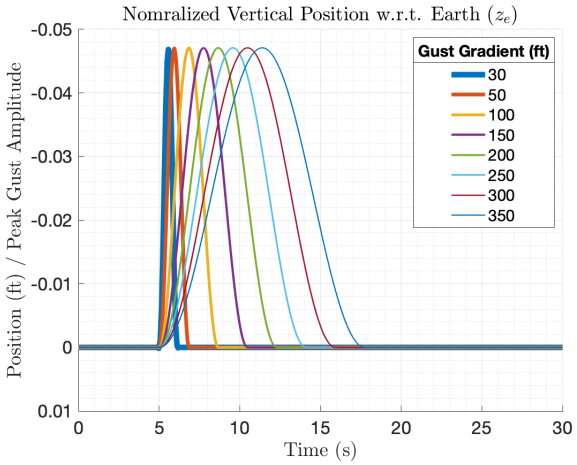

(a) Elevator controller normalized vertical position ($\frac{z_e}{H}$)

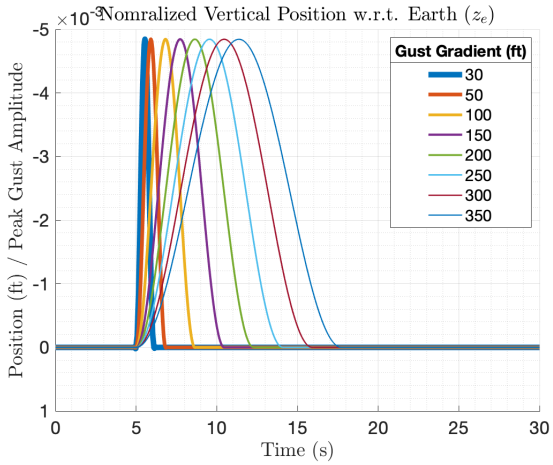

(b) Active dihedral controller normalized vertical position ($\frac{z_e}{H}$)

Figure 6.25: Vertical position response of elevator and active dihedral controllers, normalized with gust gradient

to the states z and w eventually resulted in system having no improvement in performance, and hence this was used to drive the quantification of the best available controller. Similarly, for the active dihedral controller, the Q matrix was held constant for all gust gradients. The penalty associated with the z and w states defined for the active dihedral LQR controller were increased until instability was observed with some gust gradients. Once the z and w penalties were identified, they were held constant in the Q matrix, however, there was an additional penalty assigned to Γ to ensure the system returned to equilibrium. It was found that if no penalty is assigned to Γ, the system typically returned the dihedral angle to $\Gamma = 0°$. Both control systems at hand restricted the elevator to actuate between $\pm 30°$ and the active dihedral controller limits actuation to $0° <= \Gamma <= 60°$, maintain the constraints previously described in Section 6.5.

6.9 Gust Rejection with Varied Dihedral Breakpoint

It was of interest to investigate the available authority associated with a given feedback controller, and how this authority changes with respect to dihedral breakpoint location. There also exists a trade-space in terms of the cost required to actuate the system, in which the cost assessment method based on the total capacity requirement previously defined in Section 4.3 was used for evaluation. Simulations against a 1-cosine gust and continuous turbulent gust were used to assess the performance capability of each configuration, with a comparison made to the elevator only controller performance under the identical gust pattern. The grid of configurations evaluated is listed in Table 6.2.

Defining a metric of comparison for this analysis, Figure 6.26 depicts the definition Δz_e, and empirically shows the difference between the active dihedral controller performance versus the elevator only controller. A negative Δz_e indicates the elevator only controller mitigated the perturbed vertical position of the vehicle better than the active dihedral system, and conversely, a positive Δz_e indicates better performance of the active dihedral controller. Figure 6.26 shows for a 1-cosine gust how a performance distinction was made between the two controllers.

A single 1-cosine gust with a gust gradient of 100ft was used to perturb the system to exhibit the feedback controllers response to a discrete wind gust; Figure 6.21 shows the gust profile corresponding to a 100ft gust gradient. The following set of results for the discrete disturbance assumes a fixed set of LQR controller state and input weights, given by the Q and R matrix, in which the gains were determined for each configuration. There did exist instances in which the state gains were reduced to prevent the feedback controller from destabilizing the vehicle and its response, as previously discussed in Section 6.5. These instances of instability occurred only at large values of y_{b_Γ}, and therefore the state penalty

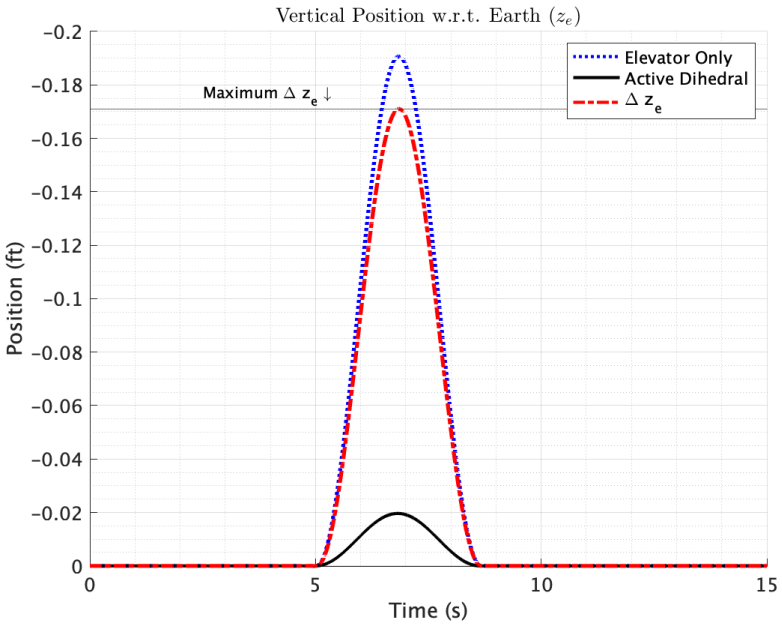

Figure 6.26: Definition of Δz_e between controllers for use in performance assessment

was reduced minimally but sufficiently to stabilize the vehicle's response.

Figure 6.27 shows a set of surface plots to visualize the variation in the vehicle configuration responses to the discrete disturbance. The total Δz_e encountered by each configuration is depicted in Figure 6.27a. The best configuration in terms of greatest Δz_e was with $y_{b_\Gamma} = 0$; this was as expected because the total gust rejection authority should be maximum with the breakpoint at the root and decrease as y_{b_Γ} increases. It is seen that $y_{b_\Gamma} = 25\%$ performs similar to the breakpoint located at the root, with only a slight decrease in vertical position. Contrasting, at $y_{b_\Gamma} = 50\%$, there is a large decrease in gust rejection performance. In all cases, the larger initial dihedral angle has slightly reduced performance than the lower initial dihedral angles, and therefore the larger dihedral angles should be considered as a trade-space for C_{l_β} as y_{b_Γ} increases. Notice that for $y_{b_\Gamma} = 75\%$, the active dihedral controller performs worse than the elevator controller; the controller is attempting to dump lift through the active dihedral controller and is unable to because only 19% of the vehicle lift is

being generated in the outboard portion of the wing. The occurrences of this negative Δz_e propagated into other results. The evaluation of $\Delta \dot{z}_e$, given in Figure 6.27b, was completed similarly to that of Δz_e. The trends in performance described for Δz_e were likewise observed in $\Delta \dot{z}_e$ for all configurations.

Figure 6.27c shows the total battery consumption due to active dihedral, expressed in mAh. The battery consumption is largest for the smaller breakpoints and smaller dihedral angles, as the wings are being used more heavily to reject the wing gust and are encountering more torque than the other configurations. A sample post-processed plot of current required to actuate the system is located in Appendix A. A comparison to mission time lost can be made if one were to assess the total battery capacity on board and expected flight time from the battery; the impeded time estimate will scale directly with the battery consumption plot shown here. Using Figure 6.27c it is also possible to estimate the total number of wind gusts the system can reject given a pre-defined battery capacity. In an attempt to find the best active dihedral controller in terms of gust rejection capability versus total battery consumption, Δz_e was normalized with respect to total battery consumption and plotted in Figure 6.25. This plot shows how much gust rejection authority the aircraft has at the cost of a battery, giving a means of measuring gust rejection efficiency. The configurations with $y_{b_\Gamma} = 0$ or $y_{b_\Gamma} = 25\%$ proved most efficient in terms of rejecting a 1-cosine gust, with larger values of Γ being the slightly more efficient than lower ones which were unexpected.

Further investigation of why the performance of higher values of y_{b_Γ} exhibited deteriorated performance compared to the other configurations was completed. An alternative means to evaluate the system cost was to compare the state penalty of the Q matrix, described in Section 4.3.2, and observe which controller best minimized the state component of the cost function. Figure 6.28a shows the state cost difference between the active dihedral controller and the elevator controller. The cost difference is evaluated as the elevator con-

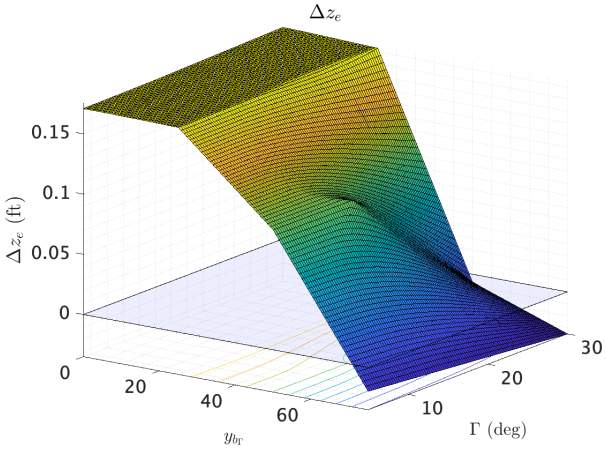

(a) Δz_e

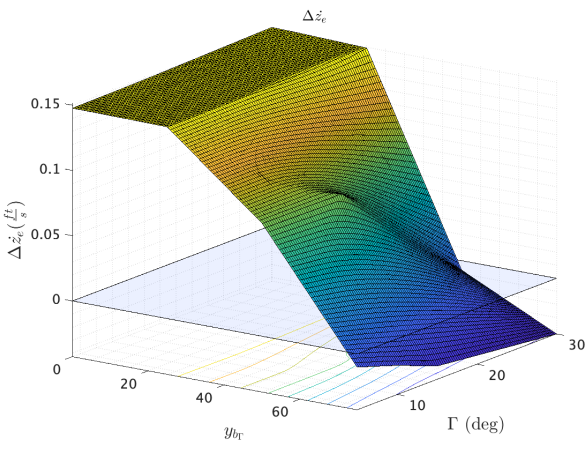

(b) $\Delta \dot{z}_e$

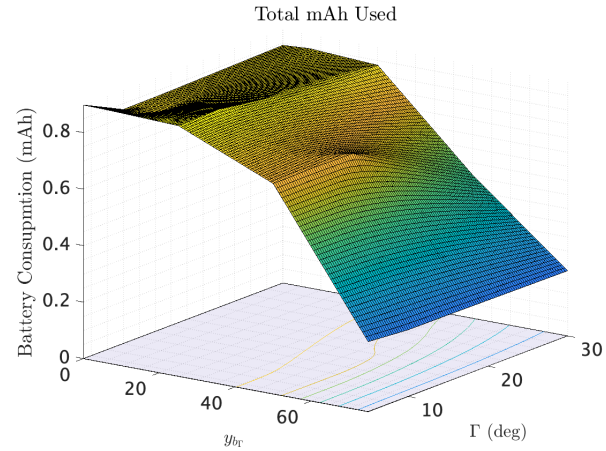

(c) Battery consumption (mAh)

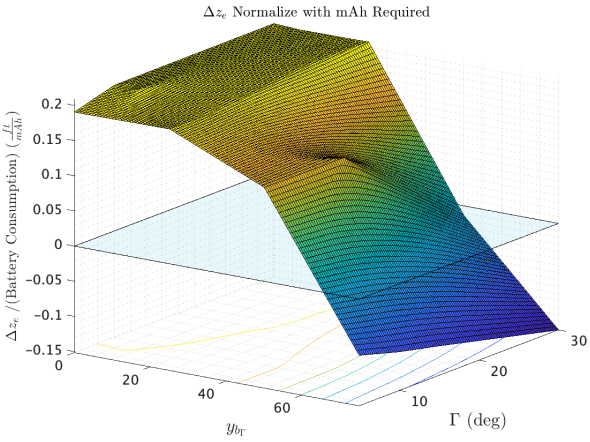

(d) Δz_e normalized with respect to battery consumption

Figure 6.27: Vertical gust rejection performance and cost assessment of active dihedral controller compared to elevator controller, for a discrete 1-cosine gust disturbance

troller cost, less the active dihedral cost; positive ΔJ_Q indicates the improved performance of the active dihedral system. Compared to previous evaluation of Δz_e and $\Delta \dot{z}_e$, the ΔJ_Q trended similarly for all dihedral angles and breakpoints. The breakpoints further outboard did not perform well compared to the vehicle using only the elevator, which was unexpected.

It must be understood what penalties are assigned to the Q matrix to comprehend how this result is obtained. Penalties are assigned to z, u, w, θ, and Γ, with cost assigned

to Γ to ensure the system returns to the equilibrium dihedral angle. The penalty given to u and θ was completed in an attempt to reduce the total acceleration the aircraft is experiencing, and associated pitching, such that the active dihedral system would not rotate the vehicle to reject gusts in z and w; the elevator employs this method to reject gusts. The Q matrix was held constant for all configurations through evaluation of Equation (4.2) to prevent variations in penalty from skewing the results; recall Q was reduced minimally for larger y_{b_Γ} configurations for the solution to converge. It was expected that breakpoints further outboard would significantly reduce the observed change in u, seen comparably in plots of ground speed like Figure 6.23d, while still giving some gust rejection authority, but this was not the case. Figure 6.28a shows breakpoints at the root successfully reduced the cost associated with all the penalized parameters, with $y_{b_\Gamma} = 0$ and $\Gamma = 30°$ being the most efficient, reflected in Figure 6.28, similar to the Δz_e evaluation.

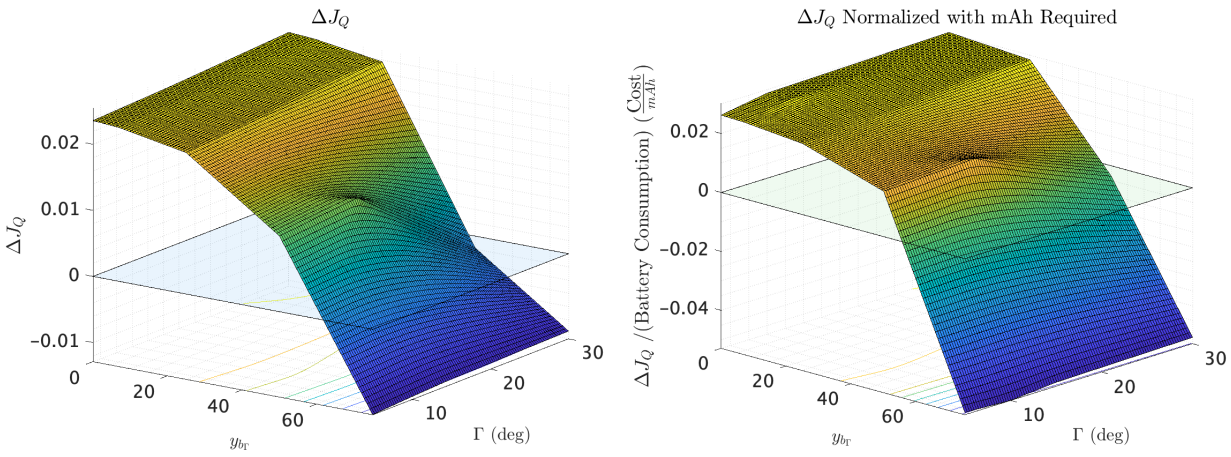

(a) ΔJ_Q (b) ΔJ_Q normalized with battery consumption

Figure 6.28: State cost, J_Q, reduction and assessment for the active dihedral controller compared to elevator controller, for a discrete 1-cosine gust disturbance

6.10 Gain Scheduled Controller

There may exist a case in which higher performance is desired from the LQR controller in terms of gust rejection compared to the results in Section 6.8. It was found that in using the LQR controller, there was frequently a challenge in obtaining higher gust rejection performance without the dihedral angle settling to a non-equilibrium state (i.e. $\Gamma = 0°$). This phenomenon likely occurred due to the state weights of z and w significantly outweighing the state cost of Γ returning to is the nominal value. In an attempt to obtain greater gust rejection performance, a mixed gain scheduling feedback controller was built and evaluated for the single configuration of $\Gamma = 5°$ and $y_{b_\Gamma} = 0$.

Three independent controllers were evaluated based on the desire to meet increased performance requirements against a wind gust disturbance with a gust gradient of 100ft. The first controller was the traditional constant LQR controller that has been used through previous simulations discussed in this study, with the state penalties in the Q matrix increased to heavily weight deviation in position and velocity. In order for the controller to use active dihedral to its advantage and truly improve performance, the associated penalty with the dihedral state was reduced such that the controller would actuate to higher dihedral angles.

The second controller developed was a gain scheduled controller, in which the same state and input cost matrices, Q and R respectively, were used in the development of the gain scheduled controller. This gain scheduled controller was employed to work in tandem with the variation of the LPV system, such that at higher dihedral angles, the resultant feedback would be an increase in elevator input would occur through the associated gains. Subsequently, if the case in which throttle was being incorporated in the feedback controller, this also would also have an increased set of gains. The gain scheduled controller uses interpolation between the gridded operating gains to reduce the impacts of switching. The

structure of this controller was previously described in Section 5.2.2.

The third controller developed was a mixed gain scheduled controller. This controller was a convolution of a constant LQR controller and the gain scheduled controller. This controller takes the form of that described in Section 5.2.3. The gain scheduled portion of the controller, $K(\Gamma)$, remains fixed with the high-performance gains as used in the second controller observed in this example. The LQR gain, K_{LQR}, in the controller was created to significantly weight a state deviation in Γ, such that when no disturbance greater than $|\vec{w}|_{\max}$ exists, the vehicle would attempt to return to its equilibrium state. A value of $0.1\frac{\text{ft}}{\text{s}}$ was assumed for $|\vec{w}|_{\max}$ and it is acknowledge that alternative values could be selected in the future with variation in performance.

Figure 6.29 depicts the response of the three controllers to a single 1-cosine gust with a gust gradient of 100ft. As expected, the traditional LQR controller responded well to performance-biased weights, with the aircraft maintaining its vertical trajectory within 5.9e-04ft and its vertical velocity being a maximum of 5.1e-4$\frac{\text{ft}}{\text{s}}$. Noticeably, due to the aggressive weighting to the trajectory, the dihedral angle settles to $\Gamma = 0°$, shown in Figure 6.29c, not the equilibrium state of $\Gamma = 5°$. This response occurred because the state cost associated with remaining at the non-equilibrium dihedral angle was of lower cost compared to the z and w state changes associated with actuating back to the equilibrium dihedral.

Opposingly, the gain scheduled controller using the state weights does return the system to the equilibrium dihedral state but at the cost of performance. In general, the gain scheduled controller performed well in terms of the general gust rejection problem, however, with respect to higher performance it reaches a maximum vertical position of 0.029 ft and a velocity of $0.026\frac{\text{ft}}{\text{s}}$ which is a magnitude larger than the LQR controller. Around 8 seconds into the simulation, as the 1-cosine gust is subsiding, the controller begins to oscillate due to inputs to the system, indicated in Figure 6.30, with the elevator and torque

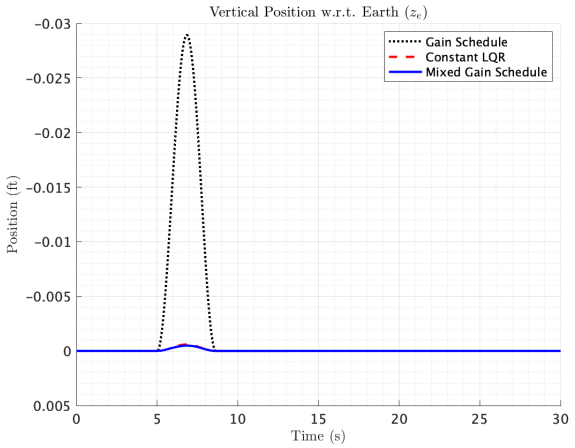

(a) Vertical position (z_e)

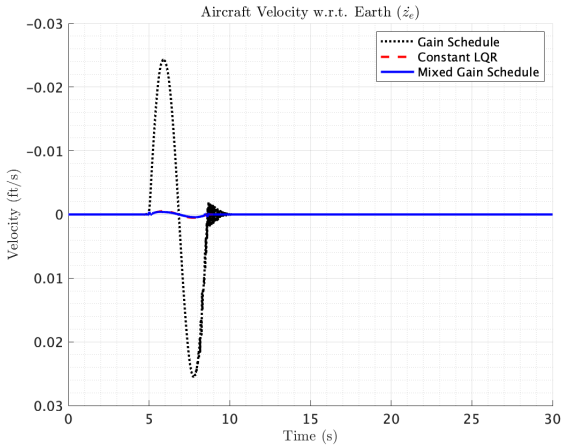

(b) Vertical velocity ($\dot{z}_e$)

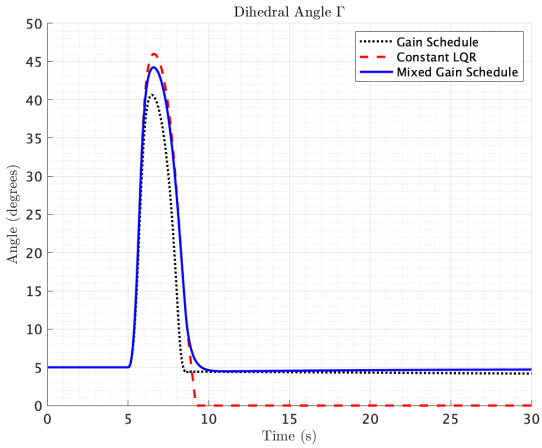

(c) Dihedral angle (Γ)

Figure 6.29: Performance comparison of the constant LQR, classical gain schedule, and the mixed gain scheduled controller schemes against a 1-cosine disturbance with gust gradient of 100ft

input beginning to rapidly deflect. The primary contributor to the vertical perturbations seen in Figure 6.29b was a resultant of the direct lift obtained from flapping the wings through variation in δ_τ. The traditional gain scheduling method assumes the aircraft is operating intentionally, and attempting to remain, at the operating dihedral angle, typically for purposes of desired lateral-directional stability; the gain matrix K being scheduled is evaluated about the equilibrium state $A(\Gamma, 0)_{\text{eq}}$ for a given y_{b_Γ}. This type of scheduling was

expected to give a greater performance at off equilibrium values of Γ. The incurred chatter on the system is not fully understood but could be contributed to the linear interpolation occurring in the gridded set of gains. It is however known that the LPV model of the system is not solely causing this oscillatory response as the traditional LQR controller uses the same LPV model.

The mixed gain scheduled controller provides the benefits of the LQR controller, obtaining the higher desired performance, but also meet returns the vehicle to its equilibrium state as does the gain schedule controller. The maximum absolute vertical perturbation is 4.9e-4ft with the vertical velocity remaining tightly controlled, reaching a maximum of absolute deviation of 4.0e-4$\frac{\text{ft}}{\text{s}}$. Figure 6.30a shows what appeared to be transients at the point of transition through $|\vec{w}|_{\max}$. Acknowledging that the system would be transitioning between controllers with alternative weights for variation in goal, the purpose of the linear ramp, described in Section 5.2.3, was to reduce the impacts of sharp variations in the feedback gain. It is expected that this controller would perform well with constant wind gusts, such as a near-constant upward wing gust, providing the proper controller feedback at an alternative dihedral angle that must be maintained. The results presented show that there exist some negative impacts with this gain scheduling method with respect to the 1-cosine gust, but it did perform the best in terms of an aggressive feedback controller. Further investigation and design into the proper gain scheduling method for this application could be conducted.

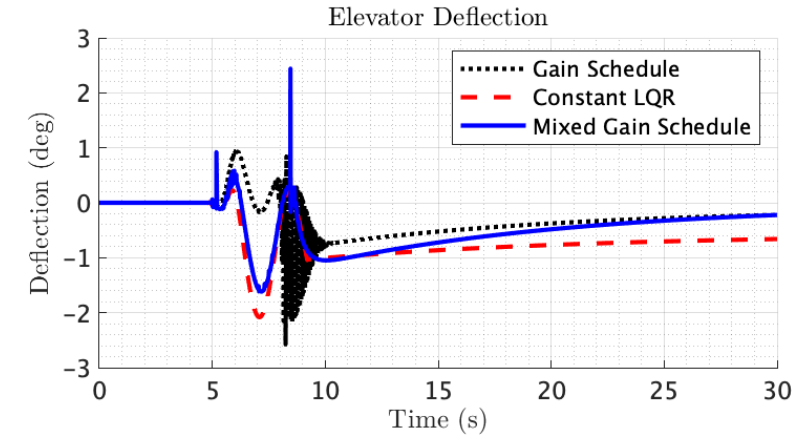

(a) Elevator input (δ_e)

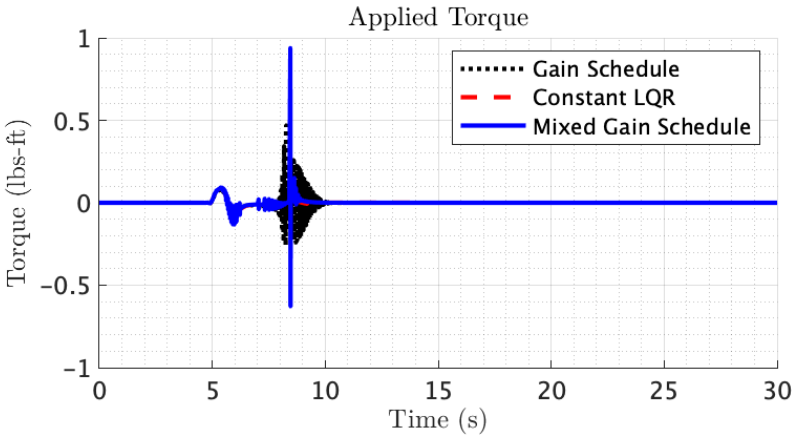

(b) Input torque (δ_τ)

Figure 6.30: System input comparison of the constant LQR, classical gain schedule, and the mixed gain scheduled controller schemes against a 1-cosine disturbance with gust gradient of 100ft

Chapter 7

Conclusions and Future Work

An active dihedral system was successfully modeled and simulated on a fixed-wing UAS as proof of concept for vertical gust rejection. The active dihedral system was modeled using an LPV model, improving the model accuracy such that the nonlinear system can be better approximated compared to a traditional LTI system. Gain scheduling was applied to the system, which highlighted the need for a mixed feedback controller which prioritizes vertical gust rejection during perturbations, and lateral-direction stability upon rejection of the gust. The active dihedral system design was based on previously identified parameters such as flapping rates, torque requirements, and battery consumption, bridging the gap between physical implementation and theoretical predictions.

Small angle approximations were used for modeling both the dihedral effect and flapping effect. Future implementations of this model should be modified to reflect the trigonometric relationship encapsulate by these effects, as the LPV system is being resolved locally about each dihedral point; this likely induced unnecessary error in the model at higher dihedral angles. Additional modeling is required to reflect the forces and moments the active dihedral actuator is encountering, with the purpose of improving model accuracy in terms of applied torque. The true torque requirements were enforced in simulation post-processing, giving accurate cost assessment. Limitations should also be put in place to remove the application of torque from the system once the active dihedral system has reached its upper or lower bounds, being analogous to a real actuating system.

The LPV model was designed such that the dihedral angle (Γ) and flapping rate ($\dot{\Gamma}$) were the parameter-dependent variables changing with time, in order to capture the dynamics associated with both the dihedral effect and flapping effect. Linear interpolation was used in between the finite set of discretized operating points to prevent chattering effects common with switched systems. Through the assessment of Lyapunov stability applied to switched systems, it was possible to identify a restricted operating range for which various configurations could operate and be locally exponentially stable. While acknowledged that stability for parameter-dependent switched systems is subject to limits on parameter rate of change, a computed restriction was not applied to the rate of change of flapping ($\ddot{\Gamma}$), which would have constrained input torque. It was shown that Γ and $\dot{\Gamma}$ restrictions, which vary based on the equilibrium configuration, must be imposed to improve the conservativeness of the system's exponential stability assessment. The Γ and $\dot{\Gamma}$ restrictions were maintained in the simulations presented in this study, with the exception of letting $\Gamma = 0°$, however, no inherent vehicle instability resulted when marginally exceeding the Γ and $\dot{\Gamma}$ restrictions.

Alternative methods for gain scheduling should be investigated, with the gain scheduled controller being built for a single selected configuration and equilibrium with a variation in operating points. The controller should be designed to return the vehicle to the equilibrium dihedral angle but continue prioritization of gust rejection in the presence of a disturbance. The approach used consisted of gains scheduled about a varying set of linearized vehicle equilibrium operating points, which worked sufficiently but not well, as adverse effects were observed in the controller due to conflicting goals of the gain schedule.

The active dihedral system was successfully tested against both discrete and continuous gust disturbances, with a comparison of its gust rejection capability to traditional control surface use. The results showed improvement in the aircraft's ability to mitigate vertical perturbation on a given flight trajectory through a reduction in vertical velocity, with minimal

increase in total aircraft loading. Gust alleviation was not obtained with the active dihedral system, as the controllers were not designed to mitigate total acceleration experienced by the vehicle. A bi-product of using active dihedral was a reduction in directional airspeed due to increased angle of attack when actuating, contributing to a lack of gust alleviation. The system was also tested against a variation of 1-cosine gust disturbances, in which the response scaled directly with the peak magnitude and gust length due to the linear feedback from the LQR controller.

A variation in dihedral breakpoint was modeled and simulated successfully. Dihedral breakpoints closer to the root provided more gust rejection bandwidth, reducing the magnitude of perturbation from equilibrium. Breakpoints further outboard from the root proved to be less effective at rejecting disturbance in terms of vertical displacement and were ineffective at minimizing the state cost function. With respect to battery consumption, larger initial dihedral angles with the breakpoint at the root proved to be most efficient. It was shown that equivalent values of C_{l_β} can be obtained using higher dihedral angles with a breakpoint further outboard, helping maintain lateral-directional stability and roll stiffness. All modeled active dihedral configurations met or exceeded the MIL-F-8785C dynamic stability requirements, giving the expectation of nominal handling qualities on a human-piloted system. There remains an opportunity for additional trade-space exploration to identify an optimal breakpoint location, though it is expected torque requirements will drive most breakpoint selections.

Observing the vertical gust rejection benefits and variable lateral-directional stability qualities, current applications of the active dihedral system show compelling reason to continue the pursuit of modeling and experimental testing of such a system. The active dihedral system presents a rich, multi-disciplinary, problem with concentrations of mechanics, structures, aerodynamics, dynamics, and control, all requiring some level of investigation for

such a concept. There exists significant scope for additional investigation in both theory and experimental validation of the active dihedral concept. This study concentrated mainly on the dynamics and control discipline, highlighting the process of modeling a variable dihedral system through the appropriate LPV schema. The overall modeling and simulation of the active dihedral system applied to fixed-wing UAS proved advantageous to rejecting vertical gust disturbances, showing promising real-world benefits when incorporated with purposeful lateral-directional stability scheduling for lateral gust disturbance rejection.

Bibliography

[1] Bernard Etkin. *Dynamics of Atmospheric Flight*. Second Edition. Dover, 2000.

[2] D. R. Warrick. "Bird Maneuvering Flight: Blurred Bodies, Clear Heads". In: *Integrative and Comparative Biology* 42.1 (Feb. 2002), pp. 141–148. DOI: 10.1093/icb/42.1.141. URL: https://doi.org/10.1093/icb/42.1.141.

[3] Aditya A Paranjape, Soon-Jo Chung, and Michael S Selig. "Flight mechanics of a tailless articulated wing aircraft". en. In: *Bioinspir. Biomim.* 6.2 (June 2011), p. 026005.

[4] Gottfried Sachs and Florian Holzapfel. "Flight Mechanic and Aerodynamic Aspects of Extremely Large Dihedral in Birds". In: *45th AIAA Aerospace Sciences Meeting and Exhibit*. American Institute of Aeronautics and Astronautics, Jan. 2007. DOI: 10.2514/6.2007-46. URL: https://doi.org/10.2514/6.2007-46.

[5] David A Caughey. *Lecture Notes in Dynamical Equations for Flight Vehicles*. Cornell University, 2011.

[6] Louis V. Schmidt. "Aerodynamic Principles". In: *Introduction to Aircraft Flight Dynamics*. American Institute of Aeronautics and Astronautics, Jan. 1998, pp. 15–65. DOI: 10.2514/5.9781600862052.0015.0065. URL: https://doi.org/10.2514/5.9781600862052.0015.0065.

[7] Josh Mills and Rafic Ajaj. "Flight Dynamics and Control Using Folding Wingtips: An Experimental Study". In: *Aerospace* 4.2 (Mar. 2017), p. 19. DOI: 10.3390/aerospace4020019. URL: https://doi.org/10.3390/aerospace4020019.

[8] Aditya A. Paranjape, Soon-Jo Chung, and Joseph Kim. "Novel Dihedral-Based Control of Flapping-Wing Aircraft With Application to Perching". In: *IEEE Transactions on*

Robotics 29.5 (Oct. 2013), pp. 1071–1084. DOI: 10.1109/tro.2013.2268947. URL: https://doi.org/10.1109/tro.2013.2268947.

[9] A. Castrichini et al. "Nonlinear Folding Wing Tips for Gust Loads Alleviation". In: *Journal of Aircraft* 53.5 (Sept. 2016), pp. 1391–1399. DOI: 10.2514/1.c033474. URL: https://doi.org/10.2514/1.c033474.

[10] Ronald C. M. Cheung et al. "Testing of a Hinged Wingtip Device for Gust Loads Alleviation". In: *Journal of Aircraft* 55.5 (Sept. 2018), pp. 2050–2067. DOI: 10.2514/1.c034811. URL: https://doi.org/10.2514/1.c034811.

[11] Joseph A. Shortal. "Effect of Tip Shape and Dihedral on Lateral-Stability Characteristics". en. In: *National Advisory Committee for Aeronautics* 588 (1937).

[12] Mohammad H Sadraey. *Aircraft Design*. en. Aerospace Series. Nashville, TN: John Wiley & Sons, Oct. 2012.

[13] Bernard Etkin and Lloy Duff Reid. *Dynamics of Flight, Stability and Control*. Third Edition. McGraw-Hill, 1996.

[14] Yufeng Chen, Kevin Ma, and Robert J. Wood. "Influence of wing morphological and inertial parameters on flapping flight performance". In: *2016 IEEE/RSJ International Conference on Intelligent Robots and Systems (IROS)*. IEEE, Oct. 2016. DOI: 10.1109/iros.2016.7759363. URL: https://doi.org/10.1109/iros.2016.7759363.

[15] SF Armanini et al. "Modelling wing wake and tail aerodynamics of a flapping-wing micro aerial vehicle". In: *International Journal of Micro Air Vehicles* 11 (Jan. 2019), p. 175682931983367. DOI: 10.1177/1756829319833674. URL: https://doi.org/10.1177/1756829319833674.

[16] Katsuhiko Ogata. *System Dynamics*. en. 4th ed. Upper Saddle River, NJ: Pearson, Aug. 2003.

[17] Mazen Farhood. *Linearization and Representation of LTI Systems*. Aug. 2019.

[18] Ir. G. J. L. Naus et al. "Gain scheduling Robust Design and Automated Tuning of Automotive Controllers". In: Oct. 2009.

[19] M Dinh and G Scorletti. "LPV system control: an overview". In: (2004).

[20] Gary J. Balas. "LINEAR, PARAMETER-VARYING CONTROL AND ITS APPLICATION TO AEROSPACE SYSTEMS". In: 2002.

[21] Federal Aviation Administration. *e-CFR 14 part 25: Airworthiness standards: Transport category airplanes*. en. Washington DC, Mar. 2022.

[22] Air Force - 11. *Department of Defense Interface Standard - Flying Qualities of Piloted Aircraft MIL-STD-1797A*. en. Aug. 2004.

[23] James L. Gresham, Benjamin M. Simmons, and Craig A. Woolsey. "Nonlinear Aerodynamic Model Identification for a Small Unmanned Aircraft from Flight Data". en. In: (2020).

[24] "XFLR5 Analysis of foils and wings operating at low Reynolds numbers". In: Oct. 2009.

[25] John D Anderson. *Fundamentals of aerodynamics*. 6th ed. Columbus, OH: McGraw-Hill Education, Mar. 2016.

[26] Ryan D. Fisher et al. "Active Control of the Dihedral Angle for a Small Fixed-Wing Unmanned Aircraft". en. In: (2018).

[27] Mark H Smith, Michael E Renzelmann, and Alan D Marx. *Folding wing-tip system*. US Patent 5,381,986. Jan. 1995.

[28] Stephen Boyd. "Stanford University: Continuous-time LQR Lecture Slides". en. In: (2009).

[29] Air Force Wright Aeronautical Labs Wright-Patterson AFB Ohio. *MIL-F-8785C, Military Specification - Flying Qualities of Piloted Airplanes*. en. Nov. 1980.

[30] Jan C. Willems. "Lyapunov Functions for Systems Described by High Order Differential Equations". en. In: *Conference of Decision and Control* (1991).

[31] Russ Tedrake. *Underactuated Robotics. Algorithms for Walking, Running, Swimming, Flying, and Manipulation*. 2022. URL: http://underactuated.mit.edu.

[32] A. Packard G. Becker. "Robust performance of linear parametrically varying systems using parametrically-dependent linear feedback". en. In: *Systems Control Letters* 23 (1994), pp. 205–215.

[33] Daniel Liberzon. *Switching in Systems and Control*. Birkhauser, Boston, 2003.

[34] Shiyun Xu et al. "On parameter-dependent Lyapunov functions for robust fault detection filter design with application in power systems". en. In: *Journal of the Franklin Institute* 349 (2012), pp. 2389–2405.

[35] Gary J. Balas. "LINEAR, PARAMETER-VARYING CONTROL AND ITS APPLICATION TO AEROSPACE SYSTEMS". en. In: *ICAS 2002 Congress* (2002).

[36] Fen Wu. "Control of linear parameter varying systems". PhD thesis. University of California, Berkeley, 1995.

[37] C.A. Desoer. "Slowly Varying Controller dx/dt=A(t)x". en. In: *IEEE Transactions on Automatic Control* 14 (1969).

[38] D. J. Leith and W. E. Leithead. "Survey of gain-scheduling analysis and design". In: *International Journal of Control* 73.11 (Jan. 2000), pp. 1001–1025. DOI: 10.1080/002071700411304. URL: https://doi.org/10.1080/002071700411304.

[39] Katsuhiko Ogata. *Modern Control Engineering*. 5th ed. Upper Saddle River, NJ: Pearson, Aug. 2009.

[40] Fredrik Bruzelius, Chalmers tekniska högskola. Institutionen för Signaler och System., and Chalmers Tekniska Högskola Sektionen elektroteknik. *Linear parameter-varying systems : an approach to gain scheduling*. Göteborg, Sweden: Dept. of Signals and Systems Chalmers University of Technology, 2004.

Appendices

Appendix A

Additional Figures

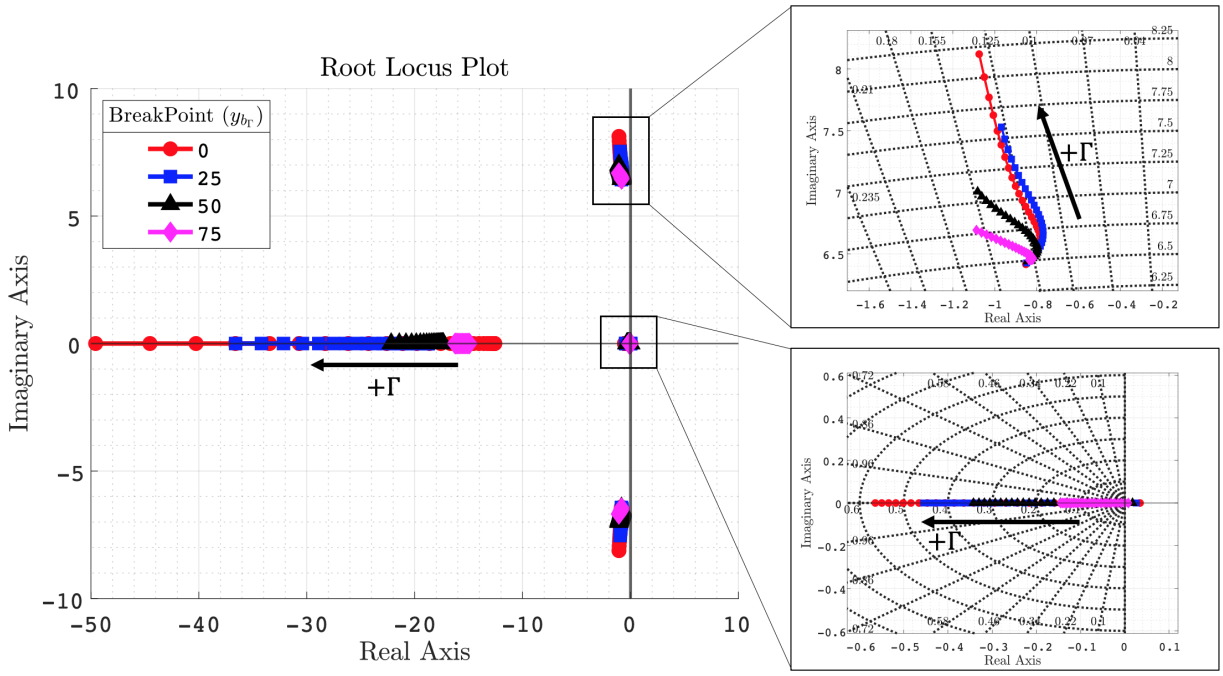

Figure A.1: Root locus for MATLAB models

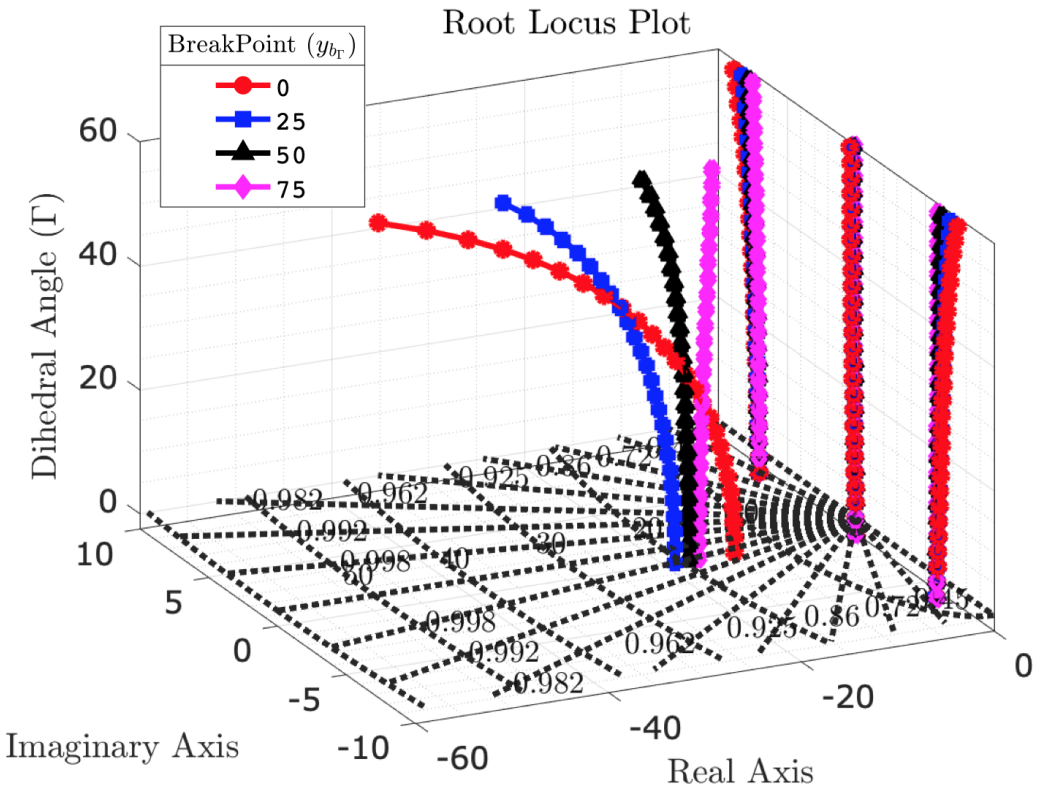

Figure A.2: 3-D root locus for MATLAB models, giving depth for Γ

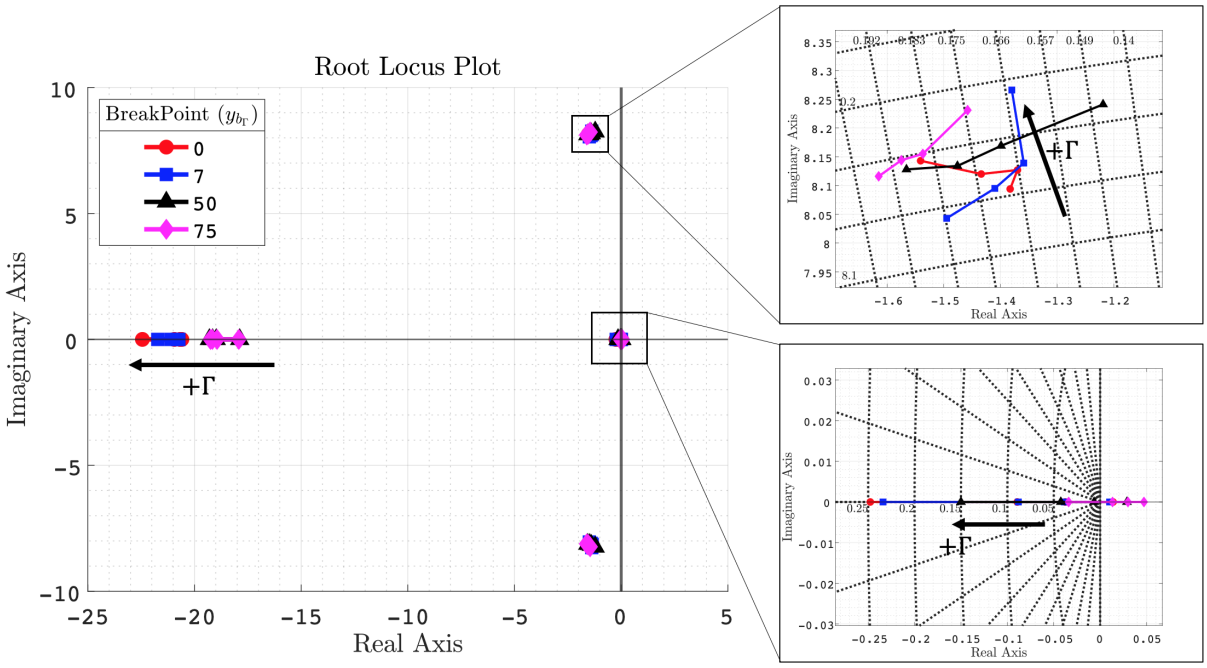

Figure A.3: Root locus for VLM models

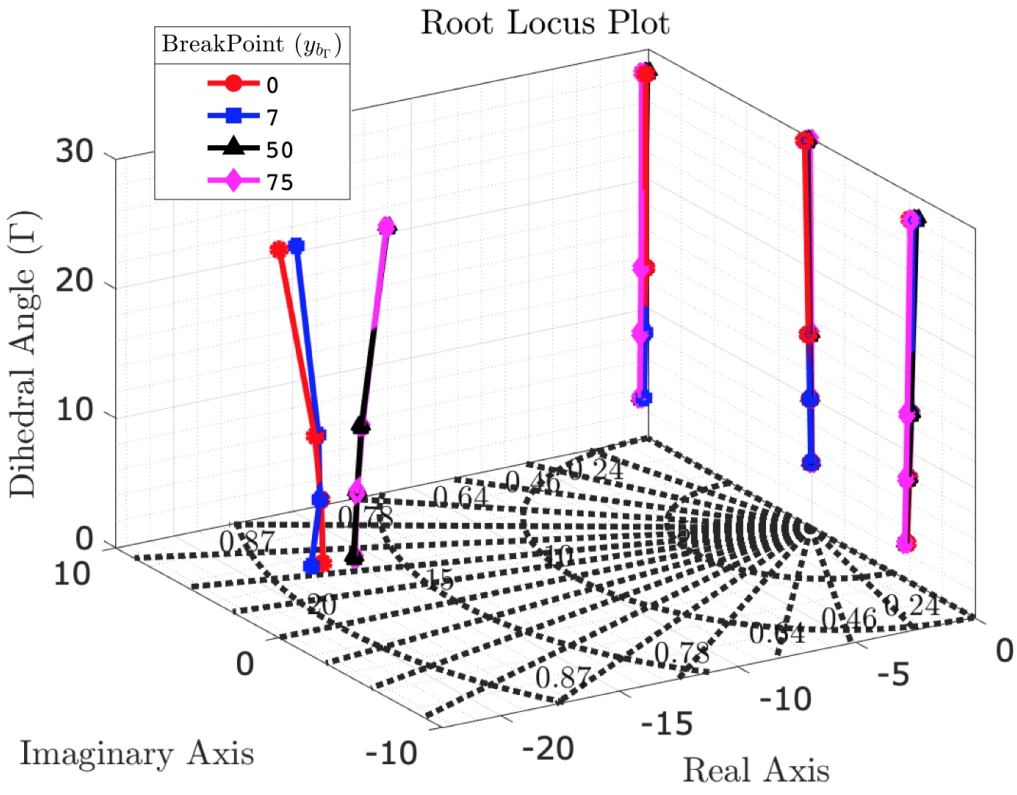

Figure A.4: 3-D root locus for VLM models, giving depth for Γ

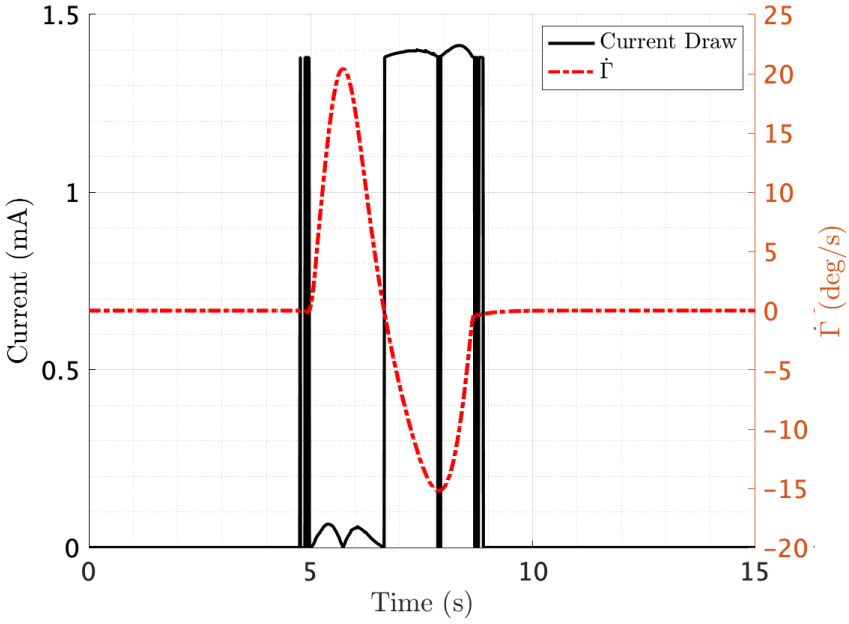

Figure A.5: Current draw required based on post-processed torque model, with $-\dot{\Gamma}$ requiring the most current to actuate against the forces generated by the wing

Appendix B

Additional Tables

MTD Aircraft Geometric Properties and Control Assumptions

Symbol	Value	Unit
ρ	0.0436	slug/ft^3
$x_{c.g.}$	0.069	ft
$y_{c.g.}$	0	ft
$z_{c.g.}$	0.083	ft
b	5.91	ft
$\bar{c}$	0.833	ft
S	4.92	ft^2
$x_{a.c.}$	0.208	ft
$y_{a.c.}$	0	ft

Table B.1: General MTD Mass Wing Parameters

Note: all positions are measured from the leading edge of the wing center aligned with the chord

Property	Symbol	Value	Unit
Aileron Start	y_1	1.478	ft
Aileron Stop	y_2	2.807	ft
Aileron Effectiveness	τ_a	0.4	-
Elevator Effectiveness	τ_e	0.4	-
Rudder Effectiveness	τ_r	0.4	-
Mean Aileron Chord	$\bar{c}_{a_{flap}}$	0.139	ft
Mean Elevator Chord	$\bar{c}_{e_{flap}}$	0.139	ft
Mean Rudder Chord	$\bar{c}_{r_{flap}}$	0.139	ft

Table B.2: MTD Control Surface Parameters

Symbol	Value	Unit
b_{ht}	1.967	ft
$\bar{c}_{ht}$	0.47	ft
e_{ht}	0.8	-
i_{ht}	-1	degree
$x_{a.c._{ht}}$	2.143	ft
$y_{a.c._{ht}}$	0.4918	ft

Table B.3: MTD Horizontal Stabilizer Parameters

Symbol	Value	Unit
b_{vt}	0.82	ft
$\bar{c}_{vt}$	0.59	ft
e_{vt}	0.8	-
$x_{a.c._{vt}}$	2.5475	ft
$x_{a.c._{vt}}$	0.205	ft

Table B.4: MTD Vertical Stabilizer Parameters

A sample set of MTD stability derivatives is provided for realization of the baseline VLM model used in analysis techniques

Property	Value
C_{x_u}	-0.0213
C_{x_a}	0.2775
C_{z_u}	-0.0002
C_{L_a}	5.09
C_{L_q}	10.672
C_{m_u}	0.0000
C_{m_a}	-2.055
C_{m_q}	-13.84
C_{Y_b}	-0.2778
C_{Y_p}	-0.0726
C_{Y_r}	0.2817
C_{l_b}	-0.0629
C_{l_p}	-0.5145
C_{l_r}	0.1406
C_{n_b}	0.0973
C_{n_p}	-0.1037
C_{n_r}	-0.1021

Table B.5: Stability Derivatives for $\Gamma = 5^\circ$ and $y_{b_\Gamma} = 0$